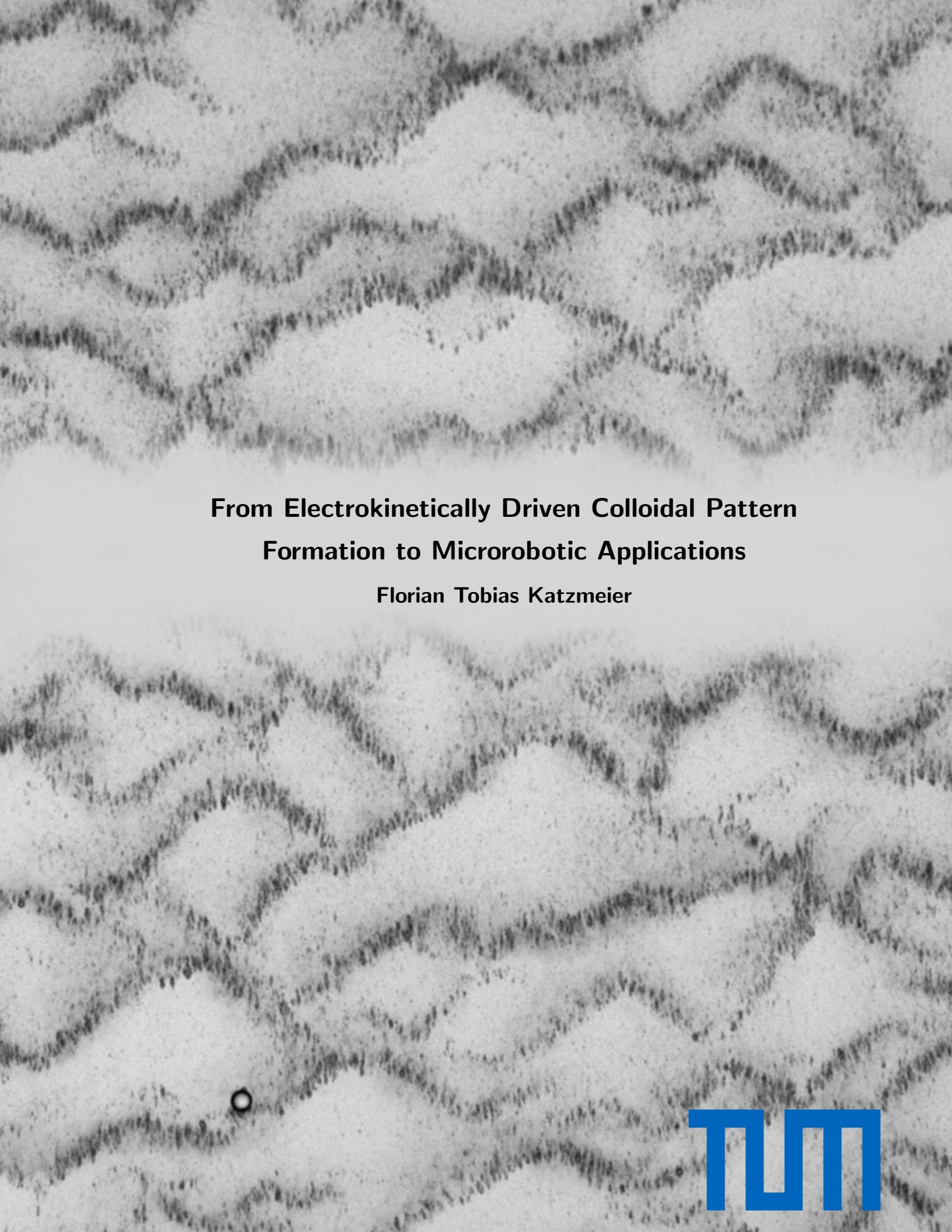

From Electrokinetically Driven Colloidal Pattern Formation to Microrobotic Applications

Florian Tobias Katzmeier

Technische Universität München
TUM School of Natural Sciences

From Electrokinetically Driven Colloidal Pattern Formation to Microrobotic Applications

Florian Tobias Katzmeier

Vollständiger Abdruck der von der TUM School of Natural Sciences der Technischen Universität München zur Erlangung des akademischen Grades eines Doktors der Naturwissenschaften (Dr. rer. nat.) genehmigten Dissertation.

Vorsitz:
Prof. Dr. Martin Zacharias

Prüfer der Dissertation:
1. Prof. Dr. Friedrich C. Simmel
2. Prof. Dr. Ulrich Gerland

Die Dissertation wurde am 18.12.2023 bei der Technischen Universität München eingereicht und durch die TUM School of Natural Sciences am 28.02.2024 angenommen.

Contents

Acknowledgements

First, I would like to express my deepest gratitude to Prof. Friedrich C. Simmel for granting me the freedom to pursue research in nonlinear electrokinetic phenomena. I am particularly grateful for the friendly research environment at his research chair. My thanks also go to my co-author Jonathan List for his initial support in implementing my experimental setup, especially for handing over his voltage amplifier. I extend special thanks to my co-author Bernhard Altaner for his assistance in literature research on electrokinetics and in interpreting experimental results.

I am grateful to all my office mates—Louis Givelet, Henning Hellmer, Anna Jäkel, Julia Müller, Thomas Frank, and Elisabeth Falgenhauer for their companionship over the years and for encouraging me to engage in social activities outside the laboratory. Special thanks to my flatmate Thomas Mayer for creating a family-like living situation. I extend my thanks to Lukas Aufinger, my former supervisor during my Master's thesis, and Aurore Dupin for their guidance in writing my first publication. I also thank Markus Eder for fruitful scientific discussions during smoking breaks. I am grateful to Lukas Oesinghaus for his rational and well-thought-out advice. Special appreciation goes to Christoph Karfuser for his inspiring out-of-the-box thinking. I extend my gratitude to Kilian Vogele, Sophie Sophie von Schönberg and Andrea Mückl for their empathy and supportive ways.

I am deeply thankful to my family: my mother Elfriede Katzmeier, my sister Anna Katzmeier, my aunt Aloisia Schäffler, and my father Christian Katzmeier, for enabling me to undertake this PhD thesis through both financial and emotional support.

Finally, I want to thank everyone with whom I interacted during my time at the Center for Nanomaterials and Nanotechnology, where I consistently had positive experiences.

Abstract

Nonlinear electrokinetic phenomena can result in a range of fascinating emergent behaviors. For instance, when aqueous suspensions of microparticles are exposed to an AC electrical field, they can organize into band patterns perpendicular to the field direction. These patterns evolve into zigzag shapes, within which particles circulate.We observed this patterning in various particles, such as silica spheres, fatty acids, oil, coacervate droplets, bacteria, and ground coffee, and determined that a second-order electrokinetic flow, specifically concentration polarization electro-osmosis (CPEO), causes this phenomenon. Brownian particle simulations, incorporating the nonlinear electroosmotic flow, accurately reproduce all observed stages of the patterning process. Furthermore, the emergence of these patterns can be quantitatively predicted by a parameter-free theory for CPEO flows. Moreover, AC electrically induced CPEO flow around asymmetric particles results in their phoretic motion, a mechanism we have termed concentration polarization electrophoresis (CPEP). To demonstrate this, we created particle dimers by connecting micron-sized silica spheres, measuring $1.0\,\mu m$ and $2.1\,\mu m$, with DNA linker molecules. These dimers can be steered in a 2D plane by controlling the AC electric field orientation using the joystick of a gamepad. Utilizing induced dipole-dipole interactions, the dimers can controllably pick up and release monomeric particles at desired positions, thereby assembling particles into groups. Systematic experiments exploring the dependence of dimer migration speed on electric field strength and frequency, as well as on buffer composition, are consistent with the theoretical framework of CPEO. Experiments with various asymmetric particles, such as fragmented ceramic, borosilicate glass, acrylic glass, agarose gel, yeast cells, and ground coffee, confirm CPEP as a general phenomenon expected for all charged dielectric particles. Turning to another electrokinetic phenomenon, specifically diffusiophoresis, we introduce our design of the diffusiophoretic trap. This trap facilitates the local upconcentration of DNA by up to a hundredfold through an electric field generated by an electrolyte gradient. Experiments with carboxylated silica particles demonstrate that the diffusiophoretic force is long-range, spanning over hundreds of micrometers. Moreover, the trap enables the localized assembly of DNA nanostars into macroscopic gels. These gels assemble in the presence of an electrolyte gradient and disassemble upon its removal, highlighting the dissipative nature of this process.

Zusammenfassung

Nichtlineare elektrokinetische Phänomene können zu einer Reihe faszinierender emergenter Verhaltensweisen führen. Beispielsweise können sich wässrige Suspensionen von Mikropartikeln, die einem Wechselstrom-Elektrofeld ausgesetzt sind, in Bandmustern senkrecht zur Feldrichtung organisieren. Diese Muster entwickeln sich zu Zickzack-Formen, innerhalb derer Partikel zirkulieren. Wir haben diese Musterbildung bei verschiedenen Partikeln beobachtet, wie zum Beispiel Silikatkugeln, Fettsäuren, Öl, Koazervat-Tropfen, Bakterien und gemahlenem Kaffee, und haben festgestellt, dass ein elektrokinetischer Fluss zweiter Ordnung, speziell die Konzentrationspolarisations-Elektroosmose (CPEO), dieses Phänomen verursacht. Brownsche Partikelsimulationen, die den nichtlinearen elektroosmotischen Fluss einbeziehen, reproduzieren genau alle beobachteten Stadien des Musterbildungsprozesses. Darüber hinaus kann das Auftreten dieser Muster quantitativ durch eine parameterfreie Theorie für CPEO-Ströme vorhergesagt werden. Weiterhin führt der durch Wechselstrom induzierter CPEO-Fluss um asymmetrische Partikel zu deren phoretischen Bewegung, ein Mechanismus, den wir als Konzentrations-polarisations-Elektrophorese (CPEP) bezeichnet haben. Um dies zu demonstrieren, haben wir Partikeldimere erstellt, indem wir mikrometergroße Silikakugeln mit Durchmessern von $1.0\,\mu m$ und $2.1\,\mu m$ mittels DNA verbunden haben. Diese Dimere können in der 2D-Ebene durch die Kontrolle der Ausrichtung des Wechselstromfeldes mit dem Joystick eines Gamepads gesteuert werden. Durch Ausnutzung induzierter Dipol-Dipol-Interaktionen können die Dimere Monomere kontrolliert aufnehmen und an gewünschten Positionen ablegen, wodurch die Monomere in Gruppen angeordnet werden können. Systematische Experimente, die die Abhängigkeit der Migrationsgeschwindigkeit der Dimere von der Stärke und Frequenz des elektrischen Feldes sowie von der Pufferzusammensetzung untersuchen, stehen im Einklang mit den theoretischen Vorhersagen der CPEO. Experimente mit verschiedenen asymmetrischen Partikeln, wie fragmentierter Keramik, Borosilikatglas, Acrylglas, Agarosegel, Hefezellen und gemahlenem Kaffee, bestätigen CPEP als generisches Phänomen, das für alle geladenen dielektrischen Partikel zu erwarten ist. Im Hinblick auf ein weiteres elektrokinetisches Phänomen, speziell die Diffusiophorese, stellen wir unser Design einer diffusiophoretischen Falle vor. Diese Falle ermöglicht die lokale Aufkonzentration von DNA auf bis zu das Hundertfache durch ein elektrisches Feld, das durch einen Elektrolytgra-

dienten erzeugt wird. Experimente mit karboxylierten Silikapartikeln zeigen, dass diese diffusiophoretische Kraft langreichweitig ist und sich über Hunderte von Mikrometern erstreckt. Außerdem ermöglicht die Falle die lokale Assemblierung von DNA-Nanosternen zu makroskopischen Gelen. Diese Gele bilden sich in Anwesenheit des Elektrolytgradienten und zerfallen wieder bei dessen Abwesenheit, was den dissipativen Charakter dieses Prozesses unterstreicht.

List of Publications

- **F. Katzmeier** and F.C. Simmel. "Microrobots powered by concentration polarization electrophoresis (CPEP)." *Nature Communications*, vol. 14, Article 6247, 2023.
- **F. Katzmeier**, B. Altaner, J. List, U. Gerland, and F.C. Simmel. "Emergence of colloidal patterns in ac electric fields." *Physical Review Letters*, vol. 128, no. 5, 058002, 2022.
- **F. Katzmeier**, L. Aufinger, A. Dupin, J. Quintero, M. Lenz, L. Bauer, S. Klumpe, D. Sherpa, B. Dürr, M. Honemann, I. Styazhkin, F.C. Simmel, M. Heymann. "A low-cost fluorescence reader for in vitro transcription and nucleic acid detection with Cas13a." *PLoS One*, vol. 14, no. 12, e0220091, 2019.
- **F. Katzmeier** and F.C. Simmel. "Non-Equilibrium Assembly of Nucleic Acids in a Diffusiophoretic Trap." Currently under review.

1. Introduction

Historically, the first comprehensive theoretical treatment of an electrokinetic phenomenon was presented by Helmholtz in 1876 [1]. In his work, he discusses the flow induced by an electric field in a charged tube filled with an electrolyte, a phenomenon now referred to as electroosmosis. Helmholtz postulated, based on the experimental work of Quincke [2], the existence of an electric double layer on the surface of a charged substance, which arises from counterions being attracted to the charged surfaces. He proposed that when an electric field is applied along the tube, electric forces act on the counterion layer along the wall, consequently dragging the liquid with them.

Later, in 1903, Smoluchowski derived an equation for the migration velocity of charged spheres immersed in an electrolyte under the influence of an electric field [3]. This phenomenon, initially known as cataphoresis, is now referred to as electrophoresis. According to Smoluchowski, the migration velocity v of a particle due to the applied electric field strength E is expressed as:

$$v = \frac{\epsilon\zeta}{\eta}E \tag{1.1}$$

Notably, the electroosmotic flow velocity in a pipe, as derived by Helmholtz, assumes the same form. Consequently, the equation is now known as the Helmholtz-Smoluchowski equation [3]. The prefactor in this equation is commonly referred to as electrophoretic mobility and is a function of the dielectric constant ϵ and the viscosity η of the fluid. The parameter ζ, known as the zeta potential, represents the potential difference between the charged surface and the electrolyte. The zeta potential serves as a lumped parameter in the above equation and depends on the structure of the electric double layer. Interestingly, the derivations by Helmholtz and Smoluchowski only required the double layer to be thin compared to the size of the tube or particle, but did not require an explicit expression for the charge distribution within it. The flow fields computed by Helmholtz and Smoluchowski are illustrated in Figure 1.1. The structure of the electric double layer was later analyzed independently by Gouy in 1910 [4] and Chapman in 1913 [5]. Their analysis allowed the calculation of the zeta potential ζ from the surface charge and the electrolyte concentration. The Gouy–Chapman model led to an expression for the characteristic size

λ_D of the electric double layer:

$$\lambda_D = \sqrt{\frac{\epsilon k_B T}{2e^2 c}} \tag{1.2}$$

In this equation, k_B represents the Boltzmann constant, T is the temperature, e denotes the elementary charge, and c is the concentration of monovalent ions. The length λ_D is below $10\,\text{nm}$ for ion concentrations exceeding $1\,\text{mM}$. This finding can be viewed as a later validation of Helmholtz's and Smoluchowski's assumption of a comparably thin double layer. The characteristic size λ_D, referred to as the Debye length, was named after Peter Debye, who calculated the electrophoretic migration velocity in 1923 for the opposite limit to that assumed by Smoluchowski, where the size of the double layer is much larger than the particle [6].

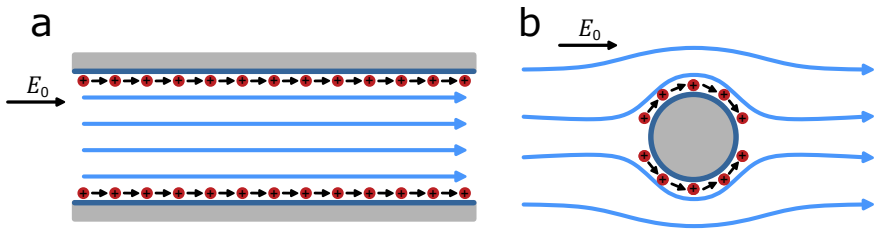

Figure 1.1. Flow fields computed by Helmholtz and Smoluchowski. (a) Electroosmotic flow in a negatively charged tube, where an electric field E_0 drives the positive counter ions in the double layer along the tube, inducing flow throughout the tube. (b) Electroosmotic flow around a negatively charged spherical particle, with the electrophoretic migration velocity of the particle directed to the left.

Another interesting aspect of the Helmholtz-Smoluchowski equation is its lack of a size parameter for the tube or particle. This implies, as Smoluchowski himself pointed out, that equation 1.1 is applicable to particles of any shape and size. This topic was further explored by Henry in 1931, who sought to establish a connection between the limiting cases discussed by Smoluchowski and Debye. He concluded that equation 1.1 indeed applies to particles of any shape when the zeta potential ζ is approximately independent of the particle size [7]. This is precisely the case in the limit of comparably thin electric double layers, as assumed by Helmholtz and Smoluchowski. A rigorous proof of the shape independence of the Helmholtz-Smoluchowski equation can be found in reference [8].

Further refinements to the theory of Smoluchowski were made by Bikerman in the 1930s, who realized that the double layer could accumulate a considerable amount of counter ions in cases of large zeta potentials [9, 10]. This accumulation leads to ion-selective surface conduction. Under the influence of an external electric field, the counter ion species is

selectively transported along the surface of the particle, resulting in charge separation. This separation, in turn, generates an electric field that opposes the external electric field. The opposing electric field reduces the electrophoretic migration velocity and introduces shape and size dependence into the equation.
In the 1960s, Soviet scientist Stanislav Dukhin offered a more comprehensive treatment of ion-selective surface conduction in the thin double layer limit, specifically accounting for the transport equations of each ion species [11]. His analysis revealed that ion flux balance on the particle surface leads to a distortion of the bulk salt concentration near the particle. Such distortions of the bulk salt concentration duo to local ion selective conduction is now known as concentration polarization. A dimensionless quantity characterizing the contribution of surface conductivity, known as the Dukhin number Du, was named after him. Further enhancements to the equation for the electrophoretic migration velocity, which have gained more recognition in the Western world, were later developed by O'Brien and White [12–14]. Notably, O'Brien and White where apparently unaware of Dukhins work in their initial analysis [12]. Other contributions to the theory of electrophoresis, leading up to the work of O'Brien and White, were made by Overbeek [15] and Wiersema [16], who built upon the work of Henry.

Dukhin also made a significant contribution in explaining a related phenomenon, namely Diffusiophoresis. Diffusiophoresis refers to the directed migration of colloidal particles in a concentration gradient, driven by double layer forces. Following its initial discovery by Derjaguin and coworkers [17], Dukhin and Derjaguin provided a satisfactory theoretical explanation for this phenomenon. Analogous to the Helmholtz-Smoluchowski equation for electrically induced flow velocity, the concentration gradient-induced flow velocity is now known as the Dukhin-Derjaguin slip boundary condition. More recent theoretical advancements in describing diffusiophoresis were subsequently made by Prieve [18, 19].

Another significant contribution of Dukhin in colaboration with Shilov was the extension of his theory of ion-selective surface conduction to particles subjected to AC electric fields [20, 21]. He discovered that concentration polarization provides a satisfactory explanation for a phenomenon known as low-frequency dielectric dispersion. In suspensions of colloidal particles within aqueous electrolyte solutions, unusually high dielectric constants are typically observed at low electric field frequencies [22, 23]. Dukhin determined that the double layer around colloidal particles becomes polarized at frequencies corresponding to the relaxation time of the concentration polarization mechanism. This mechanism is predominantly governed by ion diffusion around particles, which suggests a characteristic

frequency given by

$$f_{\mathsf{cr}} = \frac{1}{2\pi}\frac{2D}{R^2} \tag{1.3}$$

where D is the ion diffusion constant and R is the particle radius [24]. This frequency assumes a value around $1\,\mathrm{kHz}$ for micrometer-sized particles, which precisely matches the range where the unusually high dielectric constants were measured. Notably, a competing theory in Western literature was proposed by Schwarz, also involving surface conduction [22]. In 1983, Lyklema reviewed both explanations and concluded that the phenomenon of low-frequency dielectric dispersion is best explained by Dukhin's approach [24].

Over a century after Helmholtz presented his linear theory on electroosmosis, first investigations into nonlinear electrokinetic phenomena were conducted by Gamayunov, Murtsovkin, and Andrei Dukhin, son of Stanislav Dukhin, in the 1980s. They studied the flow field generated by a DC electric field around polarizable particles, such as metal particles, and the consequent interactions between particle pairs [25–27]. Ramos et al. rediscovered similar flows in 1998 [28] around microelectrodes in a microfluidic system and provided a theoretical analysis in 1999 [29]. Squires and Bazant conducted a comprehensive theoretical analysis of this electroosmotic flow and coined the term 'Induced Charge Electroosmosis' (ICEO) [30]. They also highlighted the previously unrecognized work of Gamayunov, Murtsovkin, and Andrei Dukhin. In the context of induced charge electroosmosis, the electrically induced fluid flow significantly differs around strongly polarizable particles compared to the classical electroosmotic flow around weakly polarizable particles. For strongly polarizable particles, the surface charge is induced by the applied electric field, unlike the fixed surface charge in classical electrophoresis. Consequently, an induced electric double layer is formed, to which the external field couples. This coupling gives rise to a quadratic dependence of the induced hydrodynamic flow on the electric field:

$$v \propto \frac{\epsilon R}{\eta} E^2 \tag{1.4}$$

Contrary to classical electrophoresis, this flow does not induce motion in spherical particles, as it is symmetric about the particle equator. The flow field is illustrated in Figure 1.2. However, due to the symmetry, steady streaming is expected in an AC-electric field. ICEO also exhibits a characteristic frequency below which the flow magnitude is anticipated to be strongest. This frequency is determined by the time needed to charge the double-layer through the bulk resistance and is given by

$$f_c = \frac{1}{2\pi}\frac{D}{\lambda_D R}. \tag{1.5}$$

This frequency assumes values of around $20\,\mathrm{kHz}$ for micrometer-sized particles in ion concentrations of approximately $1\,\mathrm{mM}$. While the flow is symmetric for spheres and does not induce propulsion, asymmetric particles can generate asymmetric flows, which leads to their propulsion even in AC electric fields. Bazant and Squires named this mechanism 'Induced Charge Electrophoresis' (ICEP) [31].

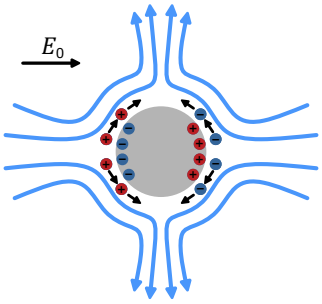

Figure 1.2. Induced Charge Electroosmotic flow around a spherical metal particle. The external electric field E_0 induces surface charges, which attract counterions, forming an induced electric double layer. The external field exerts a force on these counterions, resulting in an induced electroosmotic flow.

Recently, Schnitzer and Yariv developed a systematic approach for calculating nonlinear contributions to the electrophoretic migration velocity of dielectric, charged spherical particles, accounting for ion-selective surface conduction [32, 33]. Their calculations included a second-order contribution to the flow field, similar in form to ICEO flows. However, this contribution did not affect the migration velocity due to its symmetry.

In the past few years, steady streaming driven by AC electric fields has also been observed around nonconducting surfaces. This phenomenon was independently discovered in microfluidic channels by the research group of Ramos [34] and around micrometer-sized particles in my own work [35]. It was found that the steady streaming is most pronounced at electric field frequencies corresponding to those where the low-frequency dielectric dispersion was measured. Consequently, we independently concluded that concentration polarization is responsible for the induced fluid flow. Since Schnitzer and Yariv's approach already accounted for concentration polarization in the DC case, it was logical to extend their methodology to AC-electric fields [35, 36]. Utilizing Schnitzer and Yariv's framework, Fernandez-Mateo computed the flow field around a dielectric charged sphere in an AC-electric field and introduced the term 'Concentration Polarization Electroosmosis' (CPEO) [36]. Notably, Gamayunov, Murtsovkin, and Andrei Dukhin also predicted this hydrodynamic effect around charged dielectric particles in the earlier mentioned work on interacting particle pairs in DC-electric fields.

With this thesis, I join the group of scientists who have rediscovered electrokinetic phenomena already discussed in Soviet literature. I explore two electrokinetic phenomena caused by Concentration Polarization Electroosmosis (CPEO). In Chapter 2, I introduce the classical theory of electrophoresis and diffusiophoresis, establishing the terminology and concepts used in subsequent chapters. In Chapter 3, I present the collaborative work conducted by my co-authors and myself on a colloidal patterning phenomenon in an AC electric field, which we explain through AC electric field-induced CPEO flows resulting in hydrodynamic interactions between particles. Subsequently, in Chapter 4, I present the work conducted by Friedrich Simmel and myself on CPEO flow-induced propulsion of asymmetric particles in AC electric fields, a phenomenon we refer to as Concentration Polarization Electrophoresis (CPEP). Specifically, we experimentally demonstrate the breakdown of shape independence under experimental conditions where CPEO flows are expected. Finally, in Chapter 5, I present the work conducted by Friedrich Simmel and myself on another electrokinetic phenomenon, specifically diffusiophoresis. We introduce our design of the diffusiophoretic trap, which facilitates the local concentration of DNA and enables hybridization reactions, as well as the localized assembly of DNA nanostars into macroscopic gels.

2. Fundamentals

In this chapter, I provide a mathematical introduction to the theory of electrophoresis of colloidal particles.

In Section 2.1, we[1] will begin by outlining the governing equations commonly used to characterize electrokinetic phenomena [12–14, 16, 32, 33, 36–40]. Next, in Section 2.2, we will examine an equilibrium solution of the governing equations to introduce the concept of charge screening and electric double layers in electrolyte solutions [41, 42]. In Section 2.3, we will discuss electroosmosis, which refers to the liquid motion induced by an electric field above a charged plane [42, 43]. Subsequently, in Section 2.4, we will investigate the flow field around micrometer-sized charged particles enveloped by a comparatively thin electric double layer due to an externally applied electric field [12–14, 32, 37, 44]. From this flow profile, we will derive the migration velocity, namely the Smoluchowski equation, and subsequently prove its shape independence [8]. Next, in Section 2.5, we will explore diffusioosmosis in electrolytes, which refers to the liquid motion above a plane induced by a concentration gradient along it. Lastly, in Section 2.6, we will discuss diffusiophoresis in electrolytes, the directed migration of particles in a concentration gradient [18, 19, 40, 43].

[1] With "we" I refer to the reader and myself, as is common practice in many textbooks.

2.1 Governing Equations

The equations presented in this section are generally implicitly assumed in most treatments of electrokinetic phenomena. Explicit formulations of these equations can be found in [37, 38], and their dimensionless versions are available in [32, 33].

An electrolyte consisting of monovalent salts, such as NaCl, subjected to an electric field can be described by the Nernst-Planck equations. The fluxes $\boldsymbol{j}^+$ and $\boldsymbol{j}^-$ of positive and negative ions with concentrations c^+ and c^- are given by

$$\boldsymbol{j}^+ = -D^+ \boldsymbol{\nabla} c^+ - D^+ \frac{e}{k_B T} c^+ \boldsymbol{\nabla} \Phi + c^+ \boldsymbol{v} \tag{2.1}$$

and

$$\boldsymbol{j}^- = -D^- \boldsymbol{\nabla} c^- + D^- \frac{e}{k_B T} c^- \boldsymbol{\nabla} \Phi + c^- \boldsymbol{v}. \tag{2.2}$$

The first term describes ion diffusion according to Fick's law, where D^+ and D^- are the diffusion constants. The second term describes the migration of ions with charges $+e$ and $-e$ due to the electric field $\boldsymbol{E} = -\boldsymbol{\nabla}\Phi$, associated with the potential Φ. Note that we used the Einstein relation to express the electrical ion mobilities as $\frac{\pm e D^\pm}{k_B T}$. Here, k_B is the Boltzmann constant and T is the temperature in K. The last term describes possible additional drift due to a fluid flow with velocity $\boldsymbol{v}$. Each ion species has an associated conservation law given by

$$\frac{\partial c^+}{\partial t} + \boldsymbol{\nabla} \cdot \boldsymbol{j}^+ = 0 \tag{2.3}$$

and

$$\frac{\partial c^-}{\partial t} + \boldsymbol{\nabla} \cdot \boldsymbol{j}^- = 0. \tag{2.4}$$

The electric potential, Φ, is related to the density of free charges, ρ_e, through the Poisson equation. The charge density, in turn, is related to the ion concentrations via $\rho_e = e(c^+ - c^-)$. The electric potential is therefore described by

$$-\epsilon \Delta \Phi = \rho_e = e(c^+ - c^-) \tag{2.5}$$

where ϵ is the dielectric constant of water. Lastly, we need an evolution equation for the fluid velocity $\boldsymbol{v}$. For micron-sized particles, we can use the creeping flow approximation such that the fluid velocity, $\boldsymbol{v}$, and the pressure, P, are described by Stokes flow:

$$0 = \eta \Delta \boldsymbol{v} - \boldsymbol{\nabla} P + \rho_e \boldsymbol{E} \tag{2.6}$$

$\rho_e \boldsymbol{E}$ is the Coulomb force density or electric body force, which can also be expressed as $-e(c^+ - c^-)\boldsymbol{\nabla}\Phi$ or $\epsilon\Delta\Phi\boldsymbol{\nabla}\Phi$ according to the above definitions. The creeping flow equation must be complemented by the conservation law $\boldsymbol{\nabla} \cdot \mathbf{v} = 0$ for incompressible fluids.

2.2 Electric Double Layer as Equilibrium Solution

First, we discuss an equilibrium solution of the system of partial differential equations introduced in the previous section. We consider the scenario depicted in Figure 2.1a, where a charged plane is submerged in an electrolyte. Counter ions are attracted and accumulate near the surface, while co-ions are repelled and depleted near the surface. The resulting charge distribution is sketched in Figure 2.1. The counter ions screen the surface charge, making the plane appear electrically neutral at distances far from the surface. The emerging charge distribution is commonly referred to as electric double layer, Debye layer, or diffuse layer. This structure has a characteristic size known as the Debye length, denoted by λ_D on the x-axis.

The following discussion primarily draws from [42] and [41] and describes the the Gouy-Chapman model of electric double layers. However, we begin by deriving the Poisson-Boltzmann equation rather than assuming it, to introduce slightly modified equations as in [32]. Additionally, in subsection 2.2.4, we derive the hydrostatic pressure in the Debye layer following the approach in [40]. This will be relevant when we later discuss diffusiophoresis and diffusioosmosis in section 2.5 and section 2.6.2.

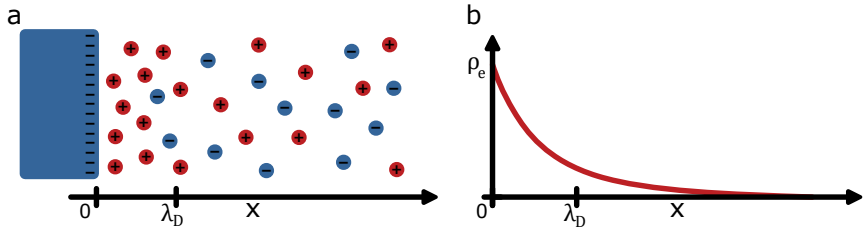

Figure 2.1. Schematic representation of a charged surface in contact with an electrolyte. **a** Positive ions accumulate near the charged surface, while negative ions are repelled. **b** Corresponding charge density distribution ρ_e as a function of distance from the charged surface. The Debye length λ_D is marked on the x-axis.

2.2.1 Poisson Boltzmann Equation

In equilibrium, the net ion fluxes $\boldsymbol{j}^+$ and $\boldsymbol{j}^-$, as well as the fluid flow $\boldsymbol{v}$, vanish everywhere. In a one-dimensional scenario, as illustrated in Figure 2.1, the ion flux equations simplify

to

$$0 = -\frac{\partial c^+}{\partial x} + \frac{e}{k_B T} c^+ \frac{\partial \Phi}{\partial x} \tag{2.7}$$

and

$$0 = -\frac{\partial c^-}{\partial x} - \frac{e}{k_B T} c^- \frac{\partial \Phi}{\partial x}. \tag{2.8}$$

By dividing each of these equations by their respective concentrations, c^+ and c^-, and making use of the identity $\frac{\partial c^\pm}{\partial x}/c^\pm = \frac{\partial \ln\left(c^\pm\right)}{\partial x}$, we can integrate both equations. This process yields a Boltzmann distribution for the ion species:

$$c^+ = A^+ e^{\frac{-e(\Phi + B^+)}{k_B T}} \tag{2.9}$$

and

$$c^- = A^- e^{\frac{+e(\Phi + B^-)}{k_B T}} \tag{2.10}$$

Here, A^+, A^-, B^+, and B^- are integration constants which need to be determined by boundary conditions. Physically, we expect that far from the charged plane, the potential approaches a constant value, φ. Additionally, ion concentrations should stabilize to a bulk ion concentration, c. Mathematically, this translates to the conditions $c^+(\infty) = c^-(\infty) = c$ and $\Phi(\infty) = \varphi$. Using these boundary conditions, we deduce expressions for the ion concentrations:

$$c^+ = c e^{\frac{-e(\Phi - \varphi)}{k_B T}} \tag{2.11}$$

$$c^- = c e^{\frac{+e(\Phi - \varphi)}{k_B T}} \tag{2.12}$$

Note that most other treatments set the potential φ far from the charged plane to zero [42]. Inserting the expressions for the ion concentrations into the Poisson equation 2.5 yields

$$-\epsilon \frac{\partial^2 \Phi}{\partial x^2} = \rho_e = ec \left(e^{\frac{-e(\Phi - \varphi)}{k_B T}} - c e^{\frac{+e(\Phi - \varphi)}{k_B T}} \right). \tag{2.13}$$

This equation is commonly referred to as the one dimensional Poisson-Boltzmann equation. We can introduce the potential difference $\Psi = \Phi - \varphi$ to reach a more recognizable form. Note that subtracting the constant φ from Φ does not alter the left side of the equation. By introducing the hyperbolic sine function, we obtain

$$\frac{\partial^2 \Psi}{\partial x^2} = 2 \frac{ec}{\epsilon} \sinh\left(\frac{e\Psi}{k_B T} \right). \tag{2.14}$$

2.2.2 Linearized Poisson Boltzmann Equation

It is instructive to consider a linearization of the Poisson Boltzmann equation. We can linearize this differential equation by assuming that the electric potentials are much smaller than the thermal voltage $\frac{k_B T}{e}$. Specifically, assuming $\frac{e\Psi}{k_B T} \ll 1$ yields

$$\frac{\partial^2 \Psi}{\partial x^2} \approx 2\frac{e^2 c}{\epsilon k_B T}\Psi. \tag{2.15}$$

Using the boundary condition $\Psi(\infty) = \varphi(\infty) - \varphi = 0$, the solution is

$$\Psi = \zeta e^{\frac{-x}{\lambda_D}}, \tag{2.16}$$

where we define the Debye length as $\lambda_D = \sqrt{\frac{\epsilon k_B T}{2e^2 c}}$. ζ is the zeta potential and typically represents the potential value directly at the charged surface, which is at $x = 0$. Using our definition, the zeta potential, $\zeta = \Psi(0) = \Phi(0) - \varphi$, represents the potential difference between the charged surface and the bulk. The potential distribution is shown in Figure 2.2. ζ can be determined by the boundary condition on the charged surface. According to Gauss's law the surface charge σ is related to the electric field at the surface via $\sigma = \epsilon E(0) = -\epsilon \frac{\partial \Psi}{\partial x}(0)$. We find $\zeta = \frac{\lambda \sigma}{\epsilon}$. We will discuss a general expression for ζ later, using the exact Poisson-Boltzmann equation.

The Debye length λ_D represents the characteristic length scale of the Debye layer. In the

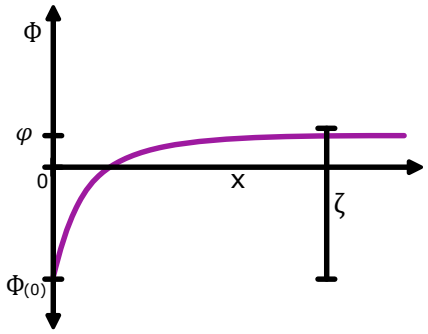

Figure 2.2. Potential distribution near a negatively charged plane. The surface potential $\Phi(0)$ exhibits a negative drop, ζ, relative to the bulk potential, φ. Here, ζ represents the zeta potential.

linearized scenario described here, it's the length where the surface potential decreases to $\frac{1}{e}$ of its surface value. Additionally, we can compute the charge distribution ρ_e using the Poisson equation as $\rho_e = -\epsilon \frac{\partial^2 \Psi}{\partial x^2}$. This results in $\rho_e = \frac{-\epsilon \zeta}{\lambda_D^2} e^{\frac{-x}{\lambda_D}}$, which has the same distance dependence. We can interpret λ_D as the characteristic length scale of the extension of the counterion cloud shown in Figure 2.1. The Debye length explicitly depends on

the bulk ion concentration c as $\lambda_D \propto \frac{1}{\sqrt{c}}$. In a solution with typical ion concentrations of $1\,\text{mM}$, $10\,\text{mM}$, and $100\,\text{mM}$ of monovalent salts, the corresponding Debye lengths at $20°\text{C}$ are $\lambda_D = 9.6\,\text{nm}$, $\lambda_D = 3.1\,\text{nm}$, and $\lambda_D = 0.96\,\text{nm}$, respectively. It is important to note that the ion concentration c in our definition of λ_D is in molecules per m^3. The computed values imply that the counterion cloud has a typical size on the order of several nm, making it comparably small in most experimental setups and even for µm-sized particles.

2.2.3 Zeta Potential and Grahame Equation

We now return to the exact Poisson Boltzmann equation 2.14 to derive an exact expression for the zeta potential ζ. Multiplying the Poisson Boltzmann equation with $\frac{\partial \Psi}{\partial x}$ and using the chain rule yields

$$\frac{1}{2}\frac{\partial}{\partial x}\left(\frac{\partial \Psi}{\partial x}\right)^2 = 2\frac{ec}{\epsilon}\frac{\partial}{\partial x}\sinh\left(\frac{e\Psi}{k_B T}\right). \tag{2.17}$$

which can be integrated to

$$\frac{1}{2}\left(\frac{\partial \Psi}{\partial x}\right)^2 = A + 2\frac{k_B T c}{\epsilon}\cosh\left(\frac{e\Psi}{k_B T}\right). \tag{2.18}$$

A is an integration constant and can again be determined by the boundary condition $\Psi(\infty) = 0$ and also $\frac{\partial \Psi}{\partial x}(\infty) = 0$. We find $A = -2\frac{k_B T c}{\epsilon}$ which gives

$$\left(\frac{\partial \Psi}{\partial x}\right)^2 = 4\frac{k_B T c}{\epsilon}\left(\cosh\left(\frac{e\Psi}{k_B T}\right) - 1\right) = 8\frac{k_B T c}{\epsilon}\sinh^2\left(\frac{e\Psi}{2k_B T}\right). \tag{2.19}$$

This equation can in principle be solved exactly by separation of variables. We are however only interested in the value of Ψ at the surface namely the zeta potential $\Psi(0) = \zeta$. We can use the above equation directly and use again the Gauss type boundary condition of the electric field $-\epsilon\frac{\partial \Psi}{\partial x}(0) = \sigma$ at the surface to relate the surface charge to the zeta potential:

$$\sigma = \sqrt{8\epsilon k_B T c}\sinh\left(\frac{e\zeta}{2k_B T}\right) \tag{2.20}$$

It is important to highlight that we took the square root of equation 2.19 before applying the boundary condition, selecting the sign of the square root to match negative surface charges with negative surface potentials. The equation presented above is commonly known as the Grahame equation and allows us to compute the zeta potential ζ directly from the surface charge, or vice versa. It is important to note that ζ explicitly depends on

the bulk ion concentration c. Furthermore, according to our definitions, the zeta potential should be interpreted as the potential difference between the surface potential $\Phi(0)$ and the bulk potential φ, given by $\zeta = \Psi(0) = \Phi(0) - \varphi$ as indicated in Figure 2.2.

2.2.4 Equilibrium Pressure

We derive the hydrostatic pressure P in the Debye layer, following the approach in [40]. The hydrostatic pressure can be computed using the one-dimensional creeping flow equation 2.6 with $\boldsymbol{v} = 0$:

$$\frac{\partial P}{\partial x} = \rho_e E = -e(c^+ - c^-)\frac{\partial \Psi}{\partial x} \tag{2.21}$$

Note that the electric field E should be computed from the complete potential $\Phi(x)$ using $E = -\frac{\partial \Phi}{\partial x}$. This is however equivalent to $E = -\frac{\partial \Psi}{\partial x}$ since $\Psi(x) = \Phi(x) - \varphi$.
This can be further simplified using the expressions for c^+ and c^-, and by once again employing the hyperbolic sine function:

$$\frac{\partial P}{\partial x} = 2ec \sinh\left(\frac{e\Psi}{k_B T}\right)\frac{\partial \Psi}{\partial x} = 2k_B T c \frac{\partial}{\partial x}\cosh\left(\frac{e\Psi}{k_B T}\right) \tag{2.22}$$

After integration and applying the boundary condition $\Psi(\infty) = 0$, we obtain an expression for the hydrostatic pressure:

$$P = P_0 + 2k_B T c\left(\cosh\left(\frac{e\Psi}{k_B T}\right) - 1\right) = P_0 + 4k_B T c \sinh^2\left(\frac{e\Psi}{2k_B T}\right) \tag{2.23}$$

P_0 represents the hydrostatic pressure in the bulk, that is, far away from the charged surface, where we require $P(\infty) = P_0$.

2.3 Electroosmosis

We present a non-equilibrium solution to the system of equations outlined in Section 2.1. We will discuss electroosmosis, which refers to the motion of liquid in a charged channel filled with an electrolyte due to an applied electric field. We start with a conceptual explanation of electroosmosis and subsequently transitions to its mathematical derivation where we mainly follow [43] and [42]. We will derive the flow profile depicted in Figure 2.3d, resulting from the application of an electric field E_0 parallel to the charged surface shown in Figure 2.3a.

2.3.1 Conceptual Discussion

Consider the setup illustrated in Figure 2.3a, where an electric field is applied parallel to a charged plane. Near the plane, counterions accumulate and coions are expelled, forming an electric double layer as in the equilibrium case. The electric potential $\Phi(\infty, y)$ far from the plane varies with the y-coordinate parallel to the plane due to the external electric field. The horizontal electric field E_0 acts on the ions, resulting in horizontal ion currents j_y^+ and j_y^-. The charge distribution is depicted in Figure 2.3b. Within the electric double layer, where a net charge density is present, a net force density acts on the liquid. The resulting Coulomb force density $F_c = \rho_e E_0$ is illustrated in Figure 2.3c. At an atomistic level, the net force density can be explained by the differential drag exerted by the ions on the liquid: Far from the surface, equal amounts of positive and negative ions are dragged through the liquid in opposite directions, resulting in no net force on the fluid. Closer to the surface, the number of counterions being dragged through the liquid exceeds that of coions moving in the opposite direction, which leads to a net force exerted on the fluid in this region.

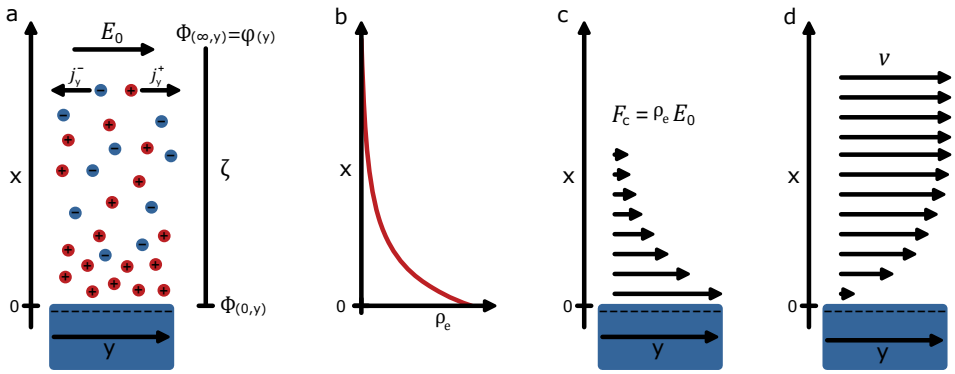

Figure 2.3. Schematic representation of an electric double layer subjected to a tangential electric field, inducing electroosmosis. (a) Positive ions accumulate near the charged surface, whereas negative ions are repelled. A tangential electric field E_0 moves the ion species in opposite directions. The electric potential Φ is indicated on the right. The potential difference ζ, between the surface $\Phi(0, y)$ and positions far away $\Phi(\infty, y)$ from the surface, is independent of y. (b) Corresponding charge density distribution ρ_e as a function of distance from the charged surface. (c) Coulomb force density resulting from the tangential electric field acting on the charge density distribution. (d) Flow profile resulting from the stress balance between Coulomb and viscous forces.

The net force density leads to liquid motion within the electric double layer. The resulting flow field is depicted in Figure 2.3d. The fluid velocity v at the surface is zero, as the liquid is in contact with the stationary surface. Within the double layer, the Coulomb force

density drags the liquid. The liquid motion is opposed by viscous stress, arising from the fluid velocity gradient $\frac{\partial v}{\partial x}$. Thus, within the double layer, the Coulomb force is balanced by viscous stress, as described by the creeping flow equation 2.6.
This balance leads to increasing fluid velocities at greater distances from the surface. Further away, where the force density is lower, the required velocity gradients are smaller. Outside the double layer, in the absence of net forces, the velocity gradient is zero, and the fluid velocity assumes a constant value. Overall, the force exerted on the fluid within the double layer drags the entire bulk of the fluid along with it, far beyond the double layer.

2.3.2 Validity of the Poisson-Boltzmann Equation

We rederive the Poisson-Boltzmann equation for the non-equilibrium case depicted in Figure 2.3, confirming that the equilibrium double-layer structure is still applicable. Although the following derivation is based on certain assumptions, we note that the solution we provide is exact and does not rely on approximations.
Due to the system's symmetry, we assume that ion transport occurs solely parallel to the plane, aligning with the external electric field. Consequently, the ion fluxes $\boldsymbol{j}^+$ and $\boldsymbol{j}^-$ are directed exclusively in the y-direction, as shown in Figure 2.3a. Analogous to the equilibrium case, the x-components of the ion fluxes, j_x^+ and j_x^-, are zero:

$$j_x^+ = 0 = -\frac{\partial c^+}{\partial x} + \frac{e}{k_B T} c^+ \frac{\partial \Phi}{\partial x} \tag{2.24}$$

$$j_x^- = 0 = -\frac{\partial c^-}{\partial x} - \frac{e}{k_B T} c^- \frac{\partial \Phi}{\partial x}. \tag{2.25}$$

As these equations are identical to those in the equilibrium solution as presented in section 2.2, the ion concentrations are again Boltzmann distributed. However, the potential $\Phi(x, y)$ now depends on both x and y due to the externally applied electric field. At distances far from the charged plane, the potential is expected to vary solely due to the applied electric field E_0, leading to the modified boundary condition $\varphi(\infty, y) = \varphi(y) = -E_0 y$. Additionally, we require again that the ion concentrations c^+ and c^- far from the plane remain at the constant value c. Upon applying the revised boundary conditions, we arrive at the following expressions for the ion concentrations:

$$c^+ = c e^{\frac{-e(\Phi - \varphi(y))}{k_B T}} = c e^{\frac{-e(\Phi + E_0 y)}{k_B T}} \tag{2.26}$$

$$c^- = c e^{\frac{+e(\Phi - \varphi(y))}{k_B T}} = c e^{\frac{+e(\Phi + E_0 y)}{k_B T}}. \tag{2.27}$$

We now revisit the Poisson equation to find an expression for the potential Φ.

$$\epsilon\left(\frac{\partial^2\Phi}{\partial x^2}+\frac{\partial^2\Phi}{\partial y^2}\right)=-e(c^+-c^-)=2ec\sinh\left(\frac{e(\Phi+E_0y)}{k_BT}\right) \tag{2.28}$$

We make the plausible assumption that the potential can be expressed as $\Phi(x,y) = \Psi(x)+\varphi(y)=\Psi(x)-E_0y$. This assumption is motivated by the definition of Ψ used to solve the equilibrium Poisson equation. Ψ represents again the potential difference between positions within the double layer and bulk, defined as $\Psi(x)=\Phi(x,y)-\varphi(y)$ with $\Psi(\infty)=\Phi(\infty,y)-\varphi(y)=0$. Substituting the assumed form of $\Phi(x,y)$ into the equation and acknowledging that $\frac{\partial^2(-E_0y)}{\partial x^2}=0$ and $\frac{\partial^2(-E_0y)}{\partial y^2}=0$, we reduce the equation to the one-dimensional Poisson-Boltzmann equation:

$$\frac{\partial^2\Psi}{\partial x^2}=\frac{2ec}{\epsilon}\sinh\left(\frac{e\Psi}{k_BT}\right) \tag{2.29}$$

The reappearance of the one-dimensional Poisson-Boltzmann confirms that the double layer structure remains unaltered. The zeta potential ζ can still be calculated from the surface charge via the Graham equation presented in subsection 2.2.3 and the charge distribution is again given by $\rho_e=-\epsilon\frac{\partial^2\Psi}{\partial x^2}$. Note that the potential at the charged surface is now given by $\Phi(0,y)=\zeta+\varphi(y)=\zeta-E_0y$. The zeta potential ζ represents again the difference between the bulk potential and the surface potential.

2.3.3 Derivation of the Flow Profile

The flow profile can be computed using the creeping flow equation, as stated in Equation 2.6, which incorporates a Coulomb force density, expressed as $\rho_e\boldsymbol{E}$. To determine expressions for the charge density ρ_e and the electric field $\boldsymbol{E}$, we must solve Equation 2.29. This will yield an expression for $\Phi(x,y)$, enabling us to compute the electric field as $\boldsymbol{E}=-\boldsymbol{\nabla}\Phi(x,y)$ and the charge density as $\rho_e=-\epsilon\Delta\Phi(x,y)$. However, it will become evident that we do not require an explicit expression for $\Phi(x,y)$.

As illustrated in the previous section, the potential $\Phi(x,y)$ can be expressed as a superposition of an x-varying component $\Psi(x)$, representing the double layer structure, and a y-dependent part $\varphi(y)$, resulting from the external electric field. By using $\Phi(x,y)=\Psi(x)+\varphi(y)=\Psi(x)-E_0y$, we derive the Coulomb force density as

$$\rho_e\boldsymbol{E}=\epsilon\Delta\left(\Psi(x)-E_0y\right)\boldsymbol{\nabla}\left(\Psi(x)-E_0y\right)=\epsilon\frac{\partial^2\Psi}{\partial x^2}\frac{\partial\Psi}{\partial x}\boldsymbol{e_x}-\epsilon\frac{\partial^2\Psi}{\partial x^2}E_0\boldsymbol{e_y} \tag{2.30}$$

with the unit vectors $\boldsymbol{e_x}$ and $\boldsymbol{e_y}$ in the x and y directions, respectively.

Let us now consider the y-component of the creeping flow equation along with the y-component of the Coulomb force:

$$\eta \frac{\partial^2 v_y}{\partial x^2} = \epsilon \frac{\partial^2 \Psi}{\partial x^2} E_0 \tag{2.31}$$

It should be noted that we have made the assumption that both v_y and P are independent of the y-coordinate, resulting in $\frac{\partial^2 v_y}{\partial y^2} = 0$ and $\frac{\partial P}{\partial y} = 0$. This implies that neither velocity nor pressure varies along the surface. We will revisit this assumption in subsection 2.3.4. Upon integrating the above equation twice, we obtain

$$\eta v_y(x) = \epsilon \Psi(x) E_0 + Ax + B \tag{2.32}$$

where A and B are integration constants, which will be determined by the boundary conditions. As defined in Section 2.3.2, Ψ represents the potential difference between positions within the double layer and the bulk. Therefore, we find $\Psi(\infty) = \Phi(\infty, y) - \varphi(y) = 0$ at a location far away from the charged surface. Additionally, it is required that the velocity reaches a finite value at infinity, denoted by $v_y(\infty) = v_\infty$. Applying these boundary condition yields $\eta v_y(\infty) = 0 + A \cdot \infty + B = \infty$. Consequently, for finite $v_y(\infty) = v_\infty$, it is necessary that $A = 0$. With this, the value of B is determined as $B = \eta v_\infty$.

Directly at the stationary surface the fluid is at rest, which yields a now slip boundary condition, expressed as $v(y) = 0$. Further we have $\Psi(0) = \zeta$ which is the definition zeta potential. By applying these two conditions and utilizing the values for B and A, we obtain $0 = \epsilon \zeta E_0 + \eta v_\infty$. Solving for v_∞ yields

$$v_\infty = -\frac{\epsilon \zeta}{\eta} E_0. \tag{2.33}$$

The above equation is usually referred to as the Helmholtz-Smoluchowski slip boundary condition [3, 43]. It relates the velocity far away from the surface, v_∞, to the zeta potential, ζ, which in turn can be computed using the Graham equation shown in subsection 2.2.3 from the surface charge σ and the ion concentration c. The equation will be further discussed in Section 2.4, specifically regarding its use as a boundary condition for hydrodynamic flows in macroscopic systems.

Finally, with the expression for v_∞, the flow profile is given by

$$v_y(x) = \frac{\epsilon}{\eta} \left(\Psi(x) - \zeta\right) E_0 \tag{2.34}$$

The flow profile is sketched in Figure 2.3d, and an explicit expression for $\Psi(x)$ can be obtained by solving Equation 2.19.

2.3.4 Systematic Approach to the Creeping Flow Equation

We conclude our discussion by addressing the systematic approach to solving the creeping flow equation, as motivated by references [40] and [32]. Typically, one starts by deriving an explicit expression for the pressure P. A differential equation that exclusively involves the pressure and the Coulomb force density can be found by applying the divergence operator $\boldsymbol{\nabla}$ to the creeping flow equation 2.6. Given the incompressibility condition $\boldsymbol{\nabla} \cdot \boldsymbol{v} = 0$, the term involving velocity becomes $\boldsymbol{\nabla} \cdot \Delta \boldsymbol{v} = \Delta \boldsymbol{\nabla} \cdot \boldsymbol{v} = 0$. Consequently, we are left with

$$\Delta P = \boldsymbol{\nabla} \left(\rho_e \boldsymbol{E}\right) \tag{2.35}$$

By substituting the expression from equation 2.30 for $\rho_e \boldsymbol{E}$, we obtain

$$\Delta P = \left(\frac{\partial^2 P}{\partial x^2} + \frac{\partial^2 P}{\partial y^2}\right) = \epsilon \frac{\partial}{\partial x} \left(\frac{\partial^2 \Psi}{\partial x^2} \frac{\partial \Psi}{\partial x}\right) \tag{2.36}$$

Since the right-hand side of the equation depends only on $\Psi(x)$, a function of x alone, we can assume P to be independent of y.

$$\frac{\partial^2 P}{\partial x^2} = \epsilon \frac{\partial}{\partial x} \left(\frac{\partial^2 \Psi}{\partial x^2} \frac{\partial \Psi}{\partial x}\right) \tag{2.37}$$

Importantly, this assumption aligns with the expectation that the pressure far from the charged surface remains constant, as we assume no external pressure gradient parallel to the charged plane.

After performing one integration and applying the Poisson-Boltzmann equation 2.28 to substitute for $\frac{\partial^2 \Psi}{\partial x^2}$, we arrive at the following equation:

$$\frac{\partial P}{\partial x} = \epsilon \frac{\partial^2 \Psi}{\partial x^2} \frac{\partial \Psi}{\partial x} + A = 2ec \sinh\left(\frac{e\Psi}{k_B T}\right) \frac{\partial \Psi}{\partial x} + A \tag{2.38}$$

Here, A represents an integration constant, which is zero as we require a constant pressure

far from the plane, leading to $\frac{\partial P}{\partial x}\big|_{\infty} = 0$. Furthermore, utilizing $\Psi(\infty) = 0$ results in $0 = 2ec\sinh(0) + A = 0 + A$, which yields $A = 0$.

This brings us back to the equation from which we began deriving the equilibrium pressure distribution in Section 2.2.4. This implies that the pressure distribution is identical to that in the equilibrium case.

Next, we need to substitute the explicit expression for the pressure gradient, $\boldsymbol{\nabla} P$, into the creeping flow equation to deduce an expression for the velocity. Starting with the x-component, we obtain

$$0 = \eta \left(\frac{\partial^2 v_x}{\partial x^2} + \frac{\partial^2 v_x}{\partial y^2} \right) - \frac{\partial P}{\partial x} + \epsilon \frac{\partial^2 \Psi}{\partial x^2} \frac{\partial \Psi}{\partial x} \tag{2.39}$$

Using our expression for $\frac{\partial P}{\partial x}$ from equation 2.38, we find $0 = \eta \left(\frac{\partial^2 v_x}{\partial x^2} + \frac{\partial^2 v_x}{\partial y^2} \right)$. A valid solution for v_x which stratifies the boundary condition $v_x(0, y) = 0$ which means that there is no liquid flux perpendicular into the charged plane is simply $v_x(x, y) = 0$. This assumption can be also motivated by the symmetry of the system. The incompressibility condition $\frac{\partial v_x}{\partial x} + \frac{\partial v_y}{\partial y} = 0$ then implies $\frac{\partial v_y}{\partial y} = 0$.

Turning to the y-component, we find

$$0 = \eta \left(\frac{\partial^2 v_y}{\partial x^2} + \frac{\partial^2 v_y}{\partial y^2} \right) - \frac{\partial P}{\partial y} - \epsilon \frac{\partial^2 \Psi}{\partial x^2} E_0. \tag{2.40}$$

Given that we have already established the pressure as independent of y, it follows that $\frac{\partial P}{\partial y} = 0$. Additionally, we deduced $\frac{\partial v_y}{\partial y} = 0$, which implies $\frac{\partial^2 v_y}{\partial y^2} = 0$. With these considerations, we arrive at the same equation used to determine the flow profile, already solved in Section 2.31:

$$\eta \frac{\partial^2 v_y}{\partial x^2} = \epsilon \frac{\partial^2 \Psi}{\partial x^2} E_0. \tag{2.41}$$

2.4 Electrophoresis

In this section, we discuss the electrophoresis of micrometer-sized charged particles enveloped by counterion cloud, forming a comparably thin electric double layer. Our analysis begins with a conceptual discussion, comparing the flow field around a spherical particle undergoing electrophoresis with and without a counterion cloud. We base our discussion on the flow field plots presented in reference [44] and the derivation of Stokes' law as found in hydrodynamic textbooks [45].

Subsequently, we mathematically explore the scale of the electric double layer surrounding the particle. This analysis enables us to derive approximate equations for calculating the

hydrodynamic flow field and the migration velocity of the particle. We then compute the force balance on the particle and demonstrate, as in reference [8], that the migration velocity is independent of the particle's shape.

2.4.1 Conceptual Discussion

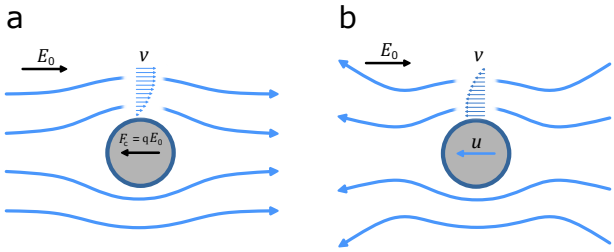

Figure 2.4. Flow profile around a negatively charged sphere being dragged through a liquid by an electric field E_0, in the absence of counter ions. The flow velocity perpendicular to the migration direction at the particle's equator is indicated with arrows. **a** Co-moving frame of reference. **b** Stationary, laboratory frame of reference.

We begin with a simple extreme case: a charged sphere is dragged through a liquid devoid of electrolytes by an electric field. In this scenario, the sphere experiences a Coulomb force, denoted as $F_c = qE_0$, where q represents the sphere's total charge, and E_0 is the externally applied electric field. The sphere moves at a constant speed through the liquid, and the Coulomb force is counteracted by a viscous friction force, expressed by $F_r = -6\pi\eta R u$. This friction force, commonly referred to as Stokes' law, points in the opposite direction to the migration velocity u. The force balance equation, $0 = F_c + F_r = qE_0 - 6\pi\eta R u$, subsequently provides an expression for the migration velocity: $u = \frac{q}{6\pi\eta R} E_0$.

Mechanistically, the viscous friction force originates from fluid elements sliding along the surface of the migrating sphere. The viscous stress σ at the surface, defined as the tangential force per unit area, is linked to the fluid velocity gradient $\frac{\partial v_y}{\partial x}$ between the solid surface and the adjacent fluid elements. Mathematically, it is expressed as $\tau = \eta \left.\frac{\partial v_y}{\partial x}\right|_{x=0}$, where x is a coordinate normal to the surface and y is tangential to it. Deriving Stokes' law involves first solving the creeping flow equation to determine the velocity profile of a sphere migrating at constant velocity. The total viscous friction force is then calculated by integrating the viscous stress τ over the sphere's entire surface.

The flow profile is depicted in Figure 2.4. Figure 2.4a illustrates the flow profile from the perspective of a negatively charged sphere at rest in a constant external fluid flow.

Here, the Coulomb force, and hence the migration direction, points left, opposite to the applied electric field. The flow velocity v at the sphere's surface is zero, increasing with distance from the sphere until it reaches a constant value, corresponding to the negative of the migration velocity u. From this frame of reference, the flow lines bend around the particle. Figure 2.4b presents the same scenario from a laboratory frame, showing the flow lines of a migrating sphere from an external observer's viewpoint at a given moment. In this view, the sphere pushes fluid in front of it and drags some fluid behind it. The flow velocity at the surface perpendicular to its migration direction equals the sphere's migration velocity u, decaying to zero at greater distances from the surface.

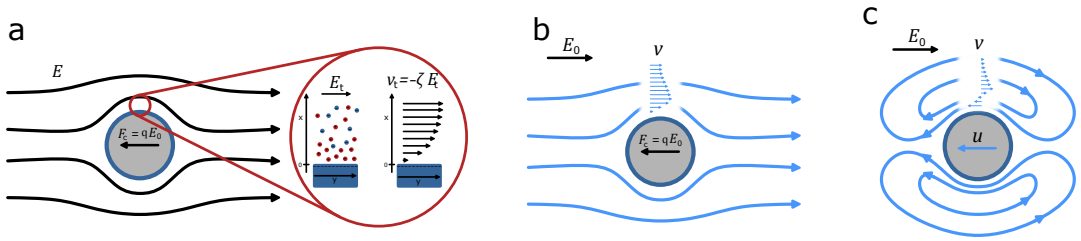

Figure 2.5. Flow profile and electric field around a negatively charged sphere being dragged through a liquid by an electric field E_0, in the presence of counter ions. The flow velocity perpendicular to the migration direction at the particle's equator is again indicated with arrows. (a) Electric field in the vicinity of the particle. The particle appears electroneutral on the displayed scale, and the electric field bends around the particle. The inset shows the situation zoomed in to the particle surface, which is similar to the case of electroosmosis. (b) Flow profile in a co-moving frame of reference. (c) Flow profile in a stationary, laboratory frame of reference.

Next, we consider another extreme scenario: a charged sphere is now dragged through a liquid containing an electrolyte at a sufficiently high concentration such that the electric double layer's extension is significantly smaller than the particle's size. As discussed in Section 2.2 for the charged plane, counterions accumulate near the particle's charged surface, effectively screening the surface charge. Figure 2.5a depicts a sphere subject to an external electric field, viewed from the sphere's frame of reference. On the depicted macroscopic scale, the particle appears electrically neutral. The electric field bends around the non-conducting sphere, thereby dragging ions around it. Near the surface, the electric field is tangential to the surface, as ions cannot penetrate the sphere. The inset in Figure 2.5a depicts the situation at the surface. At the scale of the Debye length, the charged surface appears locally flat. Additionally, the tangential electric field E_t is approximately constant at this scale. This local scenario is analogous to the case of electroosmosis discussed in Section 2.3. The tangential electric field acts on the accumulated counterions near the charged surface, inducing liquid motion. Concurrently, the tangential

electric field also acts on the surface charge, resulting in a total Coulomb force expressed as $F_c = qE_0$.

Compared to the case without an electrolyte, there is now a Coulomb body force acting on the liquid near the surface, which induces liquid motion in the opposite direction to the particle's migration direction. This effect increases the viscous drag force on the particle and therewith reduces the migration velocity. Figure 2.5b illustrates the flow profile around the sphere from the particle's frame of reference. The flow field appears qualitatively similar to that in Figure 2.4a for the case without counterions. However, near the surface, the fluid velocity increases rapidly with distance within the electric double layer due to the force on the counterions. Outside the electric double layer, the velocity reaches a maximum and then decays with distance until it reaches a constant value, which is again the negative of the migration velocity. In Figure 2.5c, we depict the same scenario from the laboratory frame of reference. At the surface perpendicular to its migration direction, the flow field matches the sphere's migration velocity u. The flow velocity decreases rapidly in the double layer and even reverses direction within the electric double layer. Beyond the double layer, the liquid flows in the opposite direction to the sphere's migration. Far away, the flow velocity decays to zero. As the sphere drags fluid in one direction and the Coulomb body force in the double layer acts in the opposite direction, the liquid circulates around the particle, as indicated in the figure.

2.4.2 Derivation of the Migration Velocity

To compute the migration velocity, we adopt an approach similar to that used for the case without counterions. In this section, we solve the Stokes equation, now incorporating a Coulomb body force, to determine the flow profile around the sphere. Subsequently, we calculate the viscous stress at the surface and balance it with the Coulomb force to establish an expression for the migration velocity.

We derive an approximate solution for the flow profile around a sphere by utilizing the small scale of the electrical double layer. This allows us to solve the governing equations from Section 2.1 in two distinct regions: an outer region, on the particle's scale, and an inner region, within the electrical double layer. Inside the double layer at a microscopic scale, the situation resembles that in electroosmosis. On a macroscopic scale, the charged particle appears electroneutral, as the surface charge is screened by the counterions in the

electric double layer. This solution strategy is commonly known as the thin double layer approximation [12–14, 32, 37].

We begin the discussion by motivating the separation of scales through the reformulation of the Poisson equation in dimensionless variables. The Poisson equation is expressed as

$$-\epsilon\Delta\Phi = \rho_e = e(c^+ - c^-). \tag{2.42}$$

We define $\hat{\boldsymbol{r}} = R\boldsymbol{r}$ as the dimensionless distance, $\hat{\Phi} = \frac{e\Phi}{k_B T}$ as the dimensionless potential, and $\hat{c^{\pm}} = c_0 c^{\pm}$ as the dimensionless concentration, where c_0 is the ion concentration far from any charged surface in the bulk. This leads us to

$$-\frac{\frac{\epsilon k_B T}{e^2 c_0}}{R^2}\Delta\hat{\Phi} = -\frac{2\lambda_D^2}{R^2}\Delta\hat{\Phi} = (\hat{c^+} - \hat{c^-}) \tag{2.43}$$

where we identify the Debye length as $\lambda_D = \sqrt{\frac{\epsilon k_B T}{2e^2 c_0}}$. When the Debye length is significantly shorter than the particle size, i.e., the radius, we find $\frac{2\lambda_D^2}{R^2} \approx 0$, leading to $\hat{c^+} - \hat{c^-} = 0$. We conclude that on a macroscopic scale, the concentrations of positive and negative ions are approximately equal, suggesting electro-neutrality. Returning to the original variables, we find $c^+ = c^- = c$, far from the charged surface.

On a microscopic scale close to the particle surface, we find the situation depicted in the inset in Figure 2.5a. At the scale of the Debye length, the charged surface appears locally flat. Additionally, the tangential electric field E_t is approximately constant at this scale. This local scenario is analogous to the case of electroosmosis discussed in Section 2.3. We can use the same approach to determine the ion concentration distribution close to the surface. From the fact that the ion flux normal to the surface is zero, we find again $c^+ = ce^{\frac{-e(\Phi-\varphi(y))}{k_B T}}$ and $c^- = ce^{\frac{+e(\Phi-\varphi(y))}{k_B T}}$.
$\varphi(y)$ and c represent the potential and ion concentration far away from the charged surface, respectively, which is outside the double layer. Assuming that the tangential electric field E_t is approximately constant on the scale of the double layer, we approximate $\varphi(y)$ as $\varphi_0 - E_t y$. This expression, $\varphi_0 - E_t y$, is the Taylor expansion of the potential outside the double layer at the specified position on the sphere. Substituting the ion concentrations back into the Poisson equation yields

$$\epsilon\left(\frac{\partial^2\Phi}{\partial x^2} + \frac{\partial^2\Phi}{\partial y^2}\right) = 2ec\sinh\left(\frac{e(\Phi - \varphi_0 + E_t y)}{k_B T}\right) \tag{2.44}$$

As before, we reintroduce the potential difference $\Psi = \Phi - \varphi_0 + E_t y$, leading to

$$\frac{\partial^2 \Psi}{\partial x^2} = 2\frac{ec}{\epsilon} \sinh\left(\frac{e\Psi}{k_B T}\right). \tag{2.45}$$

The equation can be solved as before and can be used to determine the zeta potential ζ via the Graham equation 2.20 from the surface charge. To obtain a complete solution of the potential valid in all regions, we require that the value of the inner solution at infinity matches the value of the outer solution at the particle surface. Note that the complete solution of the potential can be expressed as a single function by $\Phi_{combined} = \Psi + \varphi$. Here, we need to use the expression for the potential Φ outside the double layer for φ. However, one must replace x with $r - R$ in Ψ to align the coordinates.

We can now proceed to compute the local flow profile using the creeping flow equation, as in Section 2.3. The flow profile for a charged flat surface is given by

$$v_y(x) = \frac{\epsilon}{\eta} \left(\Psi(x) - \zeta\right) E_t \tag{2.46}$$

Far away from the surface where $\Psi(\infty) = 0$, the velocity approaches the value $v_t = -\frac{\epsilon\zeta}{\eta} E_t$. Similarly to the potential, we must also match the velocity value obtained at infinity with the solution of the velocity profile outside the double layer. v_t will serve as an effective boundary condition for the tangential velocity outside the double layer for the creeping flow equation.

Having established the solutions inside the double layer, we can now turn to the solution outside the double layer at a macroscopic scale. We use the previously derived electroneutrality condition to obtain an approximate equation for the ion flux equations. By defining $c = c^+ = c^-$, we find

$$\boldsymbol{j}^+ = -D^+ \boldsymbol{\nabla} c - D^+ \frac{e}{k_B T} c \boldsymbol{\nabla} \Phi + c\boldsymbol{v} \tag{2.47}$$

and

$$\boldsymbol{j}^- = -D^- \boldsymbol{\nabla} c + D^- \frac{e}{k_B T} c \boldsymbol{\nabla} \Phi + c\boldsymbol{v}. \tag{2.48}$$

The electric current density is defined by $\boldsymbol{j_e} = e\left(\boldsymbol{j}^+ - \boldsymbol{j}^-\right)$ and can be expressed as

$$\boldsymbol{j_e} = -(D^+ - D^-) \boldsymbol{\nabla} c - (D^+ + D^-) \frac{e}{k_B T} c \boldsymbol{\nabla} \Phi. \tag{2.49}$$

Assuming that the ion concentration c is constant, we can simplify the equation to

$$\boldsymbol{j_e} = -(D^+ + D^-)\frac{e}{k_B T} c \boldsymbol{\nabla}\Phi, \tag{2.50}$$

which corresponds to Ohm's law for two-component electrolytes. Aiming for a steady-state solution, the conservation laws dictate $\boldsymbol{\nabla} \boldsymbol{j}^+ = 0$ and $\boldsymbol{\nabla} \boldsymbol{j}^- = 0$, which also implies $\boldsymbol{\nabla} \boldsymbol{j_e} = 0$. Applying $\boldsymbol{\nabla}$ to the above equation yields a Laplace equation for the electric potential:

$$\Delta\Phi = 0. \tag{2.51}$$

To solve for the potential, we need to impose boundary conditions. In the following, we will use spherical coordinates. We assume that the charged sphere is exposed to an electric field with the constant value E_0, pointing in the z-direction. Therefore, the potential far away from the sphere should assume the value $-E_0 z = -E_0 r\cos(\theta)$, where θ is the polar angle in spherical coordinates. At the surface of the particle, we assume that no ions can enter the double layer. This yields the boundary condition $\boldsymbol{e_r} \boldsymbol{j_e} = 0$ for the current, which also implies $-\boldsymbol{e_r}\boldsymbol{\nabla}\Phi|_{r=R} = 0$. The solution satisfying these boundary conditions is a combination of an electric dipole and the constant external electric field:

$$\Phi = -\frac{1}{2} E_0 \frac{R^3}{r^2}\cos(\theta) - E_0 r\cos(\theta). \tag{2.52}$$

The corresponding electric field is given by

$$\boldsymbol{E} = E_0\cos(\theta)\left(1 - \frac{R^3}{r^3}\right)\boldsymbol{e_r} - E_0\sin(\theta)\left(\frac{R^3}{2r^3} + 1\right)\boldsymbol{e_\theta}. \tag{2.53}$$

The tangential component of the electric field at $r = R$ is given by $E_t = -1.5\sin(\theta)E_0$.

We can now proceed to solve the velocity profile outside the double layer. As mentioned earlier, the value of the velocity of the inner solution at infinity, given by $v_t = -\frac{\epsilon\zeta}{\eta}E_t$, will serve as an effective boundary condition for the tangential component of the velocity profile outside the double layer. With the expression for the tangential electric field, this results in $v_t = 1.5\frac{\epsilon\zeta}{\eta}\sin(\theta)E_0$. The normal component of the fluid velocity is zero since fluid can not enter the particles surface. Furthermore, we require that the velocity far away from the particle approaches a constant value, pointing in the z-direction. It turns out that a valid solution of the creeping flow equation, satisfying these boundary conditions,

is given by

$$\boldsymbol{v} = -\frac{\epsilon\zeta}{\eta}\boldsymbol{E} = -\frac{\epsilon\zeta}{\eta}E_0\left(\cos(\theta)\left(1-\frac{R^3}{r^3}\right)\boldsymbol{e_r} - \sin(\theta)\left(\frac{R^3}{2r^3}+1\right)\boldsymbol{e_\theta}\right). \tag{2.54}$$

Far away from the sphere, the velocity is given by $-\frac{\epsilon\zeta}{\eta}E_0\boldsymbol{e_z}$. Changing the frame of reference yields the migration velocity:

$$u = \frac{\epsilon\zeta}{\eta}E_0. \tag{2.55}$$

Note that the migration direction for a negatively charged particle with a negative surface potential ζ points in the opposite direction as the electric field.
Finally, it should be mentioned that it is not immediately apparent that the presented value for u is indeed the migration velocity. We could construct other valid solutions to the Stokes equation by adding another solution of the creeping flow equation, which is the solution used to derive Stokes' law. The boundary conditions would still be satisfied since the Stokes flow at the particle surface is zero and has a constant value far away from the sphere. To select the correct solution, we need to consider the force balance on the particle surface. However, it will ultimately be revealed that the expression previously given is, in fact, the migration velocity.

2.4.3 Force Balance

To establish the force balance of the particle, we need to compute the viscous stress at the particle's surface and equate it with the Coulomb force due to the particle's surface charge σ [46]. We begin by computing the viscous stress from the solution of the velocity profile presented above.
Near the surface, the flow profile can be expressed as $v_y(x) = \frac{\epsilon}{\eta}\left(\Psi(x)-\zeta\right)E_t$. The viscous stress τ at the surface is derived from the velocity profile by

$$\tau = \eta\left.\frac{\partial v_y}{\partial x}\right|_{x=0} = \epsilon\left.\frac{\partial\Psi(x)}{\partial x}\right|_{x=0}E_t. \tag{2.56}$$

The term $-\left.\frac{\partial\Psi(x)}{\partial x}\right|_{x=0}$ represents the electric field perpendicular to the surface, which relates to the surface charge as $-\epsilon\left.\frac{\partial\Psi(x)}{\partial x}\right|_{x=0} = \sigma$. Thus, the viscous stress is $\tau = -\sigma E_t$. The term σE_t represents the Coulomb force per unit area acting on the charged surface, equivalent to the stress or surface tension due to the Coulomb force. This implies that the viscous stress at the surface is exactly balanced by the Coulomb stress at the surface:

$0 = \tau + \sigma E_t$. This result has some interesting implications. Firstly, it confirms that the solution presented above is correct and that the migration speed is indeed given by $\frac{\epsilon\zeta}{\eta}E_0$. Secondly, this result implies that there is no internal stress within the particle, suggesting that a soft particle is not expected to deform during migration in an electric field.

2.4.4 Shape Independence

In this section, we will establish that electrophoresis, under the thin double layer approximation, is shape-independent [8]. First, we will reexamine the effective boundary conditions for the electric field and the velocity profile outside the electric double layer. The normal component of the electric field at the particle surface is zero, as no current enters the double layer. This condition is expressed as $-\boldsymbol{e_r} \cdot \boldsymbol{\nabla}\Phi|_{r=R} = 0$. Similarly, the normal component of the fluid velocity is also zero since fluid cannot enter the particle surface. This is expressed as $\boldsymbol{e_r} \cdot \boldsymbol{v}|_{r=R} = 0$. Furthermore, far away from the particle, the electric field is constant and points in the z-direction, assuming the value $E_0\boldsymbol{e_z}$. Similarly, the velocity profile far away from the particle is expected to be constant and pointing in the z-direction, assuming the value $-u\boldsymbol{e_z}$, where u is the migration velocity of the particle. The tangential component of the flow velocity at the particle surface is linked to the tangential electric field by $\boldsymbol{v_t} = -\frac{\epsilon\zeta}{\eta}\boldsymbol{E_t}$.
Let's now assume an arbitrarily shaped particle. The electric potential Φ will be a solution of the Laplace equation $\Delta\Phi = 0$, satisfying the stated boundary conditions for the electric field. Assuming the velocity field to be $\boldsymbol{v} = -\frac{\epsilon\zeta}{\eta}\boldsymbol{E}$ automatically satisfies the boundary conditions for the velocity. Both fields have only a tangential component at the particle surface, which is related via the factor $-\frac{\epsilon\zeta}{\eta}$, and they assume a constant value, pointing in the z-direction, far away from the particle. Therefore, the flow velocity far away from the particle is given by $u = -\frac{\epsilon\zeta}{\eta}E_0$.
What remains is to demonstrate that the constructed solution is indeed a solution of the creeping flow equation. Inserting $\frac{\epsilon\zeta}{\eta}\boldsymbol{\nabla}\Phi$ into the creeping flow equation yields

$$\frac{\epsilon\zeta}{\eta}\Delta\left(\boldsymbol{\nabla}\Phi\right) - \boldsymbol{\nabla}P = 0. \tag{2.57}$$

We can use $\Delta\left(\boldsymbol{\nabla}\Phi\right) = \boldsymbol{\nabla}\left(\Delta\Phi\right) = 0$, which leaves us with $\boldsymbol{\nabla}P = 0$. This shows that the proposed solution solves the creeping flow equation and that the pressure is constant everywhere. Finally, we need to mention that the local balance of viscous stress and Coulomb stress at the particle surface, proven in section 2.4.3, is a necessary condition for the shape independence of electrophoresis. This ensures that the above solution

is indeed the correct solution of the creeping flow equation, satisfying force balance of viscous friction and Coulomb force, independent of the particle's shape. Lastly, shape independence combined with the local stress balance implies that there is no hydrodynamic interaction force between two particles migrating next to each other in an electric field. The argumentation above applies also to multiple similar particles subject to an electric field. In this case, the potential is still a solution of the Laplace equation, and the hydrodynamic flow field is directly proportional to the electric field. Furthermore, on each particle's surface, there is the local stress balance between Coulomb and hydrodynamic forces. Consequently, particles migrate independently of each other. However, particles are still expected to interact with each other through the distortion of the external electric field.

2.4.5 AC Electric Fields

The derivation of the migration velocity can be extended to time-varying external electric fields. Time dependence is introduced into the governing equations, as detailed in Section 2.1, solely through the conservation laws for ion species, represented by $\frac{\partial c^+}{\partial t} + \boldsymbol{\nabla} \boldsymbol{j}^+ = 0$ and $\frac{\partial c^-}{\partial t} + \boldsymbol{\nabla} \boldsymbol{j}^- = 0$. The electroneutrality approximation outside the double layer, expressed as $c^- = c^+ = c$, leads to the equation for electric current density $\boldsymbol{\nabla} \boldsymbol{j_e} = e\boldsymbol{\nabla} \boldsymbol{j}^+ - e\boldsymbol{\nabla} \boldsymbol{j}^- = 0$, mirroring the steady-state result. Consequently, the potential adheres to a Laplace equation in this scenario, similar to the steady-state case, when assuming a constant ion concentration c throughout. Further assuming that the electric double layer at the particle surface maintains its equilibrium structure, we encounter the same mathematical problem as in the steady-state case. The AC-electric solution for the flow field and the electric field can be derived by substituting E_0 with $\sin(\omega t)E_0$ in the corresponding expressions from Section 2.4.2.
This result, combined with the proven shape independence discussed in Section 2.4.4, suggests that particles of any shape experience no net movement in an AC electric field. However, particles are expected to align with the electric field due to the induced electric dipole. Also, electric particle-particle interactions are still expected.

2.5 Diffusioosmosis

In this section, we discuss diffusioosmosis in electrolyte solutions. Diffusioosmosis describes the motion of a liquid above a surface, induced by a concentration gradient. Initially, we will provide a conceptual discussion to explain the relevant forces involved [46].

Subsequently, we will derive the diffusiophoretic flow field within a thin electric double layer [18, 19, 40, 43]. We will then discuss the emergence of diffusion-induced electric fields and deduce an effective boundary condition for hydrodynamic flows above charged surfaces.

2.5.1 Conceptual Discussion

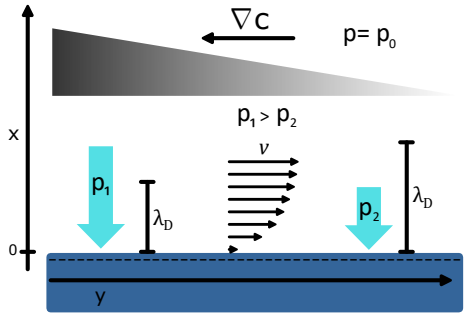

Figure 2.6. Schematic illustration of diffusioosmotic flow. A charged plane is submerged in an electrolyte with a concentration gradient $\boldsymbol{\nabla} c$, depicted with differing gray values, along the plane in the y-direction. The hydrostatic pressure p and Debye length λ_D are indicated with blue arrows at two different positions. The pressure difference causes flow v from high-pressure to low-pressure regions.

Consider the scenario depicted in Figure 2.6, where a charged plane is submerged in an electrolyte with a concentration gradient along the plane in the y-direction. Adjacent to the surface, there exists an electric double layer whose size varies along the surface due to its dependency on the bulk ion concentration. This size variation is represented in the Figure by two different Debye lengths, λ_D, along the surface. Additionally, the hydrostatic pressure within the double layer changes with the ion concentration in the bulk. This pressure results from the force exerted by the attracted counterions on the liquid. Higher ion concentrations outside the double layer correspond to higher concentrations inside, leading to increased pressures within it. The variation in hydrostatic pressure along the surface is depicted in the Figure by the two pressure values, p_1 and p_2, at different positions. It is important to note that the pressure outside the double layer remains constant at p_0. The differential pressure induces liquid motion, v, within the electric double layer, moving from high to low pressure regions as indicated. This motion drives bulk liquid from areas of higher salt concentrations to those with lower concentrations. This scenario is applicable only when ions have equal diffusion constants. In cases where ions have asymmetric diffusion constants, an additional diffusion-induced electric field arises, leading to more electroosmotic flow. This general scenario is further discussed in Section 2.5.4.

2.5.2 Surface Pressure-Driven Diffusioosmosis

We will now derive the velocity profile within the double layer in response to an externally applied concentration gradient of an electrolyte with symmetric diffusion constants, following the approach of [32]. Note that this derivation is an approximation, applicable only within a local region of the electric double layer where the external gradient appears to vary slowly, thus preserving its equilibrium structure. Assuming no ion fluxes perpendicular to the plane, we can derive Boltzmann distributions for the ion concentrations. Consequently, the Poisson equation can be expressed as

$$\epsilon\left(\frac{\partial^2\Phi}{\partial x^2}+\frac{\partial^2\Phi}{\partial y^2}\right)=2ec(y)\sinh\left(\frac{e(\Phi-\varphi_0)}{k_BT}\right), \tag{2.58}$$

where $c(y)$ represents the ion concentration outside the double layer, varying along the y-axis. We introduce dimensionless variables to approximate the potential $\Phi(x,y)$. We consider x-distances on the scale of the electric double layer, introducing $x=\lambda_0\hat{x}$ where λ_0 is a constant with the scale of the Debye length. Similarly, we introduce y-distances on the scale of the concentration gradient, defining $y=R\hat{y}$ where R is a distance much larger than the Debye length λ_D. We also introduce the dimensionless potential $\hat{\Phi}=\frac{e(\Phi)}{k_BT}$ and its dimensionless value far from the plane, $\hat{\varphi_0}=\frac{e(\varphi_0)}{k_BT}$, and use the definition $\hat{c(y)}=c_0c(y)$ where c_0 is a reference concentration outside the double layer which we set to $c(0)$. With these definitions, we arrive at

$$\frac{\frac{\epsilon k_BT}{2e^2c_0}}{\lambda_0^2}\frac{\partial^2\hat{\Phi}}{\partial\hat{x}^2}+\frac{\frac{\epsilon k_BT}{2e^2c_0}}{R^2}\frac{\partial^2\hat{\Phi}}{\partial\hat{y}^2}=\frac{\lambda_0^2}{\lambda_0^2}\frac{\partial^2\hat{\Phi}}{\partial\hat{x}^2}+\frac{\lambda_0^2}{R^2}\frac{\partial^2\hat{\Phi}}{\partial\hat{y}^2}=\hat{c}(\hat{y})\sinh\left(\hat{\Phi}-\hat{\varphi_0}\right), \tag{2.59}$$

where we define $\lambda_0=\sqrt{\frac{\epsilon k_BT}{2e^2c_0}}$ which is the Debye length at $y=0$. Utilizing the approximation $\lambda_0^2/R^2\approx 0$, we simplify the equation to

$$\frac{\partial^2\hat{\Phi}}{\partial\hat{x}^2}=\hat{c}(\hat{y})\sinh\left(\hat{\Phi}-\hat{\varphi_0}\right), \tag{2.60}$$

which is equivalent to the one-dimensional Poisson-Boltzmann equation in dimensionless variables. Returning to dimensional variables, we reintroduce the potential difference $\Psi=\Phi-\varphi_0$, leading to the familiar form

$$\frac{\partial^2\Psi}{\partial x^2}=\frac{2ec(y)}{\epsilon}\sinh\left(\frac{e\Psi}{k_BT}\right), \tag{2.61}$$

This demonstrates that the electric double layer locally maintains its equilibrium structure. Consequently, we can calculate the potential $\Psi(x, y)$ by considering only its x-dependence. As shown in Section 2.2.3, the above equation can be integrated once to obtain

$$\frac{\partial \Psi}{\partial x} = -\sqrt{\frac{8 k_B T c(y)}{\epsilon}} \sinh\left(\frac{e\Psi}{2k_B T}\right). \tag{2.62}$$

We now proceed to solve the creeping flow equation in the electric double layer. The Coulomb force density, $\rho_e \boldsymbol{E}$, can be computed from the potential as

$$\rho_e \boldsymbol{E} = -2ec(y)\sinh\left(\frac{e\Psi}{k_B T}\right)\boldsymbol{E} = +2ec(y)\sinh\left(\frac{e\Psi}{k_B T}\right)\left(\frac{\partial \Psi}{\partial x}\boldsymbol{e_x} + \frac{\partial \Psi}{\partial y}\boldsymbol{e_y}\right). \tag{2.63}$$

We calculate the pressure by considering the normal component of the creeping flow equation:

$$0 = -\frac{\partial P}{\partial x} + 2ec(y)\sinh\left(\frac{e\Psi}{k_B T}\right)\frac{\partial \Psi}{\partial x}, \tag{2.64}$$

where we assume no fluid flow in the x-direction towards the plane, i.e., $v_x = 0$.
The pressure inside the electric double layer, as integrated in Section 2.2.4, is given by

$$P(x, y) = P_0 + 4k_B T c(y)\sinh^2\left(\frac{e\Psi(x, y)}{2k_B T}\right). \tag{2.65}$$

Next, we insert this expression for the pressure and the y-component of the Coulomb force into the y-component of the creeping flow equation:

$$0 = \eta\frac{\partial^2 v_y}{\partial x^2} - \frac{\partial P}{\partial y} + 2ec(y)\sinh\left(\frac{e\Psi}{k_B T}\right)\frac{\partial \Psi}{\partial y}. \tag{2.66}$$

The term $\frac{\partial^2 v_y}{\partial y^2}$ is set to zero, as the incompressibility condition yields $\frac{\partial v_x}{\partial x} + \frac{\partial v_y}{\partial y} = \frac{\partial v_y}{\partial y} = 0$ for $v_x = 0$.
Computing the derivative of P and acknowledging that both $c(y)$ and $\Psi(x, y)$ depend on y leaves us with

$$\eta\frac{\partial^2 v_y}{\partial x^2} = 4k_B T\sinh^2\left(\frac{e\Psi}{2k_B T}\right)\frac{\partial c(y)}{\partial y}. \tag{2.67}$$

To solve for the flow velocity v_y, we need to integrate the above expression twice with respect to x:

$$\eta\int_0^x\int_\infty^x \frac{\partial^2 v_y}{\partial x^2}dxdx = 4k_B T\frac{\partial c(y)}{\partial y}\int_0^x\int_\infty^x \sinh^2\left(\frac{e\Psi}{2k_B T}\right)dxdx. \tag{2.68}$$

Substituting $\Psi(x)$ allows us to integrate with respect to Ψ. We find $dx = -d\Psi / \left(\sqrt{\frac{8k_B T c(y)}{\epsilon}} \sinh\left(\frac{e\Psi}{2k_B T}\right) \right)$ by using equation 2.62. The integration limits are set to apply the boundary conditions for Ψ, which are $\Psi(\infty) = 0$ and $\Psi(0) = \zeta$, and for v_y, where $\left.\frac{\partial v_y}{\partial x}\right|_{x=0} = 0$. With this, the flow profile can be derived as

$$v_y = \frac{4\epsilon}{\eta} \left(\frac{k_B T}{e}\right)^2 \ln\left(\frac{\cosh\left(\frac{e\Psi}{4k_B T}\right)}{\cosh\left(\frac{e\zeta}{4k_B T}\right)}\right) \frac{\partial \ln\left(c(y)\right)}{\partial y}. \tag{2.69}$$

Far from the charged plane, where $\Psi(\infty) = 0$, the velocity approaches the value v_∞, given by:

$$v_\infty = -\frac{4\epsilon}{\eta} \left(\frac{k_B T}{e}\right)^2 \ln\left(\cosh\left(\frac{e\zeta}{4k_B T}\right)\right) \frac{\partial \ln\left(c(y)\right)}{\partial y}. \tag{2.70}$$

This equation should be interpreted as an effective boundary condition for the creeping flow equation on a macroscopic scale. Unlike electroosmosis, where the flow is driven by a constant electric field E_0 resulting in a constant flow velocity $v_\infty = \frac{-\epsilon\zeta}{\eta} E_0$ far from the plane, diffusioosmosis presents a different scenario. In diffusioosmosis, the flow velocity varies along the surface with $\frac{\partial \ln(c(y))}{\partial y}$. This implies that a constant flow field is not a valid solution outside the double layer. Moreover, the induced flow field will also alter the concentration gradient due to convection.

2.5.3 Diffusion-Induced Electric Fields

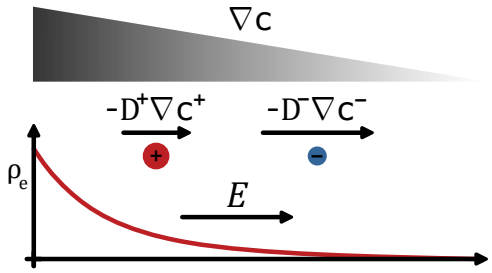

Figure 2.7. Schematic illustration of a diffusion-induced electric field. A gradient, depicted with differing gray values, of two ion species with differing diffusion constants results in differential diffusive fluxes $-D^+ \nabla c^+$ and $-D^- \nabla c^-$. In the depicted case, anions diffuse faster, leaving the cations behind. This leads to the charge distribution ρ_e shown below, which in turn gives rise to the electric field E.

In this section, we discuss the electric field that arises in an electrolyte gradient with asymmetric diffusion constants. This electric field causes an additional superimposed electroosmotic flow on top of the diffusioosmotic flow. The existence of such an electric field was initially described by Planck over a century ago [47]. Consider the concentration

gradient depicted in Figure 2.7, consisting of anions and cations with different diffusion constants, D^- and D^+, respectively. Both ion species exhibit a diffusive flux, $-D^+\boldsymbol{\nabla}c^+$ and $-D^-\boldsymbol{\nabla}c^-$, directed downward along the gradient. If anions, for instance, have higher diffusion coefficients than cations, they will diffuse down the concentration gradient more rapidly, leaving the cations behind. This results in a charge separation, as depicted in the Figure, with more positive charges on the left and negative charges on the right. The resulting charge distribution, ρ_e, gives rise to an electric field that opposes the differential diffusion. In this scenario, the electric field will move anions down the gradient and cations up the gradient. This opposing electric field results in an apparent effective diffusion constant, denoted as D^*, for both ion species combined.

To derive an expression for the electric field, we consider a macroscopic scale where we can use the electroneutrality approximation given by $0 = c^+ - c^-$, as motivated in Section 2.4.2. Using the definition $c = c^+ = c^-$, we express the ion flux equations as

$$\boldsymbol{j}^+ = -D^+\boldsymbol{\nabla}c + \frac{e}{k_BT}D^+c\boldsymbol{E} + c\boldsymbol{v}, \tag{2.71}$$

$$\boldsymbol{j}^- = -D^-\boldsymbol{\nabla}c - \frac{e}{k_BT}D^-c\boldsymbol{E} + c\boldsymbol{v}. \tag{2.72}$$

In the absence of an externally applied electric field, we can assume that the electric current is zero everywhere. Mathematically, this is expressed as $\boldsymbol{j_e} = e(\boldsymbol{j}^+ - \boldsymbol{j}^-)$. Using the expressions for the ion fluxes, one arrives at

$$0 = \frac{\boldsymbol{j_e}}{e} = -D^+\boldsymbol{\nabla}c + D^-\boldsymbol{\nabla}c + \left(D^+\frac{e}{k_BT}c + D^-\frac{e}{k_BT}c\right)\boldsymbol{E}, \tag{2.73}$$

where the convection term, $c\boldsymbol{v}$, cancels. The above equation can be solved for the electric field, yielding

$$\boldsymbol{E} = \frac{k_BT}{e}\frac{D^+ - D^-}{D^+ + D^-}\frac{\boldsymbol{\nabla}c}{c} = \frac{k_BT}{e}\frac{D^+ - D^-}{D^+ + D^-}\boldsymbol{\nabla}\ln(c). \tag{2.74}$$

2.5.4 Diffusioosmotic Slip Boundary Condition

As previously mentioned, the diffusion-induced electric field causes an additional superimposed electroosmotic flow on top of the surface pressure-driven diffusioosmotic flow, as illustrated in Figure 2.6 and derived in Section 2.5.2. The electroosmotic flow velocity outside a double layer for a tangentially imposed electric field is given by $v_\infty = -\frac{\epsilon}{\eta}\zeta E_t$. Using the expression for the the diffusion-induced electric field and assuming that the

electrolyte gradient points locally along the surface in the y-direction, we arrive at

$$v_\infty = -\frac{\epsilon}{\eta}\frac{k_B T}{e}\frac{D^+ - D^-}{D^+ + D^-}\zeta\frac{\partial \ln\left(c(y)\right)}{\partial y}. \tag{2.75}$$

We can now superimpose the electric component with the surface pressure-induced component to obtain an effective boundary condition for the creeping flow equation on a macroscopic scale. The tangential component of the flow velocity v_t is given by

$$v_t = -\frac{\epsilon}{\eta}\frac{k_B T}{e}\left(\frac{D^+ - D^-}{D^+ + D^-}\zeta + 4\frac{k_B T}{e}\ln\left(\cosh\left(\frac{e\zeta}{4k_B T}\right)\right)\right)\frac{\partial \ln\left(c(y)\right)}{\partial y}. \tag{2.76}$$

This expression is commonly referred to as the Dukhin-Derjaguin slip boundary conditions [18,19,32,40,43]. Note that the second, pressure-driven term in the equation drives liquid motion from high to low salt concentrations, since the term $\ln(\cosh(e\zeta/4k_bT))$ is positive, independent of ζ. The first term, in contrast, depends on both the sign of the zeta potential ζ and the factor $\beta = (D^+ - D^-)/(D^+ + D^-)$. This means that the direction of the electric part of the diffusioosmotic-induced fluid motion depends on the sign of the surface charge and the diffusion constants of the electrolyte used. Therefore, it is generally not trivial to predict the direction of a diffusioosmotic flow.

2.6 Diffusiophoresis

Similar to electrophoresis, where we calculated the migration velocity from the electroosmotic slip boundary condition, one can calculate the migration velocity of a particle placed in a concentration gradient using the diffusioosmotic slip boundary condition [18,19,40,43]. Consider the scenario depicted in Figure 2.8 where a spherical particle is immersed in a concentration gradient. The particle disturbs the external concentration gradient, depicted by different grey levels. It blocks the diffusive ion flux, which needs to pass around the particle. The concentration gradient on the surface of the particle will induce a diffusioosmotic flow on the particle surface, resulting in the propulsion of the particle.

2.6.1 Ion Concentration Evolution Equation

We start by deriving an evolution equation for the ion concentration on a macroscopic scale. We can eliminate the electric field in one of the ion-flux equations from Section 2.5.3 using the expression in Equation 2.74. Choosing the ion flux equation for the positive ions

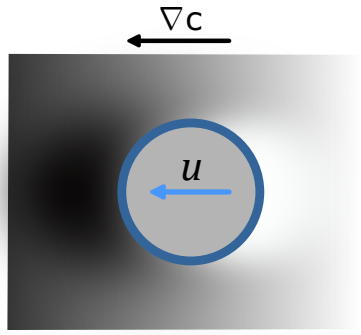

Figure 2.8. Charged sphere placed in a concentration gradient ∇c. The sphere blocks the diffusive current, resulting in the concentration distribution indicated by varying shades of gray. The diffusioosmotic flow arising on the particle surface causes its migration with velocity u.

yields

$$\boldsymbol{j}^+ = -D^+\nabla c + \frac{e}{k_B T} D^+ c \frac{k_B T}{e} \frac{D^+ - D^-}{D^+ + D^-} \frac{\nabla c}{c} + c\boldsymbol{v}, \tag{2.77}$$

which can be simplified to

$$\boldsymbol{j}^+ = \left(-D^+ + D^+ \frac{D^+ - D^-}{D^+ + D^-} \right) \nabla c + c\boldsymbol{v} = -\frac{2D^+D^-}{D^+ + D^-} \nabla c + c\boldsymbol{v}. \tag{2.78}$$

We further apply the conservation law $\nabla \cdot \boldsymbol{j}^+ + \frac{\partial c}{\partial t}$ of the positive ions to obtain the evolution equation of the ion concentration as

$$\frac{\partial c}{\partial t} = \frac{2D^+D^-}{D^+ + D^-} \Delta c + \nabla \cdot (c\boldsymbol{v}). \tag{2.79}$$

The prefactor $\frac{2D^+D^-}{D^+ + D^-}$ is the harmonic mean of the diffusion constants and serves as an effective diffusion constant D^*.

2.6.2 Diffusiophoretic Migration Velocity

To derive the migration velocity, we use a linearization of the governing equations as outlined in reference [19]. We consider three different scales: the observer scale, where the concentration varies according to equation 2.79; the particle scale, where the external concentration changes only slowly; and the scale of the electric double layer on the particle's surface.

On the intermediate scale, we linearize the external concentration gradient via a Taylor expansion, given by $c(\boldsymbol{r}) \approx c(0) + \nabla c|_{\boldsymbol{r}=0} \cdot \boldsymbol{r}$, where the coordinate $\boldsymbol{r} = 0$ represents the particle's center. We assume that the local concentration varies according to $c(\boldsymbol{r}) \approx$

$c_0 + c_1(\boldsymbol{r})$, where $c_1(\boldsymbol{r})$ is a small perturbation. We require that the perturbation $c_1(\boldsymbol{r})$ approaches $\boldsymbol{\nabla} c|_{\boldsymbol{r}=0} \cdot \boldsymbol{r}$ at a distance far from the particle. Additionally, we orient the local coordinate system such that the external concentration gradient points in the z-direction, implying $c_1(\boldsymbol{r})$ should approach $\frac{\partial c}{\partial z}\big|\, \boldsymbol{r} = 0z$.
Now, we can incorporate our approximation for the ion concentration into the evolution equation for ion concentration:

$$\frac{\partial \left(c_0 + c_1(\boldsymbol{r})\right)}{\partial t} = \frac{2D^+D^-}{D^+ + D^-} \Delta \left(c_0 + c_1(\boldsymbol{r})\right) + \boldsymbol{\nabla} \left(\left(c_0 + c_1(\boldsymbol{r})\right) \boldsymbol{v_1}\right), \tag{2.80}$$

We also assumed that the flow velocity is small and can be approximated as $\boldsymbol{v} \approx 0 + \boldsymbol{v_1}$, such that $c_1(\boldsymbol{r})\boldsymbol{v_1} \approx 0$. Acknowledging that derivatives of the constant c_0 vanish, we arrive at

$$\frac{\partial c_1(\boldsymbol{r})}{\partial t} = \frac{2D^+D^-}{D^+ + D^-} \Delta c_1(\boldsymbol{r}) + c_0 \boldsymbol{\nabla} \boldsymbol{v_1} + \boldsymbol{\nabla} \left(c_1(\boldsymbol{r}) \boldsymbol{v_1}\right) \approx \frac{2D^+D^-}{D^+ + D^-} \Delta c_1(\boldsymbol{r}), \tag{2.81}$$

where we used the incompressibility condition $\boldsymbol{\nabla} \cdot \boldsymbol{v_1} = 0$. We make another approximation, namely, that the ion concentration varies slowly locally in time in the vicinity of the particle, such that $\frac{\partial c_1(\boldsymbol{r})}{\partial t} \approx 0$. This leads us to a Laplace equation for c_1, given by

$$\Delta c_1(\boldsymbol{r}) = 0. \tag{2.82}$$

On the particle surface, we require that no ions can penetrate the surface, which is expressed as $\boldsymbol{j}^- \cdot \boldsymbol{e_r} = \boldsymbol{j}^+ \cdot \boldsymbol{e_r}$. This condition, under the above approximations, translates to $\boldsymbol{e_r} \cdot \boldsymbol{\nabla} c_1 = 0$.
We proceed in a similar manner as in the case of electrophoresis, discussed in 2.4.2. Utilizing spherical coordinates, the far-field condition for the concentration becomes $\frac{\partial c}{\partial z}\big|_{r=0} \cos(\theta)$, which we denote as $c' \cos(\theta)$. The solution that satisfies the boundary conditions of the above equation represents a dipole potential combined with the far-field condition and is given by

$$c_1 = \frac{1}{2} c' \frac{R^3}{r^2} \cos(\theta) + c' r \cos(\theta). \tag{2.83}$$

The corresponding concentration gradient is given by

$$\boldsymbol{\nabla} c_1 = -c' \cos(\theta) \left(1 - \frac{R^3}{r^3}\right) \boldsymbol{e_r} + c' \sin(\theta) \left(\frac{R^3}{2r^3} + 1\right) \boldsymbol{e_\theta}. \tag{2.84}$$

The tangential component of the concentration gradient at $r = R$ is $\boldsymbol{\nabla}_{||} c_1 = \boldsymbol{e_\theta} \cdot \boldsymbol{\nabla} c_1 = 1.5 \sin(\theta) c'$.

Next, we solve the creeping flow equation. We consider the effective boundary condition derived in Section 2.5.4 for the tangential fluid velocity, which had the form $v_t = -\mu_D(\zeta)\frac{\partial \ln(c(y))}{\partial y}$, where $\mu_D(\zeta)$ is the prefactor from equation 2.76. $\frac{\partial \ln(c(y))}{\partial y}$ represents the tangential component of the logarithmic concentration gradient at the surface. In the three-dimensional scenario of this Section, this is expressed in spherical coordinates as

$$v_t = -\mu_D(\zeta)\boldsymbol{\nabla}_{||} \ln(c). \tag{2.85}$$

Note that the prefactor $\mu_D(\zeta)$ depends on the local ion concentration through ζ.
Inserting $c \approx c_0 + c_1$ into the boundary condition and expanding for small c_1 gives

$$\left(-\mu_D(\zeta_0) - \left.\frac{\partial \mu_D}{\partial \zeta}\frac{\partial \zeta}{\partial c}\right|_{c=c_0} c_1\right) \boldsymbol{\nabla}_{||} \left(\ln(c_0) + \frac{c_1}{c_0}\right), \tag{2.86}$$

where ζ_0 is the zeta potential calculated from the ion concentration c_0, which is the ion concentration on the largest scale, the observer scale, at the particle's position. Using $\boldsymbol{\nabla}||(\ln(c_0)) = 0$ and assuming that the term containing the factor $c_1 \cdot c_1$ is approximately zero, we arrive at

$$v_t = -\mu_D(\zeta_0)\frac{\boldsymbol{\nabla}_{||} c_1}{c_0}. \tag{2.87}$$

This boundary condition for the creeping flow equation is similar to that in Section 2.4 where we discussed electrophoresis. It turns out that a valid solution of the creeping flow equation that satisfies this boundary condition is given by $\boldsymbol{v} = -\frac{\mu_D(\zeta_0)}{c_0}\boldsymbol{\nabla} c_1$, as can be shown using the same arguments given in Section 2.4.4. Since $\boldsymbol{\nabla} c_1$ approaches $c'\boldsymbol{e_z} = \left.\frac{\partial c}{\partial z}\right|_{r=0}\boldsymbol{e_z}$ far away from the particle, we conclude that $\boldsymbol{v}$ approaches $\boldsymbol{v_\infty} = -\mu_D(\zeta_0)\frac{c'}{c_0}\boldsymbol{e_z} = -\mu_D(\zeta_0)\frac{1}{c_0}\left.\frac{\partial c}{\partial z}\right|_{r=0}\boldsymbol{e_z}$, which approximates $-\mu_D(\zeta_0)\boldsymbol{\nabla}\ln(c)$ since $\boldsymbol{\nabla}\ln\left(c_0 + \left.\frac{\partial c}{\partial z}\right|_{r=0} z\right) = \frac{1}{c_0}\left.\frac{\partial c}{\partial z}\right|_{r=0}\boldsymbol{e_z}$. We can change the frame of reference again and express the migration velocity of the sphere as

$$u = \mu_D(\zeta^*)\boldsymbol{\nabla}\ln(c) = \frac{\epsilon}{\eta}\frac{k_B T}{e}\left(\frac{D^+ - D^-}{D^+ + D^-}\zeta^* + 4\frac{k_B T}{e}\ln\left(\cosh\left(\frac{e\zeta^*}{4k_B T}\right)\right)\right)\boldsymbol{\nabla}\ln(c) \tag{2.88}$$

where ζ^* refers to the zeta potential calculated with respect to the ion concentration c at the observer scale. Note that the mobility $\mu_D(\zeta^*)$ is not constant as it depends on the local ion concentration through ζ^*, which changes due to the particle's migration and the potential evolution of the external concentration profile. This means that the magnitude and direction of the migration velocity might change depending on the local ion concentration. [19]
Note that from here on, we would need to establish a force balance of the particle to

confirm that the migration velocity is correct. This is illustrated in reference [46]. Unlike electrophoresis, for diffusiophoresis, the local force balance on the particle surface is not zero, indicating that there is internal stress in the particle during migration [46].

3. Emergence of Colloidal Patterns in ac Electric Fields

The text and figures in this chapter are adapted from the publication [35] stated below and have been restructured to better suit this thesis. The videos mentioned below are accessible on the publisher's webpage and are referenced accordingly.

Emergence of Colloidal Patterns in ac Electric Fields

Florian Katzmeier, Bernhard Altaner, Jonathan List, Ulrich Gerland, and Friedrich C. Simmel,
Physics Department E14 and T37, TU Munich, D-85748 Garching, Germany

In this chapter, my coauthors and I provide a comprehensive explanation of a colloidal pattern formation phenomena, which was independently rediscovered by several researchers [48–50], including myself, for various types of particles. It was observed that when an alternating electric field is applied to sedimented particles in a microscopy chamber, the particles organize into extended dynamic band patterns perpendicular to the electric field (see upper two panels in Figure 3.1).

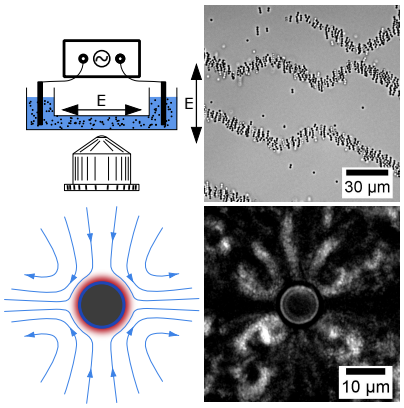

Figure 3.1. Overview Figure: Emergence of Colloidal Patterns in AC Electric Fields. (Upper left) Experimental setup. (Upper right) Late stage of the colloidal patterning phenomena. (Lower left) Electrically induced quadrupole flow responsible for the patterning. (Lower right) Experimentally observed quadrupole flow.

Motivated by the rediscoveries across different particle types, I experimentally confirmed the generic nature of this phenomenon by observing patterning for a range of different

particle types. Since existing literature lacked a thorough explanation, I conducted an extensive literature review on recently described nonlinear electrokinetic phenomena. This review led me to conclude that a typical flow, specifically a quadrupole flow arising around spherical particles in an AC electric field [30,31,33,36,51], could account for the observed patterning phenomena (see lower two panels in Figure 3.1). To validate my assessment, I implemented a many-particle Brownian dynamics simulation, taking special care to incorporate hydrodynamic interactions resulting from the quadrupole flow. This simulation successfully reproduced all stages of the patterning process. Notably, the quadrupole flow can be explicitly observed around larger particles by examining the trajectories of smaller particles (see lower right panel in Figure 3.1).

To gain further insight, I conducted experiments with silica particles, focusing on the frequency and ion concentration dependence of the patterning phenomena. In collaboration with Bernhard Altaner, I confirmed that the patterning phenomena can be quantitatively predicted without any free parameters, by utilizing the weakly nonlinear multi-scale theory of Schnitzer, Yariv, et al. [32,33].

3.1 Introduction

Systems driven far from equilibrium can self-organize into spatiotemporal dissipative structures and thereby undergo spontaneous symmetry breaking [52, 53]. Such dynamic behavior has been observed in electrokinetic experiments with clay particles [50], polystyrene micro-spheres [49], and also with λ-DNA [48]. When an alternating electric field is applied, particles form chains along the field direction, which move towards each other, align in parallel and develop extended band patterns roughly perpendicular to the field direction. The particle chains within the bands undergo dynamic break-up, resulting in the formation of triangular band structures wherein the particles circulate.

Originally, Jennings attributed the chain break-up to dipole like repulsion forces arising from electrophoretic particle oscillations [50]. Hu et al. explained the particle circulation with electrorotation caused by mutual polarization of the particles [49]. Further experimental studies following this interpretation were conducted by Lele et al. [54] and Mittal et al. [55]. For observations with λ-DNA, Isambert and coworkers assumed that hydrodynamic interactions were generated by local conductivity gradients caused by electrophoretic salt depletion [48], resulting in liquid shearing under the influence of an external electric field. All of these models explained the dynamics within the band structures, but did not address their formation in the first place.

In the present work we verify the generic emergence of the same characteristic patterns for a wide range of colloidal particles. We demonstrate that the observed phenomena can be naturally explained with an electrokinetic fluid flow [30, 33, 51] around the particles. A Brownian particle simulation accounting for the hydrodynamic and dipole-dipole pair interactions reproduces the key aspects of the band pattern formation, such as spontaneous symmetry breaking, inclination of the bands, and particle circulation within these bands. For silica spheres, we experimentally investigate the emergence of patterns as a function of salt concentration and AC field frequency. The observed dependence can be predicted without any free parameters from the weakly nonlinear multi-scale theory of Schnitzer, Yariv, et al. [32, 33].

3.2 Results

3.2.1 Experiments

We conducted our experiments with aqueous suspensions of various micrometer-scale particles, including fluorocarbon (FC) oil and lauric acid droplets, coacervates made from

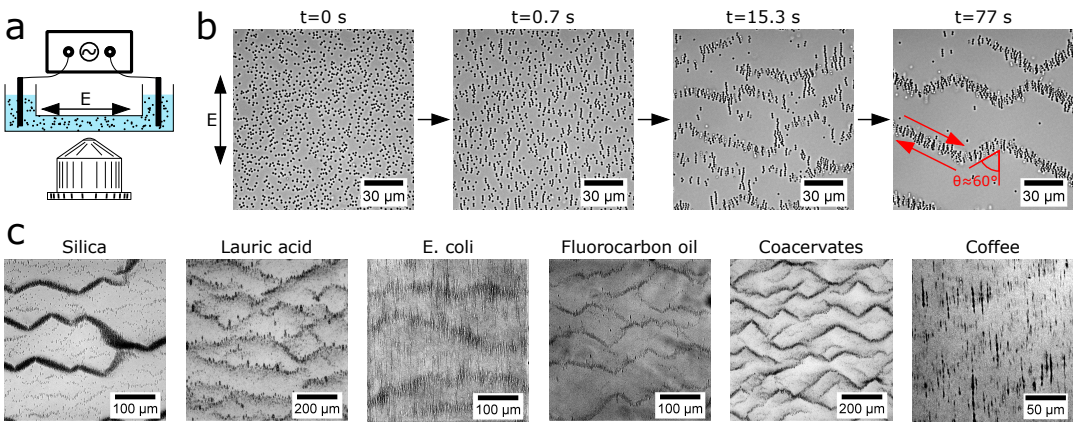

Figure 3.2. (a) Schematic representation of the experimental setup. Aqueous particle suspensions are subjected to AC electrical fields inside of a microscopic observation chamber. (b) Snapshots of a suspension of $1.3\,\mu$m diameter silica particles in an AC electric field ($E_0 = 17\,\mathrm{mV/\mu m}$, $f = 500\,\mathrm{Hz}$) at different timepoints. The formation of zigzag-shaped band patterns is clearly visible. In the fully formed bands ($t = 77\,\mathrm{s}$) the particles circulate as indicated. (c) Band formation and zigzag patterns in suspensions of various colloids. The images are taken $\approx 100\,\mathrm{s}$ after the electric field was turned on.

poly(allylamine) and adenosine triphosphate (ATP), monodisperse silica particles (radius $a \approx 650\,\mathrm{nm}$), *E. coli* bacteria, and ground coffee (Experimental details and particle size distributions are given in sections 3.4.1 and 3.6.5, respectively). The suspensions were loaded into microscope observation chambers with platinum electrodes placed at opposite inlets (see Figure 3.2a). After letting the colloids sediment for $10\,\mathrm{min}$, we applied an in-plane AC electric field and recorded the resulting dynamics on the bottom of the chamber with an inverted microscope. We applied electric fields with amplitudes between $17\,\mathrm{mV/\mu m}$ and $56\,\mathrm{mV/\mu m}$, which is on the order of the thermal voltage ($\varphi_{\mathrm{th}} := k_{\mathrm{B}}T/\mathrm{e} \approx 25.69\,\mathrm{mV}$) for µm sized particles. The applied frequency was set to $500\,\mathrm{Hz}$ for all samples except for bacteria, where it was $250\,\mathrm{Hz}$.

We found that similar band patterns formed in all our samples (Figure 3.2). Particle chain formation occurred within the first second after the electric field was switched on, while horizontal band structures emerged within the first minute. The band structures continued to grow and merge until the electric field was switched off. The time course of the pattern formation process is exemplary shown for silica particles in Figure. 3.2b, and can be clearly observed in the supplementary videos [35]. Snapshots of the patterns taken $100\,\mathrm{s}$ after the electric field was turned on are shown in Figure. 3.2(c). We observed distinct zigzag patterns for coacervates, FC oil and silica particles, and less dominant patterns for the polydisperse lauric acid droplets. For the bacteria we found only chain formation at $f = 500\,\mathrm{Hz}$, while at $f = 250\,\mathrm{Hz}$ the typical band patterns emerged, but

less pronounced zigzag structures. The sample containing the polydisperse ground coffee particles showed more irregular behavior, but chain formation and also the onset of band formation could be clearly observed. The angle between the zigzag bands and the electric field axis was roughly $60°$ (highlighted in Figure 3.2b).

3.2.2 Theoretical Background

The initially observed formation of particle chains is well-known [49,50,54,55] and is caused by induced dipole-dipole interactions. When the external AC electric field is described as the real part of the complex phasor $\boldsymbol{E}(t) = E_0 e^{\mathrm{i}\omega t}\hat{\mathbf{e}}_z$ with angular frequency $\omega = 2\pi f$, the time-averaged dipole-dipole force on a particle at position $\boldsymbol{r}$ exerted by another residing at the coordinate origin is given as

$$\boldsymbol{F}^{\mathrm{dip}}(\boldsymbol{r}) = 6\pi\epsilon|K_{\mathrm{d}}|^2 E_0^2 a^2 \boldsymbol{h}(\boldsymbol{r})\,, \tag{3.1}$$

with the complex dipole coefficient K_{d}, the permittivity of water ϵ and the substitution $\boldsymbol{h}(\boldsymbol{r}) := \frac{1-3\cos^2\theta}{r^4}\hat{\mathbf{e}}_r - \frac{2\cos\theta\sin\theta}{r^4}\hat{\mathbf{e}}_\theta$ (θ is the zenith angle in spherical coordinates, and r is given in units of the particle radius a).

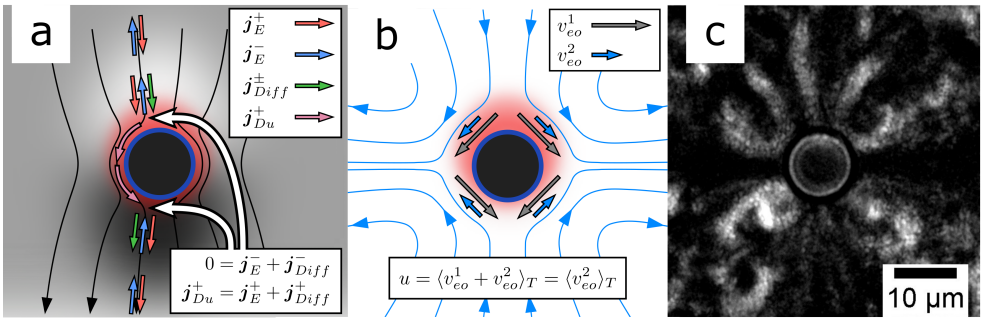

Figure 3.3. (a) A charged particle in an electric field (black field lines) surrounded by counterions (red cloud) with ion fluxes (outlined arrows) along one field line. The neutral salt concentration is drawn as a grey cloud (darker regions correspond to higher concentrations). (b) Time averaged electrokinetic flow arising from Coulomb forces acting on the Debye layer. (c) Experimentally observed fluid motion around a large coacervate (superposition of a $3.8\,\mathrm{s}$ long video with enhanced contrast for moving particles). Bright areas correspond to trajectories of smaller coacervates.

The formation of large scale patterns is driven by hydrodynamic interactions, which are caused by electrokinetic flow around the particles. The corresponding Poisson–Nernst–Planck–Navier–Stokes system of nonlinear partial differential equations can only be solved approximately [10, 12–14, 16, 37, 38, 42, 56–60]. For the DC case, Schnitzer, Yariv, et

al. [32, 33] recently developed a weakly non-linear electrokinetic theory, in which the dimensionless electrokinetic flow $\tilde{\boldsymbol{u}} := \boldsymbol{u}/u^*$, with $u^* = \frac{(k_\mathrm{B}T)^2\epsilon}{\mathrm{e}^2 a\eta}$, is expanded in powers of the dimensionless electric field $\xi = \frac{\mathrm{e}a}{k_\mathrm{B}T}E_0$:

$$\tilde{\boldsymbol{u}} = \xi\tilde{\boldsymbol{u}}_1 + \xi^2\tilde{\boldsymbol{u}}_2 + \xi^3\tilde{\boldsymbol{u}}_3 + \dots. \tag{3.2}$$

From the DC solution one can extrapolate to the time-averaged AC solution, where one can use the fact that odd powers of $\xi \propto E_0 e^{\mathrm{i}\omega t}$ have a zero time average, which leaves $\tilde{\boldsymbol{u}}_2$ as the leading order electrokinetic flow (for an AC solution in a special case, see also reference [36]). An explicit expression for $\tilde{\boldsymbol{u}}_2$ can be deduced from the stream function given in [33], which results in

$$\boldsymbol{u} = \frac{1}{2}u^*\xi^2\tilde{\boldsymbol{u}}_2 = u^*\xi^2\frac{\gamma}{2}\left(\boldsymbol{g} - \boldsymbol{h}\right) \tag{3.3}$$

where $\boldsymbol{g}(\boldsymbol{r}) := \frac{1-3\cos^2\theta}{r^2}\hat{\mathbf{e}}_r$ is a radial field and γ is a dimensionless microscopic parameter (see below and reference [33]). Notably, this well-known flow pattern [30, 51] can be explicitly observed around large coacervate droplets via the trajectories of smaller droplets (see Figure 3.3c and supplementary videos [35]), which follow the streamlines of the electrokinetic flow shown in Figure 3.3b.

The derivation of the individual terms in equation 3.2 is quite involved [32, 33], but the mechanism can be understood qualitatively from the scheme in Figure 3.3: a negatively charged particle immersed in an electrolyte is surrounded by a diffuse charge layer (Debye layer), in which positive counter-ions are accumulated and co-ions are almost completely depleted. Outside the Debye layer the salt solution is electrically neutral. The asymmetry in ionic concentrations results in an ion-selective surface conductivity and surface current j^+_{Du}, which is characterized by the ion-selective Dukhin number Du [32].

In the electro-neutral region, the electric field drives Ohmic counter- and co-ionic currents $\boldsymbol{j}^+_E$ and $\boldsymbol{j}^-_E$ parallel to the field lines. Along field lines entering the Debye layer, flux balance requires a diffusion flux $\boldsymbol{j}_{\mathsf{diff}}$ which counterbalances the co-ion current $\boldsymbol{j}^-_E$. $\boldsymbol{j}_{\mathsf{diff}}$ can only result from a variation of the neutral salt concentration n in the vicinity of the colloid, which in Figure 3.3a is depicted as a grey cloud with varying intensity. The electrokinetic properties of the Debye layer are determined by the zeta potential ζ, which depends on the surface charge and the extension of the Debye layer κ^{-1}, which in turn depends on n via $\kappa^{-1} = (2\mathrm{e}^2 n/\epsilon k_\mathrm{B}T)^{1/2}$. The variation of n outside the Debye layer causes a locally varying perturbation ζ_1 of the equilibrium zeta potential ζ_0 i.e., $\zeta = \zeta_0 + \zeta_1$, visualized as an expansion of the Debye layer on one side and a compression on the other side of the

particle.

The free charges in the Debye layer are subject to a Coulomb force due to the tangential component of the electric field E_θ, which gives rise to fluid motion according to the electrokinetic slip boundary condition $v_{eo} = \zeta E_\theta$. The first and second order velocity components $v_{eo}^{(1)}$ and $v_{eo}^{(2)}$ connected to ζ_0 and ζ_1 are indicated in Figure 3.3b. For alternating electric fields $v_{eo}^{(1)}$ has a zero time average, while $v_{eo}^{(2)}$ has a non-vanishing time average, resulting in a fluid flow around the particle.

3.2.3 Brownian Dynamics Simulation

In the overdamped limit, a direct force $\boldsymbol{F}_i^{\text{tot}}$ exerted on particle i results in particle drift with velocity $\frac{D_p}{k_\text{B}T}\boldsymbol{F}_i^{\text{tot}}$ where D_p is thediffusion constant of the particle.To include hydrodynamic interactions with the flow field $\boldsymbol{u}_i^{\text{tot}}(\boldsymbol{r})$, which is caused by other particles ($j \neq i$) in the fluid, we use Faxen's correction for the drift velocity:

$$\boldsymbol{v}_i = \frac{D_p}{k_\text{B}T}\boldsymbol{F}_i^{\text{tot}} + \left(1 + \frac{1}{6}\Delta\right)\boldsymbol{u}_i^{\text{tot}}. \tag{3.4}$$

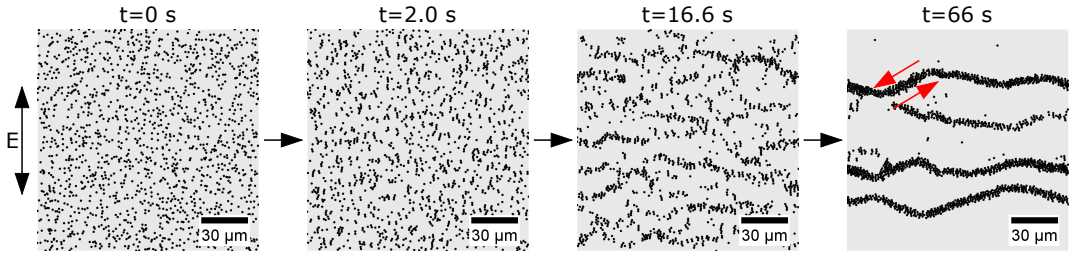

Figure 3.4. Simulated dynamics with $\gamma = 0.088$ and $|K_\text{d}|^2 = 0.23$. Snapshots of a large scale simulation of the patterning process. The different stages of the experimentally observed patterning process from Figure 3.2b are nicely reproduced. The particles circulate again as indicated.

The direct force on particle i is obtained as the sum of dipolar and a repulsive interactions $\boldsymbol{F}^{\text{rep}}(\boldsymbol{r}_{ij})$ i.e. $\boldsymbol{F}_i^{\text{tot}} = \sum_{j\neq i}\left(\boldsymbol{F}^{\text{dip}}(\boldsymbol{r}_{ij}) + \boldsymbol{F}^{\text{rep}}(\boldsymbol{r}_{ij})\right)$, where $\boldsymbol{r}_{ij} = \boldsymbol{r}_i - \boldsymbol{r}_j$ denotes the difference vector between particles i and j. Ignoring geometric interactions, the velocity field caused by the particles $j \neq i$ is to zeroth order given as the sum $\boldsymbol{u}_i^{\text{tot}} = \sum_{j\neq i}\boldsymbol{u}(\boldsymbol{r}_{ij})$. Together with 3.1 and 3.3 and by recognizing that $\Delta\boldsymbol{g} = -6\boldsymbol{h}$ and $\Delta\boldsymbol{h} = 0$, the drift velocity (Equation 3.4) becomes

$$\boldsymbol{v}_i(\boldsymbol{r}_i) = u^* \sum_{j\neq i}\left[\xi^2\left(\frac{\gamma}{2}\boldsymbol{g}(\boldsymbol{r}_{ij}) + (|K_\text{d}|^2 - \gamma)\boldsymbol{h}(\boldsymbol{r}_{ij})\right) + \nu\boldsymbol{k}(\boldsymbol{r}_{ij})\right] \tag{3.5}$$

where the repulsion $\nu \boldsymbol{k}(\boldsymbol{r}_{ij})$ is discussed in Section 3.6 The movement of the particles can then be described by the N-particle Langevin equation,

$$a\,\mathrm{d}\boldsymbol{r}_i = \boldsymbol{v}_i\,\mathrm{d}t + \sqrt{2D_p}\,\mathrm{d}W_i\,, \tag{3.6}$$

where $\mathrm{d}W$ is the increment of a Wiener process.
We numerically solved this stochastic differential equation with periodic boundary conditions and random initial particle configurations (see Section 3.6.1). As we observed the emergence of stripe patterns exclusively at the channel bottom, we restricted our simulation to two dimensions by constraining the dipole-dipole force and fluid flow to the plane $y = 0$, which captures both geometry and scaling of the physical interactions qualitatively correctly. As shown in Figure 3.4, a simulation based on equation 3.6 with 1521 particles, $\gamma = 0.088$, $|K_\mathrm{d}|^2 = 0.23$, and a particle number density matched to our silica particle experiments recapitulates all stages of the observed pattern formation process (cf. Figure 3.2 and supporting videos [35]; see Section 3.7.2 for a simulation with polydisperse particles.)

3.2.4 Parameter Dependence

To gain further insight into the physical mechanisms underlying the pattern formation process, we explored its dependence on AC field frequency and salt concentration. We prepared aqueous suspensions of silica particles at 0.0375 % (w/v) with NaCl concentrations ranging from $5\,\mu\mathrm{M}$ to $2500\,\mu\mathrm{M}$, and recorded microscopy videos with a relatively weak electric field amplitude of $10.6\,\mathrm{mV\,\mu m^{-1}}$ at frequencies ranging from $250\,\mathrm{Hz}$ to $25\,\mathrm{kHz}$. To analyze our data, we defined the 'pattern visibility' p in an image as the discretized version of $p = \int_A |\frac{\partial}{\partial z}\,(G * I)\,(x,z)|dxdz$ where A is the area of the image, G is a Gaussian with a standard deviation of 15 pixels (corresponding to $6\,\mu\mathrm{m}$), $I(x,z)$ is the image intensity, and $*$ denotes convolution. The order parameter $p(t)$ is time-dependent and measures density fluctuations along the z-direction at a scale defined by G. We computed $p(t)$ for every frame of our microscopy videos and used it to determine a typical timescale τ_p for the emergence of stripe patterns (examples of $p(t)$ are shown in Section 3.5.1). In Figure 3.5), τ_p^{-1} is plotted as a measure for the speed of pattern formation for various frequencies and salt concentrations.
As electrokinetic fluid flow appears to drive the pattern formation process, we expect τ_p^{-1} to scale with the magnitude of the fluid flow, which is set by γ. The microscopic parameter γ is related to the physics of the Debye layer, whose details are specified by the curvature parameter $\delta := (\kappa a)^{-1}$ and the dimensionless equilibrium zeta potential

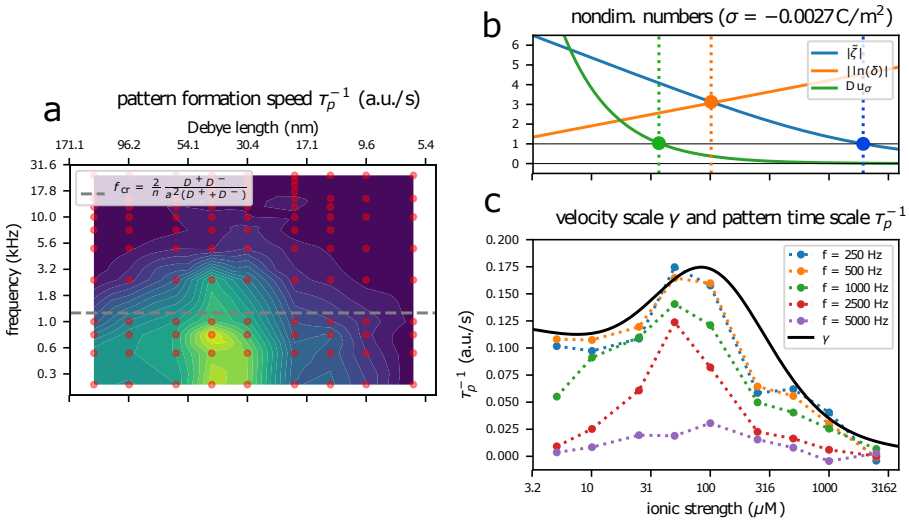

Figure 3.5. (a) Observed pattern visibility p in an experiment. Red circles indicate the experimental data points with a heat map generated by linear interpolation on the logarithmic grid. (b) Dimensionless characteristic numbers for electrokinetics lead to characteristic scales for the ionic strength (or, equivalently, Debye length). (c) The low-frequency pattern visibility p can be quantitatively predicted without fit parameters using the second-order velocity scale γ derived by Schnitzer and Yariv in Ref. [33].

$\widetilde{\zeta_0} = \zeta_0/\varphi_{\mathrm{th}}$ [32, 33]. The latter is linked to the dimensionless surface charge density $\widetilde{\sigma} := \frac{\sigma}{\epsilon\kappa\varphi_{\mathrm{th}}}$ by the Grahame equation $\widetilde{\sigma} = 2\sinh\widetilde{\zeta_0}/2$. The ionic transport around colloidal particles is characterized by the Dukhin number Du, which measures the relative strength of surface to bulk conductivity [39, 61, 62]. By considering the surface conductivity of counter-ions only, an ion-selective Dukhin number [32, 33] given by $\mathrm{Du}_\sigma := \delta\widetilde{\sigma}(1+2\mu^+)$ can be defined with the ionic drag coefficient $\mu^+ := \frac{\epsilon\varphi_{\mathrm{th}}^2}{\eta D^+}$ and the counter-ion diffusion constant D^+ [32, 33].

In Figure 3.5b, we show the variation of these dimensionless numbers for the ionic conditions of our experiment, where we set the surface charge to the known value for silica particles $\sigma = -0.0027\,\mathrm{C/m^2}$ [63]. Comparison with Figure 3.5a indicates that patterns can be observed only up to a characteristic ionic strength where $\left|\widetilde{\zeta_0}\right|$ (blue dot) is $O(1)$. For higher ionic strengths, $|\zeta_0| < \varphi_{\mathrm{th}}$, the physics of the Debye layer can be neglected altogether. Further, pattern formation is fastest when the zeta potential is 'logarithmically large' compared to the curvature parameter i.e. $\left|\widetilde{\zeta}\right| = O(|\ln(\delta)|)$ (orange dot) and where surface conduction becomes dominant over bulk conduction i.e. $\mathrm{Du}_\sigma = O(1)$ (green dot). Finally, in Figure 3.5c we compare γ (Reference [33]) with the observed pattern visibility p, for which we scaled p such that its maximum at $f = 250\,\mathrm{Hz}$ corresponds to the maximum value of γ. For the lowest experimental frequencies, we find excellent agreement between pattern visibility p and γ, and even for higher frequencies p qualitatively shows the same

behavior, albeit with a reduced amplitude. Notably, the appearance of patterns for salt concentrations below $1\,\mathrm{mM}$ as well as the maximum pattern formation speed at around $50\,\mu\mathrm{M}$ are nicely predicted by γ, when $\sigma = -0.0027\,\mathrm{C/m^2}$ is used. Further, we find that the value of γ chosen for our simulation (Figure 3.4) has a physically reasonable magnitude. While no nonlinear AC theory is available to date, we find that the decrease of the amplitude falls in the range of the characteristic frequency $f_{\mathrm{cr}} = \frac{2}{\pi}\frac{D^+D^-}{a^2(D^+ + D^-)} = 1.2\,\mathrm{kHz}$ of the variation of neutral salt n, which is known from other linear AC theories [24, 38, 60, 64–66]. As also expected from this model, both f_{cr} and τ_p^{-1} are reduced in experiments with higher viscosity (cf. Section 3.7.1).

It remains to be explained why similar patterns emerge for widely different particle types even though the model predicting the hydrodynamic flow strictly applies only for hard spheres with a surface charge - except for the silica particles, the shape and interfacial structure of the investigated colloids is generally more complex (see also Section 3.7.3). First, the geometry of the hydrodynamic flow is somewhat expected as it is the second order term of the general axisymmetric solution of the overdamped Navier-Stokes equation outside of a sphere [33] [67] [68]. Further, we expect the underlying mechanism to be generic to surface charge-stabilized colloidal dispersions [69], for which accumulation of counter-ions and depletion of co-ions close to the colloidal surface gives rise to an ion-selective surface conduction even for more complex surface compositions. Qualitatively, patterns are thus generally expected at low ionic strengths($< 1\,\mathrm{mM}$) and low frequencies($f < 1.2\,\mathrm{kHz}$) as predicted by the hard sphere model, and as used in the experiments of Figure 3.2.

3.3 Conclusion

In conclusion, we experimentally verified the generic occurrence of a pattern formation process that had been previously observed when different types of colloids in aqueous suspension were subjected to AC electrical fields. We identified the physical mechanisms underlying the pattern forming process as dipole-dipole interactions and second order electrokinetic fluid flow, and confirmed the emergence of collective behavior in a many particle simulation. We found that Schnitzer-Yariv's weakly non-linear electrokinetic theory gives a parameter-free quantitative explanation of the pattern formation process, which only requires a surface charge on the colloidal particles, providing a satisfactory unifying explanation for the observed macroscopic patterns and their underlying physical mechanism.

Apart from its fundamental scientific interest, the described effect could be utilized for

applications in microfluidics and microrobotics. For instance, it should be possible to use the described electrokinetic flow to realize microfluidic pumps and mixers, as previously proposed based on induced charge electroosmosis [70–75]. Further, our insights should be helpful for the development of electrically manipulated microswimmers, which were previously envisioned [31] and implemented [76–81] based on inorganic (metallo-dielectric) Janus particles. Our experimental results with oil droplets, coacervates, lauric acid and even bacteria demonstrate that similar swimmers consisting solely of soft and biological material are feasible.

3.4 Materials and Methods

3.4.1 Preparation of Colloidal Suspensions

In initial experiments, we found that the formation of patterns predominantly occurs at low salt concentrations ($250\,\mu$M NaCl). We therefore usually included several washing steps in the preparation of our colloidal sample. Distilled and deionized water (ddH_2O) with a resistivity ρ of $18.2\,\mathrm{M}\Omega/\mathrm{cm}$ was obtained from a water purification system (Sartorius arium® pro).

Silica Microspheres

Monodisperse silica particles with a diameter of $1.3\,\mu$m in 5 % (w/v) aqueous suspension were purchased from the microParticles GmbH (LOT:SiO_2-F-L1272). Before usage, we vortexed the stock solution and mixed $100\,\mu$L of the stock solution with $900\,\mu$L ddH_2O in an Eppendorf tube. The sample was centrifuged in a table centrifuge for $30\,$s until the colloids sedimented completely. The excess washing liquid ($900\,\mu$L) was then carefully removed again. The washing steps were repeated 5 times. The washed stock solution was then used as a starting solution for all further experiments with silica particles.

For the experiment shown in Figure 3.2 we created a solution with a particle density of 0.0375 % (w/v) and a NaCl concentration of $250\,\mu$M. A particle density of 0.0375 % (w/v) nominally corresponds to 176 210 particles per mm^3, where we used a density of $1.85\,\mathrm{g/cm}^3$ [82] for silica. In order to generate more distinct macroscopic patterns, for the experiment shown in Figure 3.2c we created a suspension with a higher particle density of 0.1 %(w/v) in a $250\,\mu$M NaCl solution.

Polyallylamine-ATP Coacervates

Polyallylamine with an average molecular weight of $17\,\mathrm{kDa}$ was obtained as an aqueous solution with a concentration of 20 % (w/w) (Sigma Aldrich 479136-1G, Lot # MKCL0467). We diluted the polyallylamine solution to a monomer concentration of $20\,\mathrm{mM}$ and adjusted the pH to 7. Adenosine 5'-triphosphate (ATP) dipotassium salt (Sigma Aldrich A8937-1G, Lot # SLBP7423V) was used to create a $100\,\mathrm{mM}$ stock solution in ddH_2O, which we aliquoted and froze at $-20\,^{\circ}\mathrm{C}$.

The conditions for the formation of stable polyallylamine-ATP coacervate droplets were derived from [83]. To create the coacervates we pipetted $20\,\mu\mathrm{L}$ of the ATP stock into $1000\,\mu\mathrm{L}$ of the polyallylamine stock solution which was kept at $4\,^{\circ}\mathrm{C}$ and vortexed the solution briefly. We then centrifuged the sample at 10000 rcf and $4\,^{\circ}\mathrm{C}$ for $1\,\mathrm{min}$. We then removed the supernatant and resuspended the coacervates in $1\,\mathrm{mL}$ ddH_2O. After a second washing step the coacervates were resuspended in $500\,\mu\mathrm{L}$ of a $250\,\mu\mathrm{M}$ NaCl solution.

Molten Lauric Acid Droplets

$0.5\,\mathrm{mg}$ lauric acid (Sigma Aldrich, # W261408-SAMPLE-K) was added to $10\,\mathrm{mL}$ of a $250\,\mu\mathrm{M}$ NaCl solution in a $15\,\mathrm{mL}$ Falcon tube. The Falcon tube was placed in a water bath placed on a heat plate, which had been set to $150\,^{\circ}\mathrm{C}$ for $30\,\mathrm{min}$. When the lauric acid was dissolved, we vortexed the Falcon tube for $1\,\mathrm{min}$ and diluted $100\,\mu\mathrm{L}$ of the resulting lauric acid emulsion in $900\,\mu\mathrm{L}$ of a pre-heated $250\,\mu\mathrm{M}$ NaCl solution in an Eppendorf tube. The sample was vortexed again for $1\,\mathrm{min}$ and a $100\,\mu\mathrm{L}$ aliquot was diluted once more in $900\,\mu\mathrm{L}$ of a pre-heated NaCl solution. We then sonicated the sample for $1\,\mathrm{min}$ using an ultrasonic homogenizer (Bandelin Sonopuls mini20) equipped with an MS 2.5 sonotrode at maximum settings ($20\,\mathrm{W}$). The sonotrode was moved in circles around the liquid air interface near the wall of the tube (this was done as we found that the colloids tended to accumulate at that part of the tube during sonication). After preparation, the sample was stored in the heat bath.

Fluorocarbon Oil Droplets

$2\,\mu\mathrm{L}$ fluorocarbon oil (Sigma Aldrich, # F9755) containing 2% of a surfactant (FluoSurf from Emulseo, Bordeaux) was added to $998\,\mu\mathrm{L}$ of a $250\,\mu\mathrm{M}$ NaCl solution. We sonicated the sample for 1 min at maximum power ($20\,\mathrm{W}$). As for the lauric acid droplets, the sonotrode was moved in circles around the liquid air interface near the wall of the tube.

E.coli Bacteria

Bacteria (E.coli DH5α) were grown for $16\,$h at $36\,^{\circ}$C in $5\,$mL of LB medium (Carl Roth, # X968.1) in a shaking incubator. The bacteria were diluted 1 to 100 in two tubes each containing $5\,$mL of fresh LB medium and grown until an OD_{600} of 2.1 was reached. The tubes containing the bacteria were put on ice for $15\,\mathrm{min}$ to cool them down to $4\,^{\circ}$C, followed by centrifugation at 3000 rcf and $4\,^{\circ}$C for $15\,\mathrm{min}$. The supernatant was removed and the bacterial pellets were re-suspended each in $5\,$mL of $4\,^{\circ}$C cold ddH_2O. After two further washing steps the bacteria were eluted in $1\,$mL of a $250\,$µM NaCl solution and pooled.

Coffee

Coffee was brewed in the office with a filter coffee machine using 2 spoons of ground coffee (Dallmayr Prodomo, 100% ARABICA) and 2 coffee filters (Rewe, Ja!). The coffee was filled into a $0.2\,$L cup, which was placed on an office desk and covered with a piece of carton. After letting the coffee particles sediment for $24\,$h, we recovered the cold coffee suspension from the office desk. To this end, we removed two times $5\,$mL of the coffee suspension from the surface of the cup and put them in two $15\,$mL Falcon tubes. We then followed the same washing protocol used for the bacteria. We sonicated the final coffee samples for 1 min at maximum settings ($20\,$W) to remove any remaining larger coffee particles.

3.4.2 Microscopy Experiments

AC signals of up to $20\,$V peak to peak were generated with a function generator RIGOL DG812 and were amplified with a home-built two channel, bipolar amplifier to voltages in the range $[-290\,\mathrm{V} : 290\,\mathrm{V}]$. Each amplifier channel employs a pair of high voltage operational amplifiers (Apex PA443) connected in a bridge amplifier configuration with a gain adjusted to 36 ($31.1\,$dB). Due to the employed operational amplifier and circuit configuration, the maximum slew rate is limited to $64\,\mathrm{V/\mu s}$. Detailed schematics and circuit board layouts can be provided by the authors upon request.

We conducted our experiments in self-made glass chambers or in commercial plastic chambers (Ibidi, μ-Slide VI 0.4), depending on the physical nature of our colloids. The self-made glass chambers are an adaption of the design used by Kopperger and List. [84] Details can be provided by the authors upon request. For imaging, we used an inverted

microscope (Olympus IX71) equipped with a CCD camera (Andor Luca, DL-604M). Self-made glass chambers enabled us the apply larger electric fields due to their shorter channel length, which we found to be necessary to trigger the formation of patterns for coffee particles, E.coli and fluorocarbon oil. On the other hand, we avoided to measure lauric acid and silica micro spheres in glass chambers as they tended to stick to the glass surface. As the pattern occurred on a scale of around $200\,\mu m$ we mostly used a magnification (20x) where our microscopy images have a size of $400\,\mu m$ x $400\,\mu m$. The size of the commercial plastic chambers was $3.7\,\mu m$ x $17\,\mu m$ and the size of the self made glass chambers was $4\,mm$ x $4\,mm$. The size of the observation chamber is chosen such that it is much larger as the occurring pattern during the recording time. We further imaged all our samples in the middle of the observation chamber. We therewith reduce the influence of confinement effects. The specific experimental conditions are listed in Table 3.1. In all experiments, we used sample volumes of $100\,\mu L$ of the colloidal suspensions described above. For the experiment with lauric acid we used a temperature controlled microscopy stage (Tokai Hit OLYMPUS THERMO PLATE, #MATS-UAXKP-D) which was heated to $50\,^{\circ}C$. The nominal exposure time was set to 50 ms in our experiments. The actual time between frames was saved in the metadata file and was $\approx 100\,ms$. The scale bar in all microscopy images and the time stamp in the supplementary videos was inserted with ImageJ.

Table 3.1. Experimental settings for imaging the different colloids

Colloid	Channel	Channel length (mm)	Voltage amplitude (V)	Electric field amplitude (mV/µm)	Frequency (Hz)	Objective
Silica (Figure 3.2b)	Ibidi	17	288	17	500	40x
Silica (Figure 3.2c)	Ibidi	17	288	17	500	20x
Coacervates	Ibidi	17	288	17	500	10x
Lauric acid	Ibidi	17	288	17	500	10x
Fluocarbon oil	Glass	5	180	36	500	20x
Coffee	Glass	5	288	58	500	20x
E. coli	Glass	5	288	58	250	20x

Bacteria

In contrast to the experiments with the other colloids, for E.coli bacteria we found only vertical chain formation at an electric field frequency of $500\,Hz$. By contrast, the usual horizontal band structures were found at a lower frequency of $250\,Hz$. We attribute this finding to the presumably more complex electric properties of the bacteria. Two images of a bacterial suspension at the two frequencies are shown in Figure 3.6.

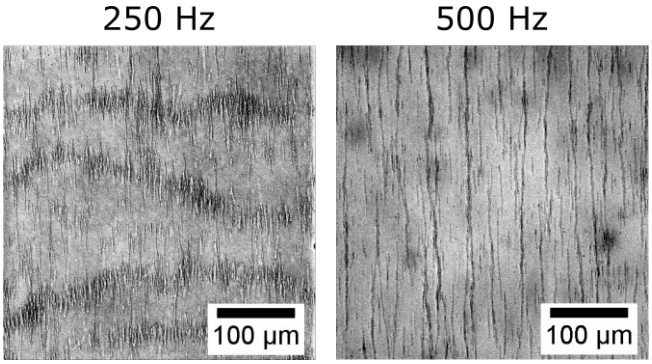

Figure 3.6. Both images are taken $100\,\mathrm{s}$ after the electric field was turned on. The other conditions are the same as listed in Table 3.1. The electric field oscillates as usual along the vertical axis.

Imaging of the Hydrodynamic Flow in Figure 3.3

In experiments with polydisperse particle suspensions we found that the hydrodynamic flow can be explicitly observed around larger particles based on the trajectory of the smaller particles surrounding them. To image the hydrodynamic flow we conducted an experiment with coacervates in a glass chamber where we applied an electric field amplitude of $36\,\mathrm{mV/\mu m}$ and a frequency of $500\,\mathrm{Hz}$. Our coacervates were best suited for this experiment, as the corresponding samples usually contained a small number of larger particles. We recorded a video focused on a large coacervate with a 100x magnification. We corrected for the drift of the large coacervate with an ImageJ plugin (Template Matching and Slice Alignment from Qingzong Tseng [85]). To create the image in Figure 3.3c we cut out a 50×50 µm^2 region of the drift corrected video and computed the absolute difference of subsequent images of the stack, which lets moving particles appear as bright spots with high contrast. From this we computed the average of 30 successive video frames that had sufficient image quality. Particle trajectories appear as bright stripes in the averaged image.

3.5 Parameter Screening

We explored the dependence of the emergence of patterns on AC field frequency and salt concentration to gain deeper insight into the underlying mechanism.

3.5.1 Experiment

For the experiment we prepared a washed silica particle stock solution as described in Section 3.4.1, from which we generated suspensions at 0.0375 % (w/v) with NaCl con-

centrations ranging from $0\,\mu M$ to $2500\,\mu M$. As the solution conductivity is a critical parameter of our experiment we prepared our experiments with particular care to avoid any salt contamination. Hence, before usage we washed every tube with ddH_2O, and we multiply pipetted ddH_2O with every fresh pipette tip before pipetting a sample. We flushed the commercial microscopy channels with ddH_2O before filling them with a sample. We found that any contact of a sample with unwashed surfaces resulted in an increase in conductivity. We applied a relatively weak electric field with amplitude $10.6\,mV/\mu m$ and applied frequencies ranging from $250\,Hz$ to $25\,kHz$. Between successive runs at a fixed frequency, an electric field of $1.06\,mV/\mu m$ at $1\,Hz$ was applied for $2\,min$ to mix the sample, followed by a pause of three minutes before the next run at a different frequency. We recorded microscopy videos with 2000 frames each and an exposure time of $50\,ms/frame$ for every sample at a given frequency and salt concentration. The actual time interval between frames was around $100\,ms$ and varied slightly from run to run. The actual time interval was saved in the microscopy metadata file and used later for the data analysis.

To confirm the absence of contaminants in a freshly prepared sample, we measured the conductivity of our samples at the lowest frequency ($250\,Hz$) and compared it to the theoretically expected conductivity at a given salt concentration. To this end, we put a reference resistor R_{ref} in series with our sample and monitored the voltage across the resistor $A(t)$ and the voltage supply $B(t)$ with a digital oscilloscope (picoscope 2206B). We recorded $\langle|A(t)|\rangle_T$, $\langle|B(t)|\rangle_T$ and $\langle A(t)\cdot B(t)\rangle_T$. From this measurement, the conductivity of the sample can be determined as follows:

The fraction of the voltage across the reference resistor that is in phase with the applied voltage is given by $\frac{\langle A(t)\cdot B(t)\rangle_T}{\langle|B(t)|\rangle_T}$ and the corresponding in-phase current is $\frac{\langle A(t)\cdot B(t)\rangle_T}{R_{\mathrm{ref}}\langle|B(t)|\rangle_T}$. From the latter we can compute the resistance of the sample via $\frac{1}{R_{\mathrm{sample}}} = \frac{\langle A(t)\cdot B(t)\rangle_T}{R_{\mathrm{ref}}(\langle|B(t)|\rangle_T)^2}$ where we assumed that the resistance of the sample is much larger than that of the reference resistor. The electrolytic conductivity can be computed from R_{sample} and the channel geometry via $\frac{1}{\rho} = \frac{1}{R_{\mathrm{sample}}}\frac{L}{W\cdot H}$ where $17\,mm$, $3.8\,mm$ and $0.4\,mm$. The measured data and the corresponding values for the in-phase current and electrolytic conductivity are listed in Table 3.2.

We fitted a line to the measured conductivity values to obtain the limiting conductivity Λ. (Figure 3.7). We found $\Lambda = 0.121\,(S/cm)/M$ which is in good agreement with the theoretical value for the limiting conductivity of $0.125\,(S/cm)/M$ computed from the Nernst-Einstein equation (using $D_{Na^+} = 1.3\times10^{-9}m^2/s$ and $D_{Cl^-} = 2\times10^{-9}m^2/s$).

[NaCl] (µM)	$\langle \lvert A(t) \rvert \rangle_T$ (mV)	$\langle \lvert B(t) \rvert \rangle_T$ (V)	$\langle \lvert A(t)B(t) \rvert \rangle_T$ $(V \cdot V)$	R_{ref} Ω	In phase current (µA)	$\frac{1}{\rho}$ (µS/cm)
Air	6.85	125.9	0.007	11000	0.0051	0.0045
0	8.467	125.9	0.98	11000	0.71	0.63
5	20.01	126	2.47	11000	1.78	1.58
10	26.68	125.9	3.331	11000	2.41	2.14
25	50.63	125.8	6.362	11000	4.60	4.09
50	96.26	125.9	12.11	11000	8.74	7.77
100	171.8	126	21.64	11000	15.61	13.86
250	396	126	50.08	11000	36.13	32.07
500	841	125.9	105.9	11000	76.47	67.93
1000	171.6	125.9	21.72	1100	156.83	139.32
2500	357	125.9	45.89	1100	331.36	294.36

Table 3.2. Measurements of the electrolytic conductivity $\frac{1}{\rho}$ of the microscopy samples used for the screening experiment.

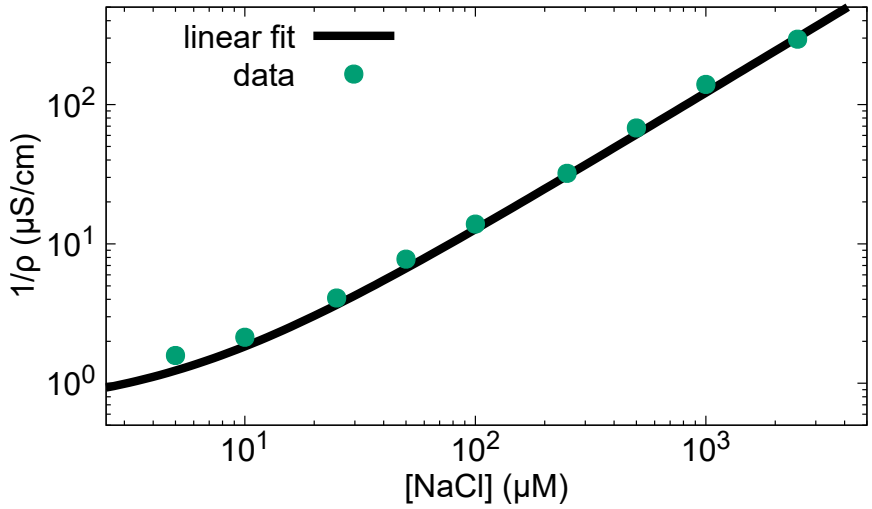

Figure 3.7. Plot of the electrolytic conductivity $\frac{1}{\rho}$ from Table 3.2 fitted to a linear function.

Data Analysis

We defined the 'pattern visibility' p in an image as a measure for large scale structure occurring along the direction of the electric field, i.e., in z-direction. The approach is motivated by scale-space theory [86]. Figure 3.8 illustrates the definition of the 'pattern visibility' p in a microscopy image at three different stages of the pattern formation process. Below the images we plotted the image intensity of a cross section. For the original images on the left dips correspond to single particles. To obtain p we first apply a Gaussian filter with a standard deviation of 15 pixels (corresponding to $6\,\mu$m at our magnification) to an image. This eliminates the information of individual particles. Images of a pattern will have large scale density fluctuations in z-direction while images with no pattern will appear mostly homogeneous. This can be seen in the cross section below the middle images. The density fluctuations can be quantified by computing the integral of the absolute value of the derivative of the image in z-direction. In the cross section plots, this operation amounts to computing the length of the intensity graph. The absolute value of the derivative of the image in z-direction is shown on the right. The area below

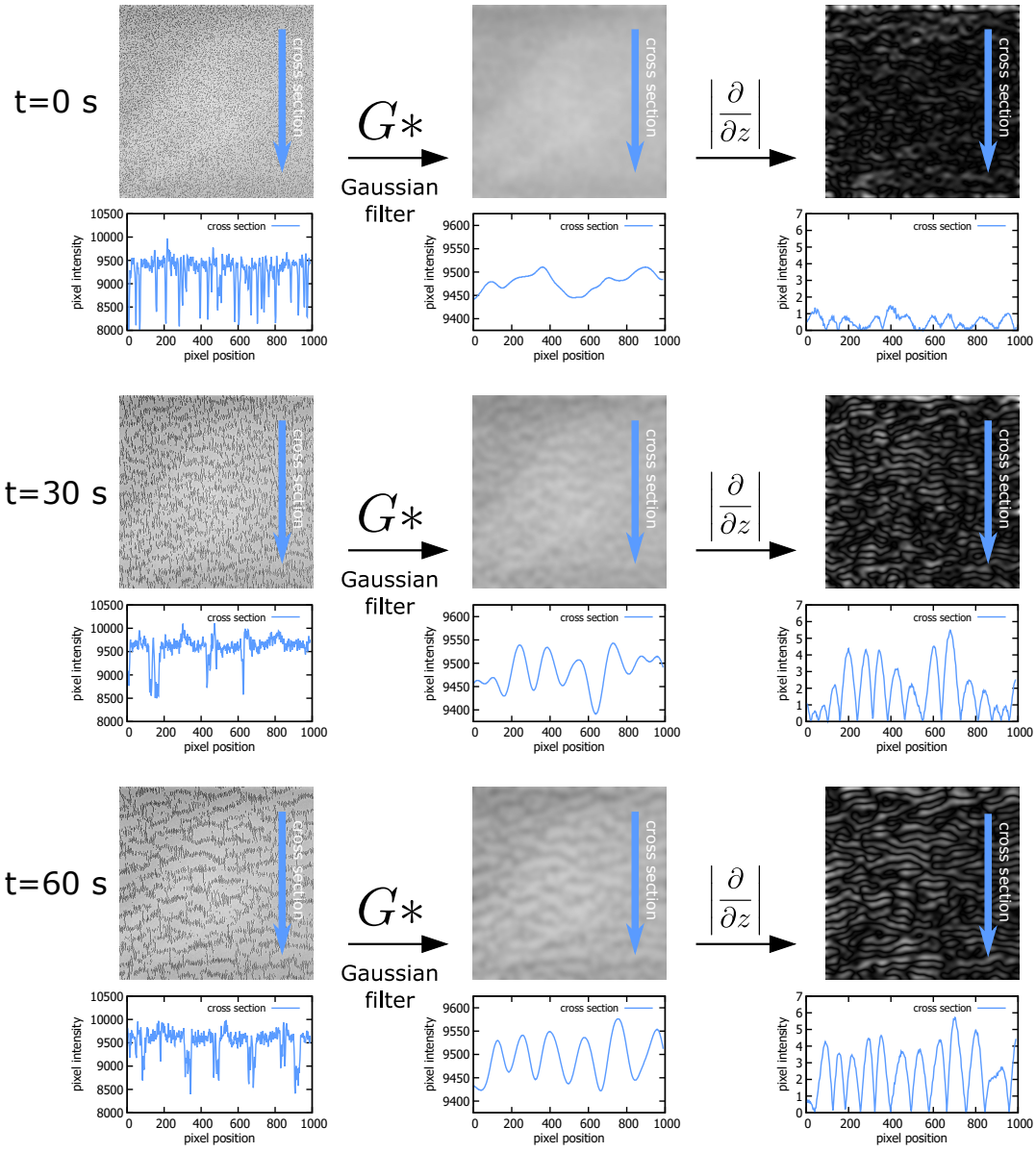

Figure 3.8. Illustration of the definition of the 'pattern visibility' p at different stages of the patterning process. The image intensity of the marked cross sections is plotted in the graph below the images.

the graphs in the corresponding cross section plots is the 'pattern visibility' of the cross section. The pattern visibility p of the whole image can be obtained by summing over all possible cross sections.

In practice, we compute a discretized version of

$$p = \int_A \left| \frac{\partial}{\partial z} \left(G * I \right) (x, z) \right| dxdz \tag{3.7}$$

where g is a Gaussian function and I is the intensity of the image ($*$ indicates convolution). We computed p for every frame of the videos of our screening experiment. We then computed the speed of the patterning process τ_p^{-1} by fitting lines to the initial stage of the p vs time data. Examples of the p vs time data including the linear fit are shown in Figure 3.9.

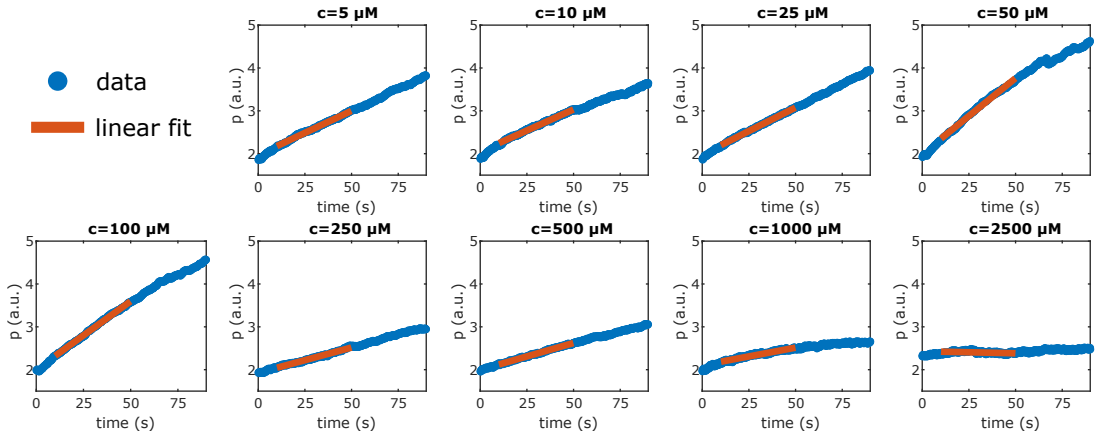

Figure 3.9. Example plots of the p vs time data for $250\,\mathrm{Hz}$ measurements. The linear fit to obtain the initial speed τ_p^{-1} of the patterning process is also included.

We analyzed our microscopy videos with ImageJ scripts. To compute the derivative of an image we used the FeatureJ plugin.

We would finally like to discuss the limitations of our definition of the pattern visibility p. p is, in principle, only a property of an image and is thus a function of the microscope settings used for imaging. In all our experiments we kept the microscope settings constant. However, high contrast images make p more sensitive for pattern quantification. Further, the smallest size of a pattern that can be quantified is set by the standard deviation of the Gaussian filter that is applied in the first analysis step.

3.6 Theory and Simulation

The SDE governing the particle dynamics in explicit form is given by

$$a\,\mathrm{d}\boldsymbol{q}_i = u^* \sum_{j\neq i} \left[\xi^2 \left(\frac{\gamma}{2}\boldsymbol{g}(\boldsymbol{r}_{ij}) + (|K_\mathrm{d}|^2 - \gamma)\boldsymbol{h}(\boldsymbol{r}_{ij}) \right) + \nu \boldsymbol{k}(\boldsymbol{r}_{ij}) \right] \mathrm{d}t + \sqrt{2D_p}\,\mathrm{d}W_i\,. \quad (3.8)$$

where the particle distances $\boldsymbol{r}_{ij}$ are defined by $\boldsymbol{r}_{ij} = \boldsymbol{q}_i - \boldsymbol{q}_j$ and $\mathrm{d}W_i$ is the stochastistic increment of a Wiener process. The positions of the particle centers $\boldsymbol{q}_i$ are given in dimensionless variables (in multiples of the particle radius). For the purpose of our simulation

we re-scaled time by $\frac{a^2}{D^p}$ and introduced the new dimensionless numbers

$$\alpha = \frac{\gamma}{2}\frac{a}{D_p}\xi^2 u^* = \frac{\gamma}{2}\frac{6\pi\epsilon E_0^2 a^3}{k_B T} \tag{3.9}$$

$$\beta = \left(\left|K_{\mathsf{d}}^2\right| - \gamma\right)\frac{a}{D_p}\xi^2 u^* = \left(\left|K_{\mathsf{d}}^2\right| - \gamma\right)\frac{6\pi\epsilon E_0^2 a^3}{k_B T} \tag{3.10}$$

and

$$\widetilde{\nu} = \nu\frac{a}{D^p}u^\star. \tag{3.11}$$

With these variables, the SDE is given by

$$\mathrm{d}\boldsymbol{q}_i = \sum_{j\neq i}\left[\alpha\boldsymbol{g}(\boldsymbol{r}_{ij}) + \beta\boldsymbol{h}(\boldsymbol{r}_{ij}) + \widetilde{\nu}\boldsymbol{k}(\boldsymbol{r}_{ij})\right]\mathrm{d}t + \sqrt{2}\,\mathrm{d}W_i\,. \tag{3.12}$$

The repulsion force $\boldsymbol{k}(\boldsymbol{r}_{ij})$ is included for particles in contact with each other. Particles are in contact when they are closer than two times the particle radius a. In dimensionless variables this condition is met when $|\boldsymbol{r}_{ij}| = |\boldsymbol{q}_i - \boldsymbol{q}_j| < 2$. The dipole-dipole-force and the hydrodynamic interactions are only defined outside the particles. We therefore assume that these interactions do not increase any further for intersecting particles. We halt $\boldsymbol{h}$ and $\boldsymbol{g}$ at their value at the particle surface and thereby obtain continuous vector fields. The explicit expressions for the particle interactions used in the simulation are given by

$$\boldsymbol{g}(\boldsymbol{r}) = \begin{cases} \frac{(1-3\cos^2(\theta)}{r^2}\hat{\mathbf{e}}_r & \text{for} \quad r > 2 \\ \frac{(1-3\cos^2(\theta)}{2^2}\hat{\mathbf{e}}_r & \text{for} \quad r \leq 2 \end{cases} \tag{3.13}$$

$$\boldsymbol{h}(\boldsymbol{r}) = \begin{cases} \frac{1-3\cos^2(\theta)}{r^4}\hat{\mathbf{e}}_r - \frac{2\cos(\theta)\sin(\theta)}{r^4}\hat{\mathbf{e}}_\theta & \text{for} \quad r > 2 \\ \frac{1-3\cos^2(\theta)}{2^4}\hat{\mathbf{e}}_r - \frac{2\cos(\theta)\sin(\theta)}{2^4}\hat{\mathbf{e}}_\theta & \text{for} \quad r \leq 2 \end{cases} \tag{3.14}$$

and

$$\boldsymbol{k}(\boldsymbol{r}) = \begin{cases} 0 & \text{for} \quad r > 2 \\ \frac{1}{\sqrt{2}}\left(2-r\right)^{\frac{3}{2}}\hat{\mathbf{e}}_r & \text{for} \quad r \leq 2 \end{cases} \tag{3.15}$$

3.6.1 Simulation

We implemented the Euler-Maruyama solution scheme to solve the overdamped many particle Langevin equation numerically (Matlab code is available on Github [87]). We

explicitly compute

$$\delta \boldsymbol{q}_i^t = \sum_{j \neq i} \left[\alpha \boldsymbol{g}(\boldsymbol{r}_{ij}^t) + \beta \boldsymbol{h}(\boldsymbol{r}_{ij}^t) + \widetilde{\nu} \boldsymbol{k}(\boldsymbol{r}_{ij}^t) \right] \delta t + \sqrt{2\delta t} \boldsymbol{X_i} \tag{3.16}$$

for every time step δt where $\boldsymbol{X_i}$ is a two-component vector of normally distributed random numbers with standard deviation 1 and $\boldsymbol{r}_{ij}^t$ is defined by $\boldsymbol{r}_{ij}^t = \boldsymbol{q}_i^t - \boldsymbol{q}_j^t$. This in turn gives the updated particle positions via

$$\boldsymbol{q}_i^{t+\delta t} = \boldsymbol{q}_i^t + \delta \boldsymbol{q}_i^t \tag{3.17}$$

3.6.2 Implementation

The particles are placed on a square grid with a dimensionless distance of $d = 5.6$. We choose the grid distance in such a way that the particle density is matched with our screening simulation. This is explained in more detail in Section 3.6.4.

We begin our simulations by letting the particles diffuse freely with only the repulsion force acting between particles. For this phase, we increased the standard deviation of the random number by a factor of 10 for a more rapid randomization and let the particles diffuse for 2000 integration steps with $\delta t = 1 \times 10^{-3}$. We explicitly compute

$$\delta \boldsymbol{q}_i^t = \sum_{j \neq i} \left[\widetilde{\nu} \boldsymbol{k}(\boldsymbol{r}_{ij}^t) \right] \delta t + 10\sqrt{2\delta t} \boldsymbol{X_i}. \tag{3.18}$$

This gives a mean square displacement for a particle from the initial position of approximately 400. The parameters of this initial stage are chosen such that $\sqrt{400}$ is larger compared to the initial particle distance and therefore yields a sufficient randomization of the particle positions.

After the randomization, the particle positions are updated according to equation 3.16 and 3.17. We implemented periodic boundary conditions by surrounding the 2D simulation box with eight copies of itself. The forces acting on one particle are computed by considering all other particles including the eight copies. Particles moving out of the simulation box on one side re-enter the box from the opposite side.

3.6.3 Numerical Stability

We observed that for badly chosen simulation parameters, particles tend to diffuse into each other and are then subjected to a large repulsion force which lets them jump over unphysically large distances. We therefore determined ad hoc criteria for the repulsion

parameter $\widetilde{\nu}$ of the contact force and the time step δt to prevent this particle hopping artifact. To this end, we first consider the equilibrium position of two intersecting particles. The maximum attraction of the two vector fields $\alpha \boldsymbol{g}$ and $\beta \boldsymbol{h}$ is given at an angle $\theta = 0$ and a distance $r = 2$. We thus find $\max(-\alpha \boldsymbol{g}) = \frac{\alpha}{2}$ and $\max(-\beta \boldsymbol{h}) = \frac{\beta}{8}$. The equilibrium position of two intersecting particles at maximum attraction is therefore given by

$$r_m = 2 - \left(\frac{\sqrt{2}}{\widetilde{\nu}} \left(\frac{\beta}{8} + \frac{\alpha}{2} \right) \right)^{\frac{2}{3}} \tag{3.19}$$

For our large scale simulation we choose $\alpha = 7$, $\beta = 35$, and $\widetilde{\nu} = 400$, which gives $r_m = 1.91$, corresponding to a 4.6 % deviation from the hard sphere distance.

Particle hopping occurs when a particle diffuses far enough into another particle's core such that the resulting repulsion force displaces the particle over a large distance away from the other particle. Lets say one particle has diffused far into an other particle such that their centers have now the distance $|\boldsymbol{r}| < 2$. In the next integration step the particle will be displaced by the distance $\widetilde{\nu} \boldsymbol{k}(\boldsymbol{r}) \delta t$. We want to avoid that the particle is catapulted out of the other particle. We therefore require that the particle does not leave the other particle in one single integration step. Such an integration step is at least $|2 - r|$ long. We therefore require

$$|2 - r| > \widetilde{\nu} \frac{1}{\sqrt{2}} (2 - r)^{\frac{3}{2}} \, \delta t, \tag{3.20}$$

which gives

$$\sqrt{2 - r} > \frac{\sqrt{2}}{\widetilde{\nu} \delta t}. \tag{3.21}$$

We now require such a jump to be extremely unlikely. ($\leq 10 \; \sigma$ or $p \leq 1.5 \times 10^{-23}$):

$$10 \sqrt{2 \delta t} = |2 - r|, \tag{3.22}$$

which in combination with equation 3.21 results in a condition for the maximum time step of our simulation:

$$\delta t = \left(\frac{\sqrt{2}}{10 \widetilde{\nu}^2} \right)^{\frac{2}{5}} \tag{3.23}$$

For $\widetilde{\nu} = 400$, this conditions yields $\delta t = 4.7 \times 10^{-3}$, and we therefore choose the slightly smaller value of $\delta t = 1 \times 10^{-3}$.

3.6.4 Matching the Particle Density between Experiment and Simulation

The particles in our simulation are initially placed on a square grid with a defined distance d between particles. d is related to the 2D particle density C_A via $C_A = \frac{1}{d^2}$ or $d = \sqrt{\frac{1}{C_A}}$. We estimate C_A in our screening experiment by counting the particles in the first frame of a video. For every concentration of NaCl we randomly choose one experiment at a given frequency for counting, and count the particles in a $(100\,\mu\text{m})^2$ large part of an image. The results are shown in Table 3.3. We find an average particle number of 763 which corresponds to a dimensionless particle density of 0.0322. We used $100\,\mu\text{m} \hat{=} 153.8$ for rescaling space with the particle radius of $a = 0.65\,\mu\text{m}$. For the dimensionless particle distance we find $d = 5.6$.

From the previously computed particle density of 176 210 per mm^3 and the channel height of $0.4\,\text{mm}$ we would expect 705 particles in an area of $(100\,\mu\text{m})^2$ (this 10% deviation from the expected value presumably is the result of the particle washing procedure).

Concentration (µM)	0	5	10	25	50	100	250	500	1000	2500
Frequency (Hz)	750	750	7500	250	17500	1000	250	12500	15000	2500
Particles in $(100\,\mu\text{m})^2$	755	767	690	820	779	803	750	681	826	759

Table 3.3. Counted number density of particles in our screening experiment

3.6.5 Particle Size Distributions

We estimated the size distributions of the colloids used in Figure 3.2 via image analysis. To this end, we used the minimum cross entropy thresholding routine implemented in ImageJ [88] to create binary images from the first frame of each of the recorded microscopy videos. We then used the 'Analyze Particle' function to measure the area of detected particles. The resulting particle diameter distributions are shown in Figure 3.10. We also show images where detected particles were marked with red circles.

For quantitative analysis, we fitted the Weibull distribution

$$f(x) = bx^{k-1}e^{\left(\frac{x}{\lambda}\right)^k} \tag{3.24}$$

to our experimentally determined particle size histograms, where k is the shape parameter and λ denotes the scale parameter of the distribution. b is a measure for the total amount of particles. The vertical line in our histograms corresponds to the size of one pixel in our images, we therefore excluded the corresponding bar from the fit. The expected value μ and the standard deviation σ are derived from the fit parameters and are given in the

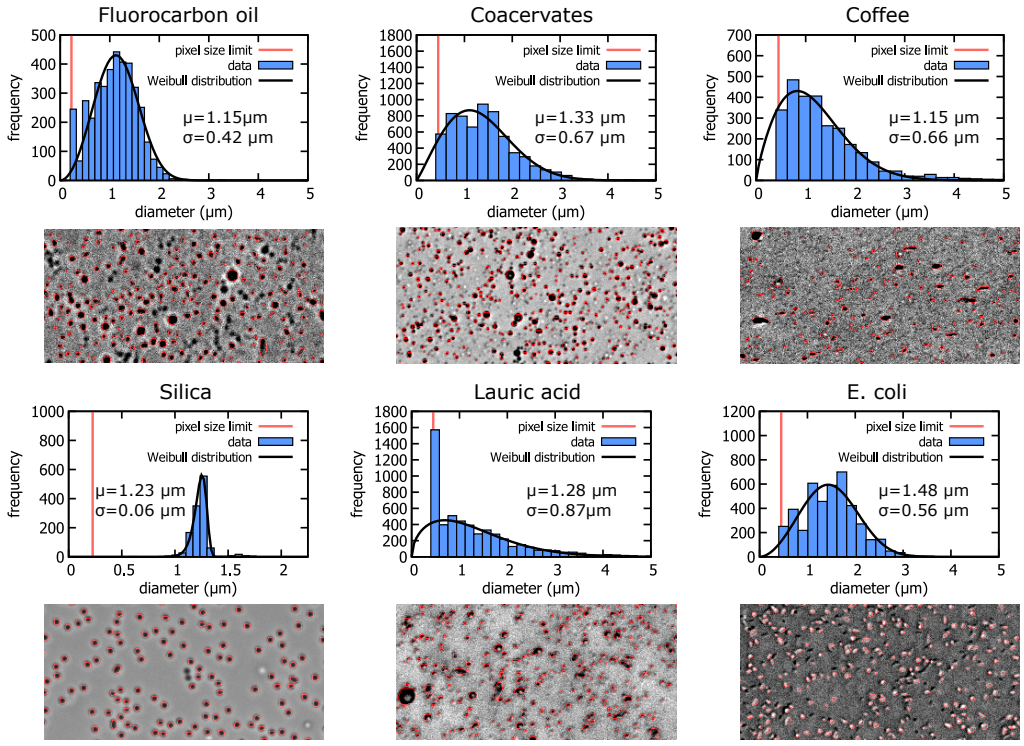

Figure 3.10. Particle size distributions of the colloids used in Figure 3.2. μ and σ are the expected value and standard deviation of the particle sizes

histograms. We find that most particles have a mean diameter of around $1.2\,\mu$m. We find that the Lauric acid droplets are very polydisperse, while among the soft colloids the FC oil droplets are the smallest and also least polydisperse. The mean diameter of the monodisperse silica particles ($\mu = 1.23\,\mu$m) is reasonably close to their expected diameter of $1.3\,\mu$m.

3.7 Supplementary Results

3.7.1 The Influence of Viscosity

The non-dimensionalized equations 3.12 together with the parameters 3.9,3.10,3.11 are independent of the medium viscosity η. Further, the parameters γ and K_d are independent of viscosity as well [33]. By contrast, the dimensional time $\tilde{t}$ is connected to dimensionless time t via the relation $\tilde{t} = \frac{a^2}{D_p} t = \frac{6\pi\eta a^3}{k_B T} t$. We therefore expect that the speed of pattern formation τ_p^{-1} decreases by a factor of $\frac{\eta_1}{\eta_0}$ when the viscosity is increased from η_0 to η_1. The characteristic frequency depends on the diffusion constants D^+ and D^- of the ions via $f_{\text{cr}} = \frac{2}{\pi} \frac{D^+ D^-}{a^2 (D^+ + D^-)}$. The Stokes-Einstein equation predicts the diffusion constant to

depend on the viscosity as $D^{\pm} \propto \frac{1}{\eta}$. We therefore expect the characteristic frequency f_{cr} should also decrease by a factor of $\frac{\eta_1}{\eta_0}$ when the viscosity increases from η_0 to η_1. We note such time scaling behavior is generally true for overdamped systems.

We designed an experiment to verify these predictions. We recorded microscopy videos of the pattern formation process at a fixed salt concentration ($100\,\mu$M) and several frequencies for two different viscosities of the aqueous medium - one sample was prepared with water, while the viscosity in the other sample was changed by adding 20% (v/v) of glycerol (Sigma Aldrich, # 49767-100ML). We kept the other conditions the same as in our other screening experiment. Using an online tool [89] based on Refs. [90] and [91], we computed the ratio $\frac{\eta_1}{\eta_0} = 1.94$ ($T = 25\,^{\circ}$C) from the glycerol concentration.

The speed of pattern formation τ_p^{-1} at different AC frequencies for the two viscosities is shown in Figure 3.11a. In agreement with our predictions we find the overall pattern formation speed to be slower for the more viscous sample as well as the frequency response shifted to lower frequencies. In 3.11b we scaled τ_p^{-1} and f_{cr} for the glycerol-containing sample with the predicted value of $\frac{\eta_1}{\eta_0}$, resulting in reasonable agreement between the two graphs.

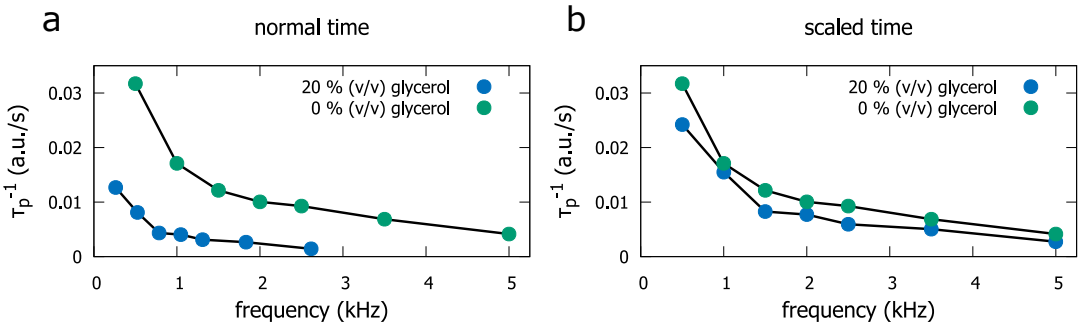

Figure 3.11. (a) Effect of glycerol on the patterning speed at different frequencies. (b) patterning speed rescaled with the viscosity ratio $\frac{\eta_1}{\eta_0}$.

3.7.2 Generalization of the Simulation for Particles with Varying Size

As the particle-particle interactions scale with the radii of the respective particles, we have to reformulate the equations underlying the simulation in an appropriate way, for which we start with the fully dimensional interaction equations. Dimensional variables are denoted by a tilde.

The drift $\tilde{\boldsymbol{v}}_{ij}^{dip}$ of a particle at position $\tilde{\boldsymbol{q}}_i$ due to the dipole-dipole force of a particle at position $\tilde{\boldsymbol{q}}_j$ is given by

$$\tilde{\boldsymbol{v}}_{ij}^{dip} = \frac{1}{6\pi\eta\tilde{R}_i} \cdot 6\pi\epsilon \left|K_d\right|^2 E_0^2 \tilde{R}_i^3 \tilde{R}_j^3 \boldsymbol{h}_{ij}(\tilde{\boldsymbol{r}}_{ij}) \tag{3.25}$$

where the factor $\frac{1}{6\pi\eta\tilde{R}_i}$ is the Stokes drag on particle i and $\tilde{\boldsymbol{r}}_{ij}$ is given by $\tilde{\boldsymbol{r}}_{ij} = \tilde{\boldsymbol{q}}_i - \tilde{\boldsymbol{q}}_j$. For particles in contact we again fix $\boldsymbol{h}_{ij}(\boldsymbol{r})$ at its value at the surface. Particles are in contact when $|\tilde{\boldsymbol{r}}_{ij}| < \tilde{R}_i + \tilde{R}_j$. We find

$$\boldsymbol{h}_{ij}(\tilde{\boldsymbol{r}}) = \begin{cases} \frac{1-3\cos^2(\theta)}{\tilde{r}^4}\hat{\mathbf{e}}_r - \frac{2\cos(\theta)\sin(\theta)}{\tilde{r}^4}\hat{\mathbf{e}}_\theta & \text{for} \quad \tilde{r} > \tilde{R}_i + \tilde{R}_j \\ \frac{1-3\cos^2(\theta)}{(\tilde{R}_i+\tilde{R}_j)^4}\hat{\mathbf{e}}_r - \frac{2\cos(\theta)\sin(\theta)}{(\tilde{R}_i+\tilde{R}_j)^4}\hat{\mathbf{e}}_\theta & \text{for} \quad \tilde{r} \leq \tilde{R}_i + \tilde{R}_j \end{cases} \tag{3.26}$$

The hydrodynamic flow at position $\tilde{\boldsymbol{q}}_i$ caused by a particle at position $\tilde{\boldsymbol{q}}_j$ is then given by

$$\tilde{\boldsymbol{u}}_j = \frac{\gamma}{2}\left(\frac{e\tilde{R}_j}{k_B T}E_0\right)^2 \frac{(k_B T)^2\epsilon}{e^2\tilde{R}_j\eta}\left(\tilde{R}_j^2 \boldsymbol{g}_{ij}(\tilde{\boldsymbol{r}}_{ij}) - \tilde{R}_j^4 \boldsymbol{h}_{ij}(\tilde{\boldsymbol{r}}_{ij})\right) \tag{3.27}$$

The corresponding drift $\tilde{\boldsymbol{u}}_{ij}$ of a particle at position $\tilde{\boldsymbol{q}}_i$ can be computed by Faxen's law $\tilde{\boldsymbol{u}}_{ij} = (1 + \tilde{R}_i^2\boldsymbol{\nabla}^2)\tilde{\boldsymbol{u}}_j$ which gives

$$\tilde{\boldsymbol{u}}_{ij} = \frac{\gamma}{2}\left(\frac{e\tilde{R}_j}{k_B T}E_0\right)^2 \frac{(k_B T)^2\epsilon}{e^2\tilde{R}_j\eta}\left(\tilde{R}_j^2 \boldsymbol{g}_{ij}(\tilde{\boldsymbol{r}}_{ij}) - \left(\tilde{R}_j^2 + \tilde{R}_i^2\right)\tilde{R}_j^2 \boldsymbol{h}_{ij}(\tilde{\boldsymbol{r}}_{ij})\right) \tag{3.28}$$

For particles in contact we also fix $\boldsymbol{g}_{ij}(\boldsymbol{r})$ at its value at the surface. We find

$$\boldsymbol{g}_{ij}(\tilde{\boldsymbol{r}}) = \begin{cases} \frac{1-3\cos^2(\theta)}{\tilde{r}^2}\hat{\mathbf{e}}_r & \text{for} \quad \tilde{r} > \tilde{R}_i + \tilde{R}_j \\ \frac{1-3\cos^2(\theta)}{(\tilde{R}_i+\tilde{R}_j)^2}\hat{\mathbf{e}}_r & \text{for} \quad \tilde{r} \leq \tilde{R}_i + \tilde{R}_j \end{cases} \tag{3.29}$$

The drift $\tilde{\boldsymbol{v}}_{ij}^{rep}$ due to the repulsion force for interacting particles is motivated by the Hertz contact mechanics model for two spheres. We assume that this results in a reasonable scaling of the repulsion force between differently sized particles. We use

$$\tilde{\boldsymbol{v}}_{ij}^{rep} = \frac{1}{6\pi\eta\tilde{R}_i} \cdot \nu' \left(\frac{1}{\tilde{R}_j} + \frac{1}{\tilde{R}_i}\right)^{-\frac{1}{2}} \boldsymbol{k}_{ij}(\tilde{\boldsymbol{r}}_{ij}) \tag{3.30}$$

with

$$\boldsymbol{k}_{ij}(\tilde{\boldsymbol{r}}) = \begin{cases} 0 & \text{for} \quad \tilde{r} > \tilde{R}_i + \tilde{R}_j \\ \left(\tilde{R}_i + \tilde{R}_j - r\right)^{\frac{3}{2}}\hat{\mathbf{e}}_r & \text{for} \quad \tilde{r} \leq \tilde{R}_i + \tilde{R}_j \end{cases} \tag{3.31}$$

where ν' is a material specific constant.
The stochastic differential equation describing the particle dynamics is given by

$$\mathrm{d}\tilde{\boldsymbol{q}}_i = \sum_{j\neq i}\left[\tilde{\boldsymbol{v}}_{ij}^{dip} + \tilde{\boldsymbol{u}}_{ij} + \tilde{\boldsymbol{v}}_{ij}^{rep}\right]\mathrm{d}\tilde{t} + \sqrt{2D_i^p}\,\mathrm{d}\tilde{W}_i\,. \tag{3.32}$$

where D_i^p is the diffusion constant of particle i. The diffusion constant is given by the Stokes-Einstein equation as $D_i^p = \frac{k_B T}{6\pi\eta\tilde{R}_i}$.
We now introduce new dimensionless variables by scaling all distances by a length a, which gives the dimensionless particle positions $\boldsymbol{q}_i = \frac{1}{a}\tilde{\boldsymbol{q}}_i$ and particle distances $\boldsymbol{r}_{ij} = \frac{1}{a}\tilde{\boldsymbol{r}}_{ij}$. a can be an arbitrary length which represents a characteristic scale of the system, e.g., the mean particle radius. Further we introduce dimensionless time t by defining $\tilde{t} = \frac{a^2}{D_i^p}t = \frac{6\pi\eta a^3}{k_B T}t$. We also define dimensionless particle radii via $R_j = \frac{\tilde{R}_j}{a}$ For the stochastic differential equation, we then find

$$\mathrm{d}\boldsymbol{q}_i = \sum_{j\neq i}\left[\alpha_{ij}\boldsymbol{g}_{ij}(\boldsymbol{r}_{ij}) + \beta_{ij}\boldsymbol{h}_{ij}(\boldsymbol{r}_{ij}) + \nu_{ij}\boldsymbol{k}_{ij}(\boldsymbol{r}_{ij})\right]\mathrm{d}t + \sqrt{2\frac{1}{R_i}}\,\mathrm{d}W_i\,. \tag{3.33}$$

with

$$\alpha_{ij} = \frac{6\pi\epsilon E_0^2 a^3}{k_B T}\cdot R_j^3 \tag{3.34}$$

and

$$\beta_{ij} = \frac{6\pi\epsilon E_0^2 a^3}{k_B T}\cdot R_j^3\left(|K_d|^2\,R_i^2 - \frac{\gamma}{2}R_j^2 - \frac{\gamma}{2}R_i^2\right) \tag{3.35}$$

and

$$\nu_{ij} = \frac{\nu' a^3}{k_B T}\frac{1}{R_i}\left(\frac{1}{R_j} + \frac{1}{R_i}\right)^{-\frac{1}{2}}. \tag{3.36}$$

The parameter definitions for equally sized particles can obtained by setting $R_{i/j} = 1$. For the repulsion force we identify the relation $\tilde{\nu} = \frac{\nu' a^3}{k_B T}$ between the parameter $\tilde{\nu}$ used for the monodisperse particle simulation and the parameter ν' used in the polydisperse particle simulation. The vector fields $\boldsymbol{g}_{ij}$, $\boldsymbol{h}_{ij}$ and $\boldsymbol{k}_{ij}$ have the same form under the given scaling as before.

With these new definitions at hand we created a simulation with variably sized particles (Matlab code is available on Github [87]). For the parameters we used $\gamma = 0.088$, $|K_d|^2 = 0.23$ and $\nu' = 75$. γ and $|K_d|^2$ are the same as in the monodisperse particle simulation. We used a smaller value for ν' which corresponds to softer particles. For the particle distribution we used a Weibull distribution with parameters obtained for the

coacervate sample in Figure 3.10. The results are shown in Figure 3.12 and demonstrate that the simulation reproduces all stages of the pattern formation process also for particles with variable sizes.

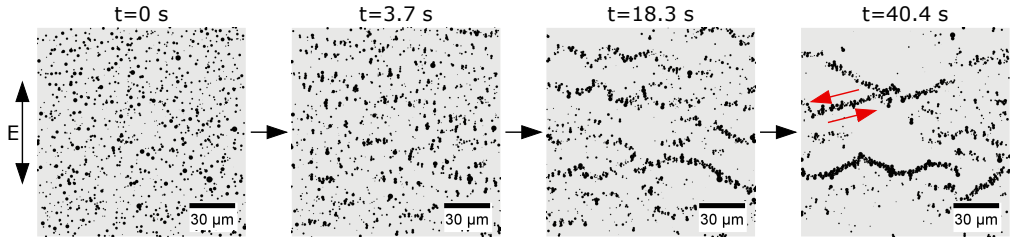

Figure 3.12. Simulation dynamics with Weibull-distributed particle sizes. The particles again circulate as indicated by the arrows.

3.7.3 On the Generality of the Pattern Formation Phenomena

In the general case of an arbitrary colloid, an explicit expression for γ is, unfortunately, unavailable. The model of Ref. [33] used to compute γ for our silica particles assumes hard spheres with a fixed surface charge. The other types of colloids used in our experiments are generally more complex: Coacervates, which are composed of charged polymers, have a diffuse boundary. *E.coli* bacteria have a multilayered cell wall with complex electrochemical properties. Fatty acid and oil droplets are liquid. Even though the surface properties of these colloids are unknown in detail, it is clear that they all have a nonzero surface charge - a high surface charge goes hand in hand with a stable colloidal suspension and is therefore always given [69]. As the proposed mechanism for the fluid motion generating the colloidal patterns is based on ion-selective surface conduction, it should always be at work for a high enough surface charge, independent of its exact spatial distribution.

Despite the unavailability of an explicit expression, we expect a similar scaling for γ for all colloids investigated, i.e., we expect emergence of patterns for salt concentrations lower than $1\,\mathrm{mM}$. The characteristic frequency f_{cr} should be mostly independent of the type of colloid as it is only determined by the time scale of neutral salt diffusion outside of the Debye layer, which lets us expect patterns for frequencies below $1\,\mathrm{kHz}$. Our experiments for the different colloids shown in Figure 3.2 were performed accordingly. We used as little salt as possible and at a low enough frequency ($500\,\mathrm{Hz}$). Nevertheless, in spite of the 'generality' of the phenomenon, we do observe deviations as exemplified by our experiments with bacteria in Figure 3.6, for which we found strikingly different behaviors for $500\,\mathrm{Hz}$ and $250\,\mathrm{Hz}$.

4. Microrobots Powered by Concentration Polarization Electrophoresis (CPEP)

The text and figures in this chapter are adapted from the publication [92] stated below and have been restructured to better suit this thesis. The videos mentioned below are accessible on the publisher's webpage and are referenced accordingly.

Microrobots Powered by Concentration Polarization Electrophoresis (CPEP)

Florian Katzmeier and Friedrich C. Simmel,
Department of Bioscience, TUM School of Natural Sciences, Technical University Munich,
D-85748 Garching, Germany

In light of the generic occurrence of the quadrupole flow around spherical particles discovered in the previous chapter, Friedrich C. Simmel and I concluded that a similar flow should also occur around asymmetric particles in an AC electric field, as shown in Figure 4.1 for a dimer. This induced flow is asymmetric and leads to the propulsion of the particle along the electric field lines. Such propulsion is generally unexpected in the classical picture of electrophoresis of microscopic particles. As demonstrated in Section 2.4.4, electrophoresis is shape-independent, which, coupled with the time reversibility of hydrodynamics at low Reynolds numbers, results in zero net movement in an AC electric field. I named this novel propulsion mechanism "Concentration Polarization Electrophoresis (CPEP)" in accordance with the recently theoretically described mechanism "Concentration Polarization Electroosmosis (CPEO)" [36], which drives the quadrupole flow around spherical particles. To verify the effectiveness of this propulsion mechanism, I designed and constructed the four-electrode setup depicted on the right in Figure 4.1. Furthermore, I established a protocol to synthesize asymmetric dimeric colloidal particles via DNA strand hybridization. With this setup, I was able to steer the dimer particles along arbitrary trajectories using an Xbox controller. Additionally, the setup allowed for the pickup, transport, and release of monomeric cargo particles.

I also conducted characterization experiments, where I measured the dependence of the dimer migration velocity on different frequencies, electric field amplitudes, and buffer

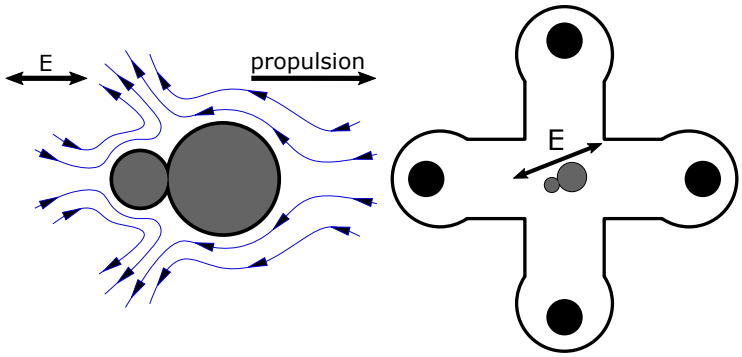

Figure 4.1. Overview Figure: Microrobots Powered by Concentration Polarization Electrophoresis (CPEP). (Left part) Hydrodynamic flow field around a dimer in an AC electric field, resulting in propulsion. (Right part) Experimental setup with an electrode configuration that enables steering of the dimer along arbitrary trajectories.

compositions. I found that these measurements generally fit well into the theoretical picture of "Concentration Polarization Electro-Osmosis (CPEO)".

Lastly, I conducted experiments with a variety of fragmented asymmetric particles to confirm the generic occurrence of CPEP.

4.1 Introduction

According to Smoluchowski's century-old theory, electrophoresis of colloidal particles is shape-independent [8]. In combination with the time reversibility of hydrodynamics at low Reynolds numbers, shape-independence implies that even asymmetric particles will not display any net movement when subjected to a homogeneous AC electric field. However, under experimental conditions which generate nonlinear electrokinetic phenomena, particles with a broken symmetry can experience directed propulsion also in homogeneous AC electric fields. Such AC electrophoretic propulsion was first theoretically proposed [31] for *strongly* polarizable particles based on induced charge electroosmosis (ICEO) [30] and later experimentally verified for metallo-dielectric Janus particles, which were observed to move perpendicular to the electric field direction [76].

In this work, we investigate a novel propulsion mechanism for *weakly* polarizable particles with a non-zero surface charge based on the phenomenon of concentration polarization electroosmosis (CPEO). CPEO was recently theoretically described [36] and experimentally validated [35,36,93,94] and is found to produce similar flow patterns around spheres in an AC electric field as ICEO, but under different experimental conditions. We therefore expected that similar to propulsion via induced charge electrophoresis (ICEP) resulting from ICEO, asymmetric particles subjected to CPEO would also experience directed propulsion, which we accordingly refer to as concentration polarization electrophoresis (CPEP).

In the most widely utilized experimental setup, microswimmers are placed on an electrode and exposed to a vertical electric field. Within this setup, it was demonstrated that asymmetric colloidal dimers [95] and metallo-dielectric Janus particles [81, 96] are propelled perpendicularly to the electric field in a random direction in the 2D plane. To introduce maneuverability, magnetic fields have been used in combination with ferromagnetic metallo-dielectric Janus particles [97] and ferromagnetic asymmetric colloidal dimers [98]. Further, it has been demonstrated that metallo-dielectric Janus particles can be used to transport other dielectric particles [97, 99, 100]. In the case of asymmetric colloidal dimers, the propulsion mechanism is based on the electrohydrodynamic interplay between electrode and particles [101, 102].

Since, in contrast to this propulsion mechanism, CPEO does not require an electrode in close proximity, we surmised that it could be applied to propel asymmetric colloidal dimer particles using an *in-plane* electric field. Taking advantage of electro-orientation [103–106], which orients prolate particles parallel to an AC electric field through induced dipole alignment and induced hydrodynamic flows, we thus expected to achieve directed propulsion of asymmetric dimers *along* the field lines rather than perpendicular to them.

In the following, we demonstrate that asymmetric dimer 'microrobots' can be precisely maneuvered using a straightforward electrical setup without any additional magnetic forces by simply controlling the orientation of an homogeneous AC electric field in the plane of movement. Such AC electrically-controlled 2D actuation was previously only achieved through dielectrophoresis [107], which requires electric field gradients and a computer-controlled feedback mechanism [104, 105]. We also develop a strategy to pick up, transport, and release spherical cargo particles with these microrobots by making use of induced dipole-dipole interactions and hydrodynamic flow fields. Next, we explore the dependence of the microrobots' migration speeds on electric field strength, frequency, and buffer composition, finding that these measurements align reasonably well with the theoretical predictions of CPEO. Lastly, we argue that most particles with broken symmetry can be propelled either through ICEP for metal particles or CPEP for dielectric particles. This leads us to conclude that propulsion in an AC-electric field, namely AC-electrophoresis (ACEP), is a universal phenomenon anticipated for most asymmetric particle types. We validate this by observing directed migration of a variety of asymmetric particles within a homogeneous AC-electric field. These include fragmented ceramic, borosilicate glass, acrylic glass, agarose gel, and ground coffee particles, as well as yeast cells.

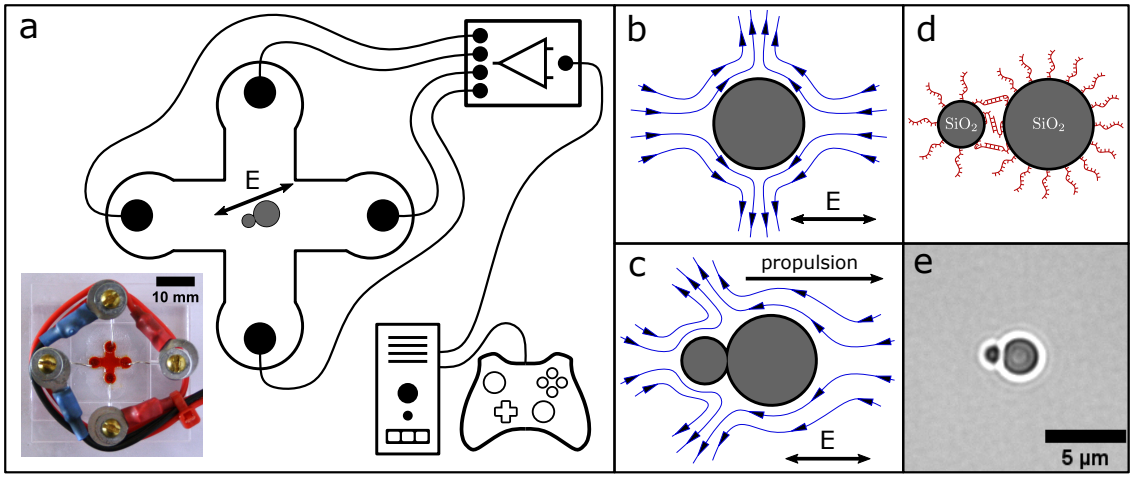

Figure 4.2. (a) Schematic representation and photograph of our experimental setup that enables control of the direction and amplitude of an AC electric field in a microscopy chamber. A dimer is drawn in the center of the cross-shaped fluidic chamber, which aligns with the externally applied AC field through an induced dipole. For visualization, the fluidic chamber in the photograph is filled with a red dye. (b) Electrokinetic flow around a spherical particle arising in an AC electric field. (c) Expected electrokinetic flow around an asymmetric particle dimer in an AC electric field, which results in directed propulsion. (d) DNA modified colloids form a dimer through DNA hybridization. (e) Microscopy image of a particle dimer.

4.2 Results

4.2.1 Asymmetric Colloidal Microswimmers in an AC Electrical Field

It is known that the axisymmetric fluid flow depicted in Figure 4.2b arises around weakly polarizable particles with a non-zero surface charge when subjected to an AC electrical field in a low-ionic strength aqueous medium. Fluid flows towards the particle in the direction of the electric field and is repelled perpendicularly to the electric field [35, 36]. We expected that for an asymmetric dimeric particle an asymmetric flow would arise as proposed in Figure 4.2c that would lead to the propulsion of the particle. We experimentally verified the proposed structure of the flow field using tracer particles (See Section 4.6.4 and Figure 4.13) Further, a dimeric particle will also align with the external electric field as shown in Figure 4.2c and Figure 4.2a due to an alignment torque caused by the induced dipole and fluid flow. In combination with the propulsion this leads to a directed motion along the field lines of the electric field. The movement of the dimers can thus be easily controlled by changing the direction and strength of the external AC electric field.

4.2.2 Experimental Setup and Fabrication of Particle Dimers

For our experiments we designed the sample chamber shown in Figure 4.2a, in which two microfluidic channels equipped with platinum electrode pairs at their inlets intersect in the center. The electric field in the center of the chamber is a superposition of the fields generated by the remote electrode pairs. Hence, the field at the intersection is homogeneous, and its direction and amplitude can be controlled by applying different electric field strengths to the channels [84, 108].

We created two electric signals with the sound card of a computer, which were amplified in two stages using custom-built amplifiers before feeding them into the microchannels. With our setup we can apply AC voltages with an amplitude of up to $305\,\mathrm{V}$ which corresponds to an electric field amplitude of approximately $60\,\mathrm{mV/\mu m}$ in the center of our chamber. We programmed a python script to control the amplitude of the electric signals via the XY-deflection of the analog joystick of a gamepad (an Xbox Controller) which is conventionally used to play video games. As a result, the direction and amplitude of the AC electric field in our sample chamber and thereby the movement of our microrobots can be directly controlled with a joystick while imaging them with a microscope. We also included the possibility to change the field frequency to predefined values $250\,\mathrm{Hz}$ and $750\,\mathrm{Hz}$ by

pressing the buttons available on the controller. Images of the setup together with detailed information on its design and manufacture are given in Section 4.5.1.
Asymmetric particle dimers acting as microrobots were synthesized through the self-assembly of two differently sized, DNA-coated silica spheres with diameters $1.01\,\mu m$ and $2.12\,\mu m$, respectively [109–112]. To this end, each particle type was modified with 60 nt long single-stranded DNA molecules, which had 30 nt long sub-sequences that were complementary to sequences on the respective other particle type. When mixed in the presence of $4\,mM$ $MgCl_2$, the silica spheres specifically bound to each other via DNA duplex formation (cf. Figure 4.2d & e). For our experiments, we diluted the dimers in Tris buffer ($100\,\mu M$, pH 8.4) supplemented with $5.2\,\mu M$ $MgCl_2$. A detailed description of synthesis and sample preparation is given in Section A.1.

4.2.3 Movement and Maneuverability of the Microrobots

Our protocol for the assembly of the silica particles resulted in a mixture of mainly monomers and dimers with only small amounts of higher order multimers. Upon exposure to an AC electric field in our sample chamber, the dimers are subject to a torque due to an induced dipole and fluid flow which aligns the dimer axis parallel to the electric field lines. The dimers can assume two alternative, stable orientations in the AC field, in which the positions of the larger and smaller particle are exchanged with each other (Figure 4.3a). Notably, the induced asymmetric hydrodynamic flow around each dimer propels them in the direction defined by the position of the larger particle. Thus the particle dimers shown in the scheme of Figure 4.3a would be expected to move in opposite directions, as indicated by the blue pointers. To demonstrate this effect in the experiment, we recorded a microscopy video of two differently aligned dimers while slowly changing the direction of the applied electric field using the joystick. As expected, the dimers were observed to move anti-synchronously, meaning that the trajectory of one particle was the point reflection of the other (the image sequence shown in Figure 4.3a is the first part of Supplementary Video 1 [92]; details on video processing are given in Section 4.5.6). All dimers in a sample move along the electric field lines collectively, with the larger particles in the front. We thus focused on the movement of individual dimers in all further experiments.

To demonstrate microrobot maneuverability, we recorded a microscopy video, in which we steered a microrobot along a slalom course around islands of monomeric particles, which remained stationary in the AC field (cf. Figure 4.3b and second part of Supplementary

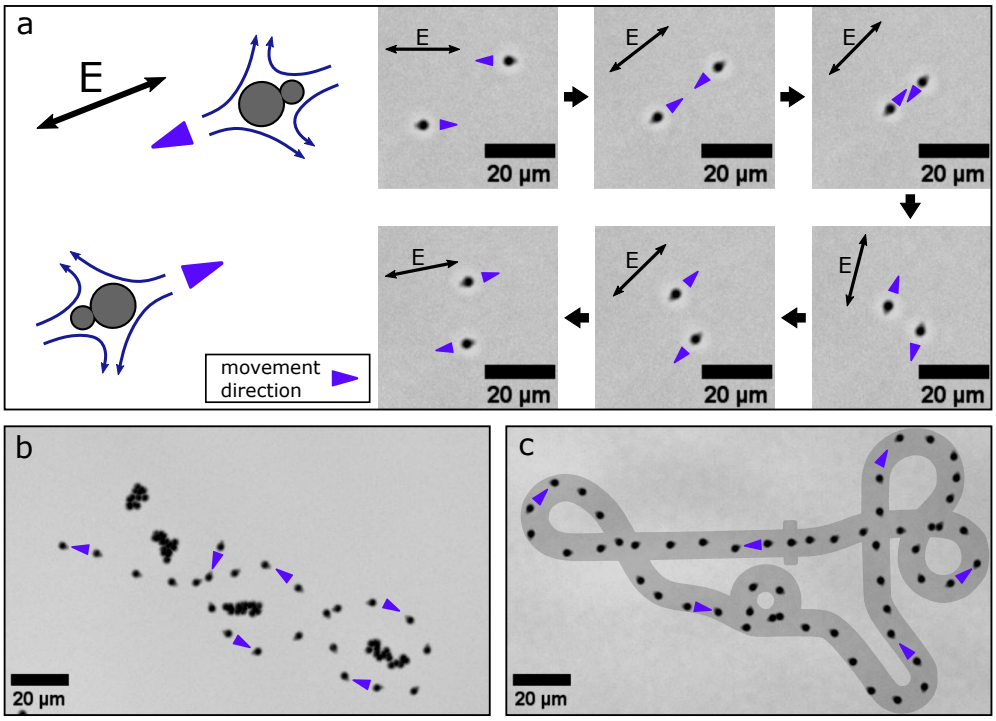

Figure 4.3. Controlled movement of particle dimers. (a) The sketch on the left shows two microrobots aligned with an AC electric field. The orientation of the AC electric field is indicated with a black double arrow. The movement direction is indicated with a blue pointer and is opposite for the two microrobots due to their opposite orientations. The image sequence on the right shows successive frames of a microscopy video demonstrating the resulting anti-synchronous movement in an electric field with slowly changing orientation. (b) By applying joystick-controlled AC voltages a microrobot is maneuvered through a slalom course around stationary monomer particles. The image shows an overlay of successive frames of a recorded microscopy video. Due to Brownian motion, the monomer particles appear as particle clouds, but they do not respond the applied AC electric field. (c) A microrobot is maneuvered along a race track adopted from a well-known video game. The image shows an overlay of successive frames of a recorded microscopy video and the racetrack.

Video 1 [92]). The monomeric particles appear as clouds in the overlay image, since they are subject to Brownian motion. We also found a slight drift in our microscopy videos due to bulk fluid motion which we corrected by tracking several of the stationary monomeric particles and shifting the recorded video by their average displacement.

We also recorded a microscopy video, in which we maneuvered a microrobot along a racetrack adopted from a computer game. For this purpose, we printed the racetrack on a cling film and attached it with tape to the screen of the computer controlling the microscope to enable visual feedback and control by a human operator. Figure 4.3c shows an overlay of the racetrack and video images recorded during the experiment (cf. third part of Supplementary Video 1 [92]).

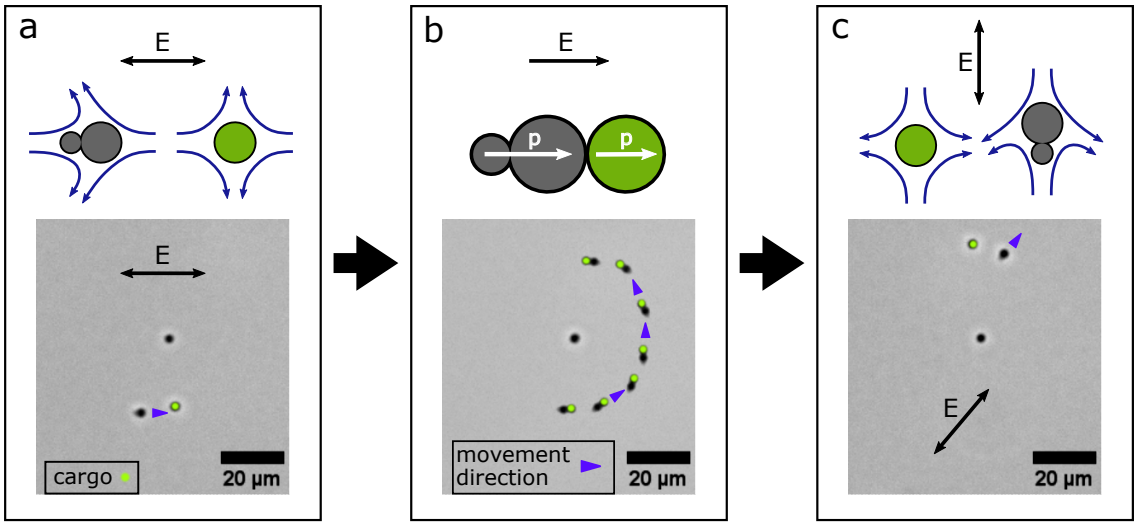

Figure 4.4. Cargo pick-up, transport and release. (a) A microrobot approaches a cargo particle. The direction of motion of the microrobot is indicated with a blue pointer and the cargo particle is labeled with a green dot. The orientation of the AC electric field is indicated with a black double arrow. The fluid flow arising around the microrobot and the cargo particle is illustrated with curved blue arrows in the sketch above and leads to an attraction. (b) A microrobot sticks to a cargo particle via induced dipole-dipole forces. Both are maneuvered around another monomeric particle. The instantaneous induced dipole moments are indicated with white arrows in the sketch above, the electric field is indicated with a black arrow. (c) A cargo particle is released from a microrobot by a quick change in direction of the external electric field. The fluid flow arising around the microrobot and the cargo particle now leads to repulsion.

4.2.4 Pick-up, Transport, and Release of Cargo Particles

We found that the microrobots can be readily used to pick up, transport, and release other, *monomeric* cargo particles, for which we utilized both electric and hydrodynamic interactions between microrobot and cargo. Figure 4.4a shows a microscopy image of a microrobot approaching a cargo particle (shown in green in the image). As illustrated in the sketch above the microscopy image, fluid flows towards both particles in the direction of the electric field and is repelled perpendicularly to it. The microrobot and the cargo particle drift in the fluid flow caused by each other which results in an attractive interaction for the configuration shown.

When in direct contact, the microrobot sticks to the cargo via induced dipole-dipole forces (see Figure 4.4b). Even though we apply an AC electric field, at any point in time the external field induces electric dipoles in both microrobot and cargo, which point in the same direction and thus result in a near-field attraction of the particles. This mechanism is well known and results in particle chain formation in crowded colloidal suspensions. [35,49,113].

We then maneuvered the cargo-loaded microrobot around another monomeric particle as shown in the overlay image in Figure 4.4b. For this image, we corrected the drift in the corresponding microscopy video by moving the tracked position of the monomeric *non-cargo* particle into the center of each frame.

Cargo release (shown in Figure 4.4c) was achieved by switching off the electric field, changing the frequency from $250\,\mathrm{Hz}$ to $750\,\mathrm{Hz}$, and then applying an AC electric field with an orientation roughly perpendicular to the previous field. The corresponding particle configuration and flow fields are illustrated in the sketch above the microscopy image, where the fluid is repelled perpendicularly to the electric field from the particles' equators, resulting in their repulsion. Once the microrobot had moved sufficiently far from the cargo particle, the frequency was reset to $250\,\mathrm{Hz}$. We found that increasing the frequency made it easier to execute cargo release, as the microrobots moved more slowly at higher frequencies. This is presumably caused by lower CPEO flow magnitudes. Additionally, we hypothesize that at higher frequencies the strength of the induced dipole-dipole force decreases relative to the force exerted by the fluid flow. It is worth to note that although the interaction between two parallel-aligned dipoles in this configuration is also repulsive, the particles will always return to a chain formation when they are subjected solely to dipole forces. Importantly, the field lines of the dipole-dipole forces start and end at the dipoles, which prevents the particles from escaping. A video of the cargo transport process is shown in the fourth part of Supplementary Video 1 [92].

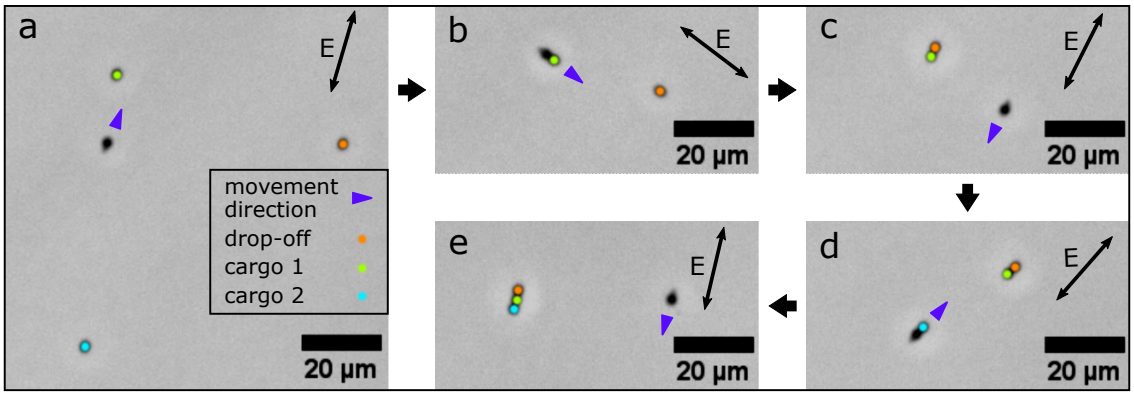

Figure 4.5. Assembly of three monomeric particles into a particle chain. (a) A microrobot approaches cargo particle 1 (labeled with a green dot). (b) The microrobot, loaded with cargo 1, approaches another monomeric particle (orange), which serves as the drop-off location for cargo release. (c) The cargo particle sticks to the orange particle via induced dipole-dipole forces, while the microrobot is maneuvered towards cargo particle 2 (turquoise). (d) The microrobot loaded with cargo 2 heads back towards the drop-off location to release the cargo. (e) The two cargo particles and the orange target particle are assembled into a chain.

4.2.5 Controlled Assembly of Cargo Particles into Particle Chains

Using the same strategy for particle transport and release, we were also able to assemble several monomeric particles into a particle chain. As shown in Figure 4.5 (cf. last part of Supplementary Video 1 [92], the microrobot can be controlled to sequentially pick up two individual cargo particles and drop them off in the vicinity of a third target particle. As a result of the attractive induced dipole-dipole interactions between the monomeric particles, the three particles stick together and form a particle chain.

4.2.6 Amplitude and Frequency Dependence of the CPEO Mechanism

Having established a novel approach for the manipulation of asymmetric colloidal dimers, we intended to verify whether the underlying propulsion mechanism indeed conformed with the theoretical framework for CPEO. We hypothesized that the migration speed of the dimers would scale similarly as the strength of the fluid flow around spherical monomer particles. Like ICEO, CPEO is a second-order phenomenon with respect to the applied electric field and thus the migration speed v should scale with the electric field amplitude E_0 as $v \propto E_0^2$. However, the frequency dependence of CPEO is expected to differ substantially from that of ICEO. Notably, the fluid velocity around spherical particles caused by CPEO falls off to zero for frequencies exceeding the characteristic frequency $f_c = \frac{1}{2\pi} \frac{2D^+D^-}{R^2(D^+ + D^-)}$ [35, 36, 38, 64]. Here, D^- and D^+ denote the diffusion

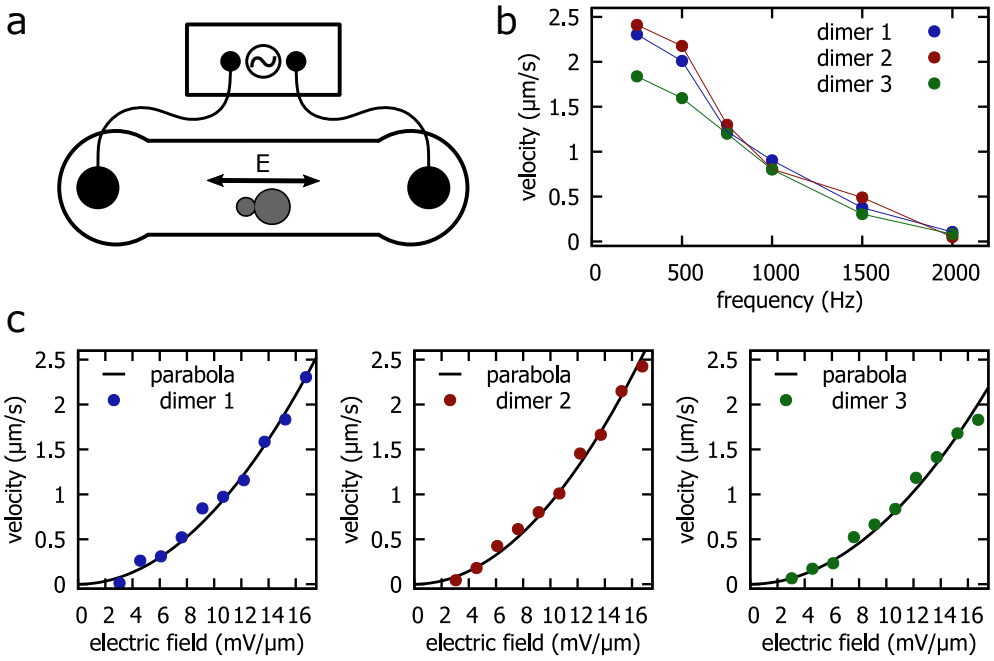

Figure 4.6. Dependence of migration speed on frequency and amplitude of the AC field. (a) Simplified measurement setup. An AC electric field is applied to a linear microscopy channel containing dimers. (b) Migration speed of three different dimers at a constant electric field amplitude of $16.8\,\mathrm{mV/\mu m}$ and varying frequency. The colored lines are a guide for the eye. (c) Migration speed of three different dimers at a constant frequency of $250\,\mathrm{Hz}$ and varying electric field amplitude. The black lines are parabolas ($v = \lambda E_0^2$) fitted to the velocity data.

coefficients of the buffer ions Cl^- and Tris$-H^+$, which are $D^- = 2 \times 10^3\,\mu m^2/s$ and $D^+ = 0.8 \times 10^3\,\mu m^2/s$ at $T = 20\,^\circ C$ [114] and R is the radius of the object. When applying the theory to our dimers, we can interpret R as their typical size, which we take as the average radius of their constituent particles, and with the given parameters we obtain $f_c = 297$ Hz. $1/(2\pi f_c)$ corresponds to the time required for ions to diffuse over the distance R. By contrast, in the case of ICEO the characteristic frequency is derived from the time required to charge the electric double layer on the particle, which is given by the RC time of the corresponding circuit [30, 115].

Table 4.1. Characteristic frequencies f_c and velocity scales v

	CPEO	ICEO metal	ICEO dielectric
characteristic frequency	$297\,$Hz	$5.40\,$kHz	$98.0\,$kHz
velocity scale	$17.5\,\mu m/s$	$175\,\mu m/s$	$0.33\,\mu m/s$

We measured the migration speeds of three different dimers for several voltages and frequencies to verify the above hypothesis. To this end, we employed the setup shown in Figure 4.6a where dimers are placed in a linear microchannel with two electrodes at its opposite inlets. As before, we prepared the dimers in $100\,\mu$M Tris-buffer, which we titrated to pH 8.4 by the addition of HCl and supplemented with $5.2\,\mu$M $MgCl_2$. We then recorded microscopy videos of the migration of the three dimers while applying AC fields with different frequencies and amplitudes. From the start and end positions of the dimers, we computed the distances covered and from these the average migration speeds. We also measured the speed of a monomeric particle as a reference. The corresponding measurements are listed in Tables A.9,A.10 and A.11. Figure 4.6c shows plots of the migration speeds versus the applied electric field amplitude at a constant frequency of $250\,$Hz. As shown, the experimental migration speeds are well described by a quadratic fit $v = \lambda E_0^2$. In Figure 4.6b, the frequency dependence of the migration speeds of the three dimers is plotted for a constant electric field amplitude of $16.8\,mV/\mu m$. We find a decrease of the migration speed in the range of the characteristic frequency $f_c = 297$ Hz calculated for CPEO flows.

For comparison, we computed the characteristic frequency of ICEO flows around metal and uncharged dielectric spheres at our experimental conditions [30, 115]. In addition, we calculated the expected slip velocities around spheres for CPEO and ICEO flows at the highest applied electric field amplitude $16.8\,mV/\mu m$ (Table 4.1) [30, 36, 116]. The corresponding calculation can be found in Section 4.6.1. As mentioned, the frequency response of our dimers agrees best with the characteristic frequency predicted by CPEO, whereas f_c predicted by ICEO for dielectric particles is two orders of magnitude off. The

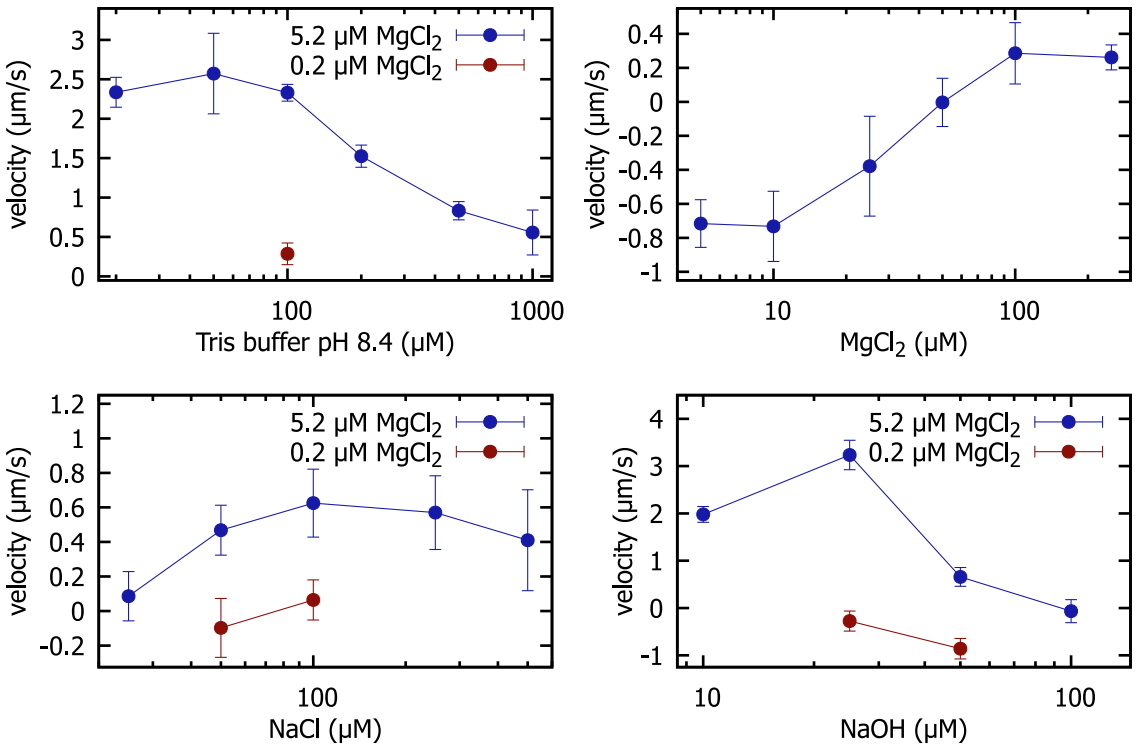

Figure 4.7. Dimer velocities at a constant electric field amplitude of $16.8\,\mathrm{mV/\mu m}$ and constant frequency of $250\,\mathrm{Hz}$ for various buffer conditions. Blue data points indicate measurements with $MgCl_2$ supplemented to the buffer, while red data points correspond to measurements without supplemented $MgCl_2$. Each data point is the average of at least 5 velocity measurements of different dimers, error bars indicate the corresponding standard deviations. Data points with negative velocities correspond to dimers moving backward, which we defined as a movement with the smaller particle in front.

characteristic frequency predicted for strongly polarizable particles, such as metal particles, is closer to the experimentally observed value, but application of this model to our case is physically unreasonable as silica particles are not strongly polarizable. The value for the slip velocity around a sphere calculated from CPEO is found to be one order of magnitude larger than the observed migration speed of our dimers. This result is not unexpected since the slip velocity and the migration speed are not directly equivalent, as also demonstrated in the schematic diagram shown in Fig 4.2c. The migration speed may be further reduced due to the additional drag caused by the nearby channel bottom. Importantly, the slip velocity calculated for ICEO flow around a dielectric sphere is approximately one order of magnitude lower than the observed dimer migration speed.

4.2.7 Buffer Dependence of the Transport Mechanism

We finally also characterized the buffer dependence of the microrobots' migration velocity. CPEO flows are caused by ion-selective surface conduction in the electric double layer at the particle surface, which depends on the zeta potential. The zeta potential, in turn, is a function of the surface charge of the particle and the ionic strength of the buffer solution. The flow is thus expected to be strongest for large surface potentials, i.e., under conditions with large surface charge densities and low ionic strengths. We recorded microscopy videos of dimers prepared in buffers with different concentrations of Tris, NaCl and NaOH, each supplemented with $5.2\,\mu$M $MgCl_2$. In addition, we tested Tris-buffer, NaCl and NaOH without any $MgCl_2$ and also a solution containing exclusively $MgCl_2$. For each buffer composition, we recorded tracks of at least five dimers, and we took care that every video contained at least one spherical particle as a reference. As before, we measured the migration speed by marking the start and end position of the dimer and dividing the resulting distance by the elapsed time. We also measured the migration speed of all spherical particles in each microscopy video and used it as a reference (See Section 4.5.7 for details) The results of these experiments are listed in Tables A.1,A.2,A.3,A.4,A.5,A.6,A.7 and A.8), and are plotted in Figure 4.7.

Overall, the velocities tended to decrease for increasing monovalent salt concentrations, approaching zero velocity for concentrations around $1\,$mM, which is in the range expected for CPEO flows for typical values of the surface charge [35]. The details of the buffer dependence of the particle velocity are intricate, however. We found that supplementing the buffers with $5.2\,\mu$M $MgCl_2$ had a tremendous effect on the migration behavior. For Tris buffer, we found a strong enhancement of the velocity by $MgCl_2$. For NaOH, we found that dimers moved backwards in the absence of $MgCl_2$, while they moved forward in its presence. Notably, when using $MgCl_2$ in dH_2O only, we found backward movement that changed to forward movement at higher concentrations. When present alone and at low concentrations, either NaOH or $MgCl_2$ induced backward movement. However, when combined they induced forward movement. We found the largest migration velocities for NaOH and Tris buffer at pH 8.4, which we attribute to an increase in surface charge caused by the elevated pH. As even small amounts of $MgCl_2$ had an extreme effect on the migration velocity, we took special care to avoid any salt contamination in our samples (See Section 4.5.4 for details).

For an electrokinetic phenomenon such as CPEO, a complex dependence on buffer conditions is not unexpected. The reversal of the direction of movement of the particle dimers could be caused by either a complete flow inversion or by a more subtle change of the cur-

vature of the flow lines around the particles depending on the ionic environment. At the microscopic level, these variations might be associated with the DNA molecules present on the colloidal surface, which are known interact strongly with Mg^{2+} ions [117]. An extended discussion of this phenomenon is provided in Section 4.6.2, 4.6.4 and 4.6.4 with a brief summary provided here.

In particular, we found that the theory by Fernández-Mateo et al. [36], which was developed for binary electrolytes with identical ion diffusion coefficients D, indeed predicts flow reversal around spherical particles for certain values of D. However, in this case flow reversal is restricted to scenarios with unrealistically high zeta potentials ($\zeta > 100\,\mathrm{mV}$) and rather low diffusion constants ($D \approx 500\,\mu\mathrm{m}^2/\mathrm{s}$) (See Figures 4.11 and 4.12). We therefore experimentally examined the flow field around the microswimmers using tracer particles under buffer conditions leading to either backward ($50\,\mu$M of NaOH and $0\,\mu$M of $MgCl_2$) or forward migration ($25\,\mu$M of NaOH and $5\,\mu$M of $MgCl_2$) (Supplementary Videos 3 & 4 [35]). The results of these experiments suggest that the flow lines are differently curved around the swimmer particles for the two movement directions rather than simply inverted (See Figure 4.13).

To determine whether the reversal of migration direction is linked to the DNA surface modification, we measured the mobility of our $1.0\,\mu$m silica particles with and without DNA using electrophoretic light scattering, under buffer conditions corresponding to either forward or backward migration. We observed no significant differences between both particle types, suggesting a negligible impact of the DNA. Interestingly, the presence of $5\,\mu$M $MgCl_2$ significantly altered the mobility of the monomers, which is consistent with the strong screening effect of the divalent Mg^{2+} ions. We estimated the surface charge from the mobility using the Smoluchowski equation and the Poisson-Boltzmann equation, revealing that the additional $5\,\mu$M of $MgCl_2$ strongly altered the mobility without appreciably affecting the surface charge. Considering the pronounced effect of even small quantities of Mg^{2+} ions on the mobility, we suggest that a detailed calculation of the dimensionless flow velocity for mixed electrolytes, including divalent ions, could provide mechanistic insight into the reversal of the migration direction of the microswimmers.

4.2.8 Universality and Interplay of CPEP and ICEP in AC Electrophoresis

As a general comment, we would like to note that AC electrophoresis (ACEP) in a homogenous AC-electric field is a generic phenomenon that should be expected for most particle types with a broken symmetry under the appropriate experimental conditions, i.e.,

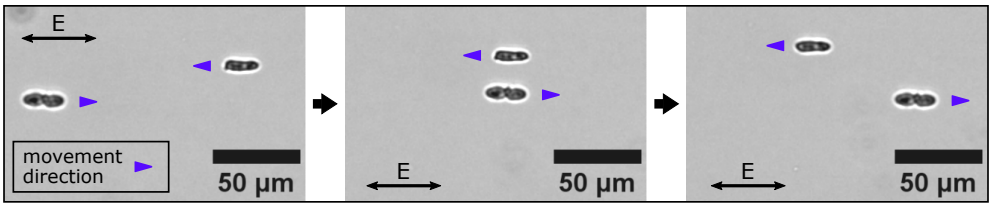

Figure 4.8. Selected frames from a video showing an individual yeast cell and a yeast cell doublet subjected to an AC electric field. The cells migrate in opposite directions, parallel to the electric field, and pass each other.

at sufficiently low salt concentrations and an externally applied frequency that matches the characteristic frequency of the particles. The underlying mechanisms for ACEP are the well-established ICEP for metal particles and CPEP (described in this paper) for dielectric particles with a non-zero surface charge. Importantly, all electrostatically stabilized colloidal dispersions inherently meet the non-zero surface charge requirement for CPEO flows. In our previous work [35], we have demonstrated that a variety of particles, including fluorocarbon (FC) oil and lauric acid droplets, coacervates, silica particles, E. coli bacteria, and ground coffee, are subject to CPEO flows. As it is the case for our microrobots, CPEO flows around an arbitrary asymmetric particle will be asymmetric which will lead to a propulsion in a direction determined by the shape of the particle.

To confirm the universality of CPEP, we conducted experiments with a variety of charged dielectric particle types exhibiting broken symmetry, including fragmented ceramic, borosilicate glass, acrylic glass, agarose gel debris, ground coffee particles, and even yeast cells (Supplementary Video 2 [92]). Using the setup illustrated in Figure 4.6a, we exposed these particles to a homogeneous AC electric field with an amplitude of $16.8\,\mathrm{mV/\mu m}$ and a frequency of $250\,\mathrm{Hz}$. As demonstrated in Supplementary Video 2 [92], we indeed observed the expected, directed migration for all asymmetric particle types. The particles moved predominantly along the electric field lines, even though some migrated at an angle to the field. As an example, Figure 4.8 shows three selected frames from a microscopy video, in which an individual yeast cell and a yeast cell doublet pass each other, while moving in opposite directions.

We conjecture that for composite particles (e.g., metallo-dielectric Janus particles), ICEP is not an isolated phenomenon. A CPEO flow may occur along with the ICEO flow generated on the metallic side, provided the dielectric Janus face is sufficiently charged. Given that ICEO and CPEO flows operate at different characteristic frequencies, their interplay would depend on the applied frequency. A similar argument can be made for particle dimers exposed to a vertical electric field. These should also be subject to CPEO flows in addition to the flows created at the electrode, when AC electric fields are applied within

the frequency range defined by the corresponding characteristic frequency.

4.3 Discussion

A wide range of AC-electrophoretic propulsion strategies have been developed in the past years, which differ from our approach in several aspects. In general, there are two possible electric field geometries - either microswimmers are positioned on top of large electrodes and exposed to vertical electric fields [81, 95–100, 118–122] or they are subjected to in-plane electric fields using remote electrodes [76, 123] as employed in our study. In both configurations, the applied electric field must be large enough to generate a voltage drop across the particle on the order of the thermal voltage $k_B T/e$. Due to the shorter distance between the electrodes, vertical electric field setups typically require lower voltages, making them easier to implement.

Vertical electric field configurations, however, induce propulsion only in a random direction perpendicular to the field. To achieve directional motion or steerability with microswimmers in such setups, magnetic fields have been employed, requiring additional external magnets and the use of appropriate magnetic microparticles. [97, 98, 100, 119, 120] By contrast, employing in-plane electric fields - such as in this work - naturally provides alignment and steerability through electro-orientation [103–106] of the microswimmers. This results in an overall simpler experimental setup and more design flexibility for the swimmers as they do not have to be magnetic.

The two electric field configurations can be implemented in combination with two basic microswimmer designs - metallo-dielectric Janus particles [76,81,96,97,99,100,118–121,123] and asymmetric colloidal dimers [95, 98]. Both microswimmer designs are expected to exhibit propulsion in both electric field configurations. The propulsion mechanisms of each combination differ, each being associated with a distinct characteristic frequency that must be matched with the frequency of the external electric field in order to achieve propulsion. The characteristic frequencies range from the lower MHz range for Janus particles in vertical electric fields, which are driven by self-dielectrophoresis [96], to the lower kHz region for ICEO-driven metallo-dielectric Janus particles [76], to the $297\,\mathrm{Hz}$ needed to propel our asymmetric colloidal dimers by CPEO. Overall, the CPEO mechanism can be applied to the broadest class of particles that can be used as microswimmers, as only particle asymmetry and a surface charge is required. This offers great design flexibility and even allows the use of biological and soft materials as microswimmers, overcoming the need for hard, durable substrate particles that are required for metal deposition to manufacture Janus particles.

To implement effective cargo transport, both attractive and repulsive interactions between microswimmer and cargo are necessary to establish an efficient loading and release mechanism. In our setup, this is accomplished through the geometry of the induced hydrodynamic flow, which can be either attractive or repulsive, depending on the particle-cargo configuration. The only alternative strategy known to balance these interactions employs Janus particles in vertical electric fields, where cargo particles are either repelled or attracted to the dielectric or metallic side based on the applied frequencies. This strategy has been previously implemented using specially designed ferromagnetic metallo-dielectric Janus particles, allowing for steerability and directed cargo transport [97, 100, 120].

4.4 Conclusion

In conclusion, we have introduced a novel approach towards AC electrophoretic (ACEP) manipulation of colloidal microswimmers, namely concentration–polarization electrophoresis (CPEP), which facilitates precise electrical control over two-dimensional movements. In contrast to other approaches for electrically driven swimmers, the utilization of concentration–polarization electroosmosis (CPEO) and electro-orientation enables the use of in-plane electric fields to move the particles in the direction of the field lines, rather than perpendicular to them, as in other approaches. Directed movement requires asymmetric particles with a surface charge, but the particles themselves do not need to be 'Janus' or magnetic, which broadens the design possibilities for electrically controlled microrobots. In our case, two differently-sized silica particles were connected using DNA linker molecules. We employed a relatively simple setup to achieve 2D actuation, which did not require additional magnetic fields, as in the case of dimers or Janus particles subject to a vertical electric field, nor computer-controlled feedback, as in the case of dielectrophoretically driven microswimmers. As demonstrated by the joystick-controlled actions, our approach is of immediate interest for applications in microrobotics. The microrobots can move along arbitrarily chosen paths in 2D and can be directed to controllably pick up, release, and also assemble particles into groups. Further, we confirmed that the dependence of our microrobots' migration speed on the AC electric-field frequency, amplitude, and electrolyte concentration aligns with the theoretical expectations for CPEP. Finally, we confirmed that CPEP applies to a broad class of dielectric particles with a broken symmetry and non-zero surface charge by observing the directed migration of a variety of asymmetric particles subject to a homogenous AC-electric field. From this, we conclude that AC electrophoresis (ACEP) in a homogeneous AC-electric field, governed by ICEP for metal particles and CPEP for dielectric particles, is a universal phenomenon expected for most

asymmetric particles.
Looking ahead, the generic nature of ACEP opens up opportunities for frequency-dependent particle sorting or precise positioning of particles, as their unique size, shape, and composition should result in distinct frequency responses, enabling their selective manipulation. Further, it is conceivable to let microrobots assemble other microparticles into defined superstructures, which themselves could then also act as microrobots, potentially laying the basis for a simple form of 'self-replication'. One of the main challenges for future applications, however, will be the realization of operating conditions that are compatible with useful chemical or biochemical reactions.

4.5 Materials and Methods

4.5.1 Design of the Experimental Setup and its Operation

The bottom part of our microscopy chamber is a glass cover slide. The PMMA part is glued to the glass slide with Dichloromethane. We use platinum wires (Merck: Art. No. 267201-400MG) with a diameter of 0.5 mm as electrodes.
The design of our self-made sample chamber is inspired by that of Kopperger et al. [84]. Photographs of our experimental setup are shown in Figure 4.9. The sample chamber is shown in Figure 4.9a, where it is filled with a red dye for better visualization. The sample chamber consists of two parts. Its bottom is constituted by a glass cover slide (Carl Roth: Art. No. CEX2.1), whereas its top is made from a piece of PMMA, from which the channel geometry has been milled out via micro-milling. Both parts are glued together with Dichloromethane (Carl Roth: Art. No. 8424.2). The gluing process is illustrated in Figure 4.10. First, the PMMA part is placed on the glass cover slide. Then small drops of dichloromethane are placed with a glass pipette at the edge of the PMMA part. Due to capillary forces, the drops wet the surface between the PMMA and the glass slide. The dichloromethane dissolves the surface of the PMMA. The PMMA part is then pressed gently with a finger onto the glass cover slide until the dichloromethane is dried.
Figure 4.9b and Figure 4.9c show the electrode mounting, where four electrodes are fixed on a PMMA frame. The electrode mounting was milled from a 10 mm PMMA sheet. The electrodes extend out of small holes from the PMMA frame and are clamped with a screw from above (see red arrow in Figure 4.9b with the label "electrode fixture"). In Figure 4.10c the electrode mounting is placed on the sample chamber such that the electrodes extend into the inlets of the sample chamber, resulting in an operational setup.

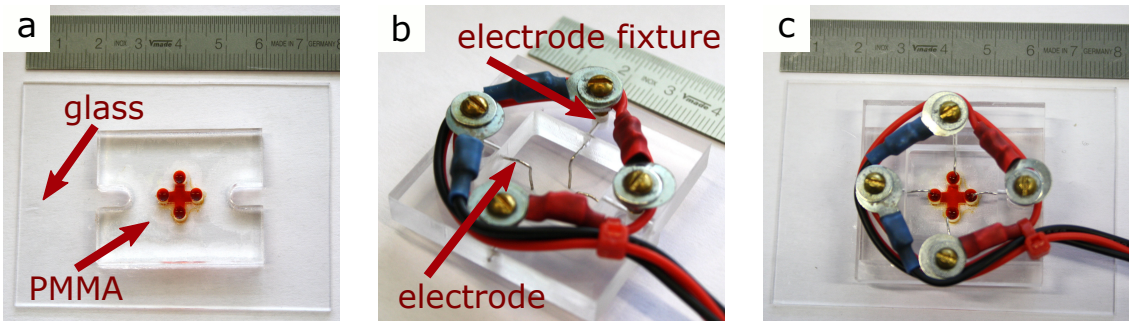

Figure 4.9. Photographs of the experimental setup. (a) Sample chamber filled with a red dye. (b) Electrode mounting. (c) Electrode mounting placed on the sample chamber.

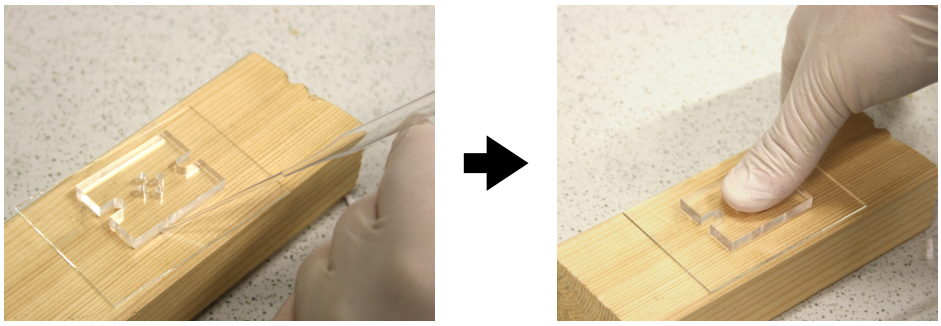

Figure 4.10. Illustration of the glueing process used for manufacturing the sample chamber.

We use a standard Xbox Controller (PDP 049-012-EU-RD Controller Xbox Series X Rot) connected via an USB-cable to the microscope computer to control electrical signals generated by the sound card of the computer. For microscopy, we used an Olympus IX71 inverted microscope equipped with a 20x objective (Olympus UPlanFL N 20x/0.50) and an 100x objective (Olympus PlanApo 100x/1.40 Oil). During our screening experiments we monitored the current and voltage with a digital oscilloscope (PicoScope 2000) to avoid systematic errors. Electric signals for our screening experiments were created with a function generator (RIGOL DG812) and amplified with an amplifier built in-house.

4.5.2 Functionalization and Dimerization of Colloidal Particles

Carboxylated silica spheres with diameters $1.01\,\mu m$ (Lot: SiO_2-COOH-AR756-5ml) and $2.12\,\mu m$ (Lot: SiO_2-COOH-AR1060-5ml) were purchased from microParticles GmbH. We modified the surface of the silica spheres by activating the carboxyl groups with 1-Ethyl-3-(3-dimethyl-aminopropyl) carbodiimide (EDC) and coupling them to amino-modified DNA. [124, 125] The colloids were reacted in $200\,\mu L$ of $100\,mM$ MES buffer (pH 4.8 adjusted with HCl and NaOH) containing $250\,\mu M$ amino-modified DNA and $250\,mM$ EDC

(Merck: Art. No. E6383-1G) on a rotator at room temperature for 3 h. We used colloid concentrations of $11.35 \cdot 10^9$/mL and $50 \cdot 10^9$/mL of the $2.12\,\mu$m colloids and the $1.01\,\mu$m colloids, respectively, to account for the different surface areas of the colloids. The colloids were then washed and incubated extensively in borate buffer (boric acid adjusted to pH 8.2 with NaOH) and deionized water to get rid of remaining reaction components and to hydrolyze unreacted activated carboxyl groups. We avoided using buffers containing amino groups for washing as we wanted to preserve the negative surface charge of the colloids. An extended protocol with details on the washing procedure is given in Section A.1. Finally, the colloids were diluted to concentrations of $2.27 \cdot 10^9$/mL ($2.12\,\mu$m colloids) and $10 \cdot 10^9$/mL ($1.01\,\mu$m colloids) in deionized water, shock frozen in liquid nitrogen and stored at $-80\,^\circ$C.

Our two DNA strands are 60 nucleotides (nt) long and are each composed of a 30 nt long spacer region followed by a 30 nt region which is complementary to the corresponding region on the other strand. The spacer provides flexibility in the distance between the colloids where hybridization can take place. We designed our DNA sequences with NUPACK [126] such that they have no secondary structure. The oligonucleotides were purchased from Integrated DNA Technologies as dried pellets, their sequences are listed in Section A.1.1. We diluted our DNA strands in deionized water and stored them at $-20\,^\circ$C.

4.5.3 Microrobot Assembly

We assembled our microrobots by incubating concentrations of approximately $1.6 \cdot 10^9$/mL of each colloid with $4\,$mM $MgCl_2$ in a reaction volume of $25\,\mu$L for 45 min on a rotator. The above colloid concentration assumes that no colloids were lost in the above washing procedure. The reaction is stopped by rapid dilution of the sample by a factor of 1 to 1000 in deionized water. The sample is handled with special care as we found that shaking causes the microrobots to disintegrate. For further use, we usually diluted our microrobots again by a factor of 1 to 20 in a buffer of choice. The microrobots were assembled freshly for every day of experiments.

4.5.4 Sample Preparation

In initial experiments, we found a reduction in the migration speed after washing our pipette tips. We therefore suspected that the pipette tips contained trace amounts of divalent ions. In order to establish stable and reproducible behavior of the swimmers, we henceforth cleaned all pipette tips and the sample chamber with deionized water before

usage. With every fresh pipette tip, we pipetted deionized water three times before pipetting an actual sample. We also washed all used reaction tubes with deionized water before usage, vortexed them and removed the deionized water again. For our screening experiments, we used commercial microscopy chambers purchased from ibidi (µ-Slide VI 0.4; Cat.No:80601). Before usage, the microscopy chambers were filled three times with deionized water and then blown dry with nitrogen gas. For our experiments with Tris-buffer, we created a 50 mM stock solution at pH 8.4 by titrating Tris (Carl Roth: Art. No. 4855.2) with HCl. We avoided using NaOH in case of overshooting pH 8.4 as this would have resulted in an unknown concentration of additional NaCl in the buffer.

4.5.5 Preparation of Fragmented Particles

We produced fragmented particles from a variety of materials as described below. Following their production, the fragments were washed to remove electrolytes and prepare them for use in our experiments. To this end, we immersed the particles in 1 mL of deionized water in a 1.5 mL Eppendorf tube. We centrifuged the resulting suspension, adjusting the duration and centrifugal forces depending on the stability of the particles. The supernatant was subsequently discarded, and the tube refilled with 1 mL of deionized water. This washing process was repeated three times. Finally, we diluted the washed suspension by an empirical factor using the same buffer as in our microrobot experiments, i.e., 100 µM Tris buffer at pH 8.4, supplemented with 5.2 µM $MgCl_2$. We finally adjusted the dilution to obtain a particle density appropriate for imaging. *Agarose gel:* We mixed 1.5 g of agarose powder (Agarose NEEOP Ultra-Qualität; Art.-NR.2267.3) from CARL ROTH with 30 mL of deionized water. We dissolved the agarose by heating in a microwave oven. We then poured the hot agarose solution into a glass Petri dish and let it cool and solidify for approximately 20 min. Once solidified, we gently scratched the agarose surface using a scalpel, moving the blade perpendicularly to the cutting edge across the gel surface. We collected around 20 mg of the agarose gel fragments in a 1.5 mL Eppendorf tube and filled it up to 1 mL with deionized water. For the washing process, we centrifuged for 1 min at 1000 rcf. Finally, we diluted the washed gel fragments by a factor of 20. *Borosilicate glass:* To obtain glass fragments, we mechanically pulverized a borosilicate glass capillary (BOROSILICATE GLASS; ITEM #: BF150-86-7.5) from Science Products GmbH placed between two glass microscopy slides (Objektträger 76 x 26 mm; Art.Nr.0656) from CARL ROTH. We recovered the resulting glass powder by pipetting 100 µL dH_2O onto the slide and transferred it into a 1.5 mL Eppendorf tube that was filled up to 1 mL with deionized water. For the washing process, we centrifuged for 1 min at 1000 rcf, followed by dilution

1:5. *Acrylic glass:* Acrylic glass fragments (Poly(methyl methacrylate)) were produced using a fine metal file. We collected approximately 2 mg of the resulting powder suspended it in 1 mL of deionized water within a 1.5 mL Eppendorf tube. For the washing process, we centrifuged for 1 min at 1000 rcf, followed by dilution 1:10. *Brewers yeast:* We extracted a turbid suspension of brewer's yeast cells from a sample of Bavarian wheat beer with a pipette and transferred 1 mL of the suspension into a 1.5 mL Eppendorf tube. For the washing process, we centrifuged at 250 rcf for 4 min. Finally, we diluted the washed cells by a factor of 20 in Tris buffer. *Ceramic:* We created small ceramic fragments by placing a splinter from a coffee mug of the size of a fingertip between two aluminum sheets and grinding it. We transferred approximately 2 mg of the resulting powder into a 1.5 mL Eppendorf tube and filled it with 1 mL dH_2O. For washing, we centrifuged at 1000 rcf for 1 min, and finally diluted the washed ceramic fragments 1:5 in Tris buffer. *Coffee:* We pipetted 1 mL of coffee (prepared using standard procedures using very finely ground coffee beans) into a 1.5 mL Eppendorf tube. For the washing process, we centrifuged the suspension at 1000 rcf for 1 min, followed by dilution 1:5.

4.5.6 Video Editing

We used ImageJ to edit our videos. We corrected the drift in the corresponding microscopy video by tracking the monomeric particles with the ImageJ plugin TrackMate [127] and shifting the recorded video by their displacement. Overlay images were created by computing the minimum intensity of a collection of frames from a microscopy video. We adjusted the contrast and brightness of our videos and images such that they appear alike. The final video editing was done with the freely available software Shotcut [128].

4.5.7 Data Analysis

We marked the start and end positions of every microrobot and reference particle in a video and saved the coordinates with the corresponding frame number. We also recorded the instantaneous orientations of every microrobot, which lets us identify backward and forward movements. For that purpose, we used an ImageJ macro to automatize the data analysis. We computed the velocities of all microrobots and reference particles by subtracting the y-coordinates of the start and end positions and dividing the result by the elapsed time. The elapsed time was extracted from the metadata of the corresponding video. We then computed the average velocity of all reference particles in a video and subtracted the velocity of every microrobot in a video by the result, which gives us the corrected microrobot velocities. The average and standard deviation are then computed

from the corrected velocities of all videos with the same buffer conditions. All measured velocities and the recorded microrobot orientations for our buffer characterization experiments are listed in Tables A.1,A.2,A.3,A.4,A.5,A.6,A.7 and A.8). In our frequency and electric field characterization experiments, we were interested in the response of a single microrobot and reference particle. We therefore applied a simplified data analysis procedure and measured only the speed of the single microrobot and reference particle in a video. The recorded measurements are listed in Tables A.9,A.10 and A.11.

4.5.8 Programming

We used the online tool ChatGPT [129] based on GPT3 [130], a Generative Pretrained Transformer developed by OpenAI, to assist with programming.

4.6 Supplementary Results

4.6.1 Characteristic Frequencies and Velocity Scales

In this Section, we compute the characteristic frequencies and magnitudes of the slip velocity for CPEO flows around charge dielectric particles and for ICEO flow around dielectric and metallic particles. We use the average particle radius $R = 0.78\,\mu\text{m}$ of the two particles composing our dimers as the typical size. Further, we use the inverse averaged diffusion constant as used by [36] and [115] for the diffusion constant which is defined by $D = \frac{2D^+D^-}{D^+ + D^-}$. D^+ and D^- are the ion diffusion constants for TrisH^+ and Cl^-, respectively, and are given by $D^+ = 800\,\mu\text{m}^2/\text{s}$ and $D^- = 2000\,\mu\text{m}^2/\text{s}$. Numerically, $D = 1143\,\mu\text{m}^2/\text{s}$ for this case.

The characteristic frequency of ICEO flows around metal particles is derived from the charging time $\tau = \lambda R/D$ [30] of the electric double layer on the particle surface, where λ is the Debye screening length and depends on the ionic strength c. A concentration of $c = 50\,\mu\text{M}$ corresponds to $\lambda = 43\,\text{nm}$. The characteristic frequency is then given by

$$f_c = \frac{1}{2\pi}\frac{D}{\lambda R}, \tag{4.1}$$

which results in $f_c = 5396$ Hz.

For ICEO flows around dielectric particles the characteristic time scale is given by $\tau = \lambda^2/D$ [30] which corresponds to a characteristic frequency of

$$f_c = \frac{1}{2\pi}\frac{D}{\lambda^2}, \tag{4.2}$$

which gives $f_c = 98.0\,\text{kHz}$.
Note that the equation for the characteristic time scale for dielectric particles in [30] has an additional erroneous factor ϵ_w/ϵ_d (see their equation 6.14). ϵ_w/ϵ_d is the fraction of the dielectric constants of water and the particle. The equation above can be obtained when starting from their equation 6.7 and by following the steps stated in the paper. Additionally, one has to assume $\frac{1+\epsilon_w/\epsilon_d}{\epsilon_w/\epsilon_d} \approx 1$, which is reasonable as in most cases $\epsilon_w \gg \epsilon_d$.
The characteristic time scale for CPEO flows is independent of the Debye screening length and is given by $\tau = R^2/D$ [36]. Here, τ is the typical time that ions need to diffuse across the length of our dimer. The characteristic frequency is given by

$$f_c = \frac{1}{2\pi}\frac{D}{R^2}, \tag{4.3}$$

which for our parameter settings is $f_c = 297\,\text{Hz}$.
The slip velocity V for ICEO flows around a metal particle is given by

$$V = \epsilon_w \frac{RE^2}{\mu} \tag{4.4}$$

where ϵ_w is the dielectric constant of water and μ is the viscosity. When using the maximum applied electric field amplitude $E = 16.75\,\text{mV/µm}$, we obtain $V = 0.33\,\text{µm/s}$.
The slip velocity V for ICEO flows around a dielectric particles is given by

$$V = \frac{3}{4}\epsilon_d \frac{\lambda E^2}{\mu} \tag{4.5}$$

where ϵ_d is the dielectric constant of the particle [116]. We used the relative permittivity of 3.7 for silica to compute ϵ_d. When again using the maximum applied electric field amplitude we get $V = 0.33\,\text{µm/s}$.
The slip velocity V for CPEO flows around a charged dielectric particle is given by

$$V = U\epsilon_w \frac{RE^2}{\mu} \tag{4.6}$$

where U is the dimensionless velocity computed which has typically a magnitude of $U = 0.1$ (see below and in [36]). For the maximum applied electric field amplitude this results in $V = 17.47\,\text{µm/s}$.

4.6.2 Propulsion Direction

In this Section, we further investigate the observation that the migration direction of the microswimmers is influenced by the buffer composition, specifically by the presence or absence of $MgCl_2$. The observed change in the migration direction could be attributed either to a complete inversion of the hydrodynamic flow or to a different curvature of the flow lines. The results obtained by Fernandez Mateo et al. [36], who computed the magnitude U of CPEO flows around spherical particles in AC-electric fields, show that flow reversal is theoretically feasible. However, this reversal occurs under physical conditions that are difficult to achieve, such as exceedingly high zeta potentials ($\zeta > 100\,\mathrm{mV}$) and unrealistically low ionic diffusion coefficients ($D \approx 500\,\mu\mathrm{m}^2/\mathrm{s}$). We therefore used tracer particles to experimentally investigate the flow field for both migration directions. The flow fields derived from these experiments indicate that the flow field around the dimer is merely differently curved for the different conditions, but not reversed. Finally, we studied the impact of the DNA modification and $MgCl_2$ on the surface properties of our microswimmers by measuring the electrophoretic mobility of the monomer particles via electrophoretic light scattering. We found that the DNA modification did not alter the monomer mobility which suggests that the inversion of the migration direction is in fact not related to the DNA modification. Our results indicate that small amounts (5 µM) of $MgCl_2$ significantly alter the monomer mobility but do not change the surface charge. Since Fernandez Mateo et al.'s result for the flow velocity only applies to monovalent ions with identical diffusion constants, the significant effect of even small amounts of divalent magnesium ions on the mobility lets us to surmise that a more general theory for the dimensionless flow velocity might elucidate the reasons for the observed migration direction reversal.

4.6.3 Flow Reversal

In this Section, we plot the result of [36] for the dimensionless flow magnitude U of CPEO flows around spherical particles for different ion diffusion constants. Their result for U is a function of the zeta potential ζ, the Dukhin number Du, and the ion diffusion constant D. The Dukhin number is a dimensionless quantity that characterizes the surface conduction of colloidal particles. In Figure 4.11, we plot the dimensionless flow magnitude U versus the dimensionless frequency $2\pi f/(D/R^2)$ for different ion diffusion constants D and Dukhin numbers Du at a constant zeta potential $\zeta = 101\,\mathrm{mV}$. The plot on the upper left is a recreation of a plot shown in [36], where we plotted the frequency response of U for the ion diffusion constants of KCl ($D = 2036\,\mu\mathrm{m}^2/\mathrm{s}$) and four different values

of the Dukhin number. In the other plots, we decreased the diffusion constant. We find decreasing velocities for the higher Dukhin numbers, 1 and 10, for decreasing values of the ion diffusion constant. For very low diffusion constants ($D = 226\,\mu m^2/s$) and Dukhin numbers of 1 and 10, we find flow reversal at low frequencies.

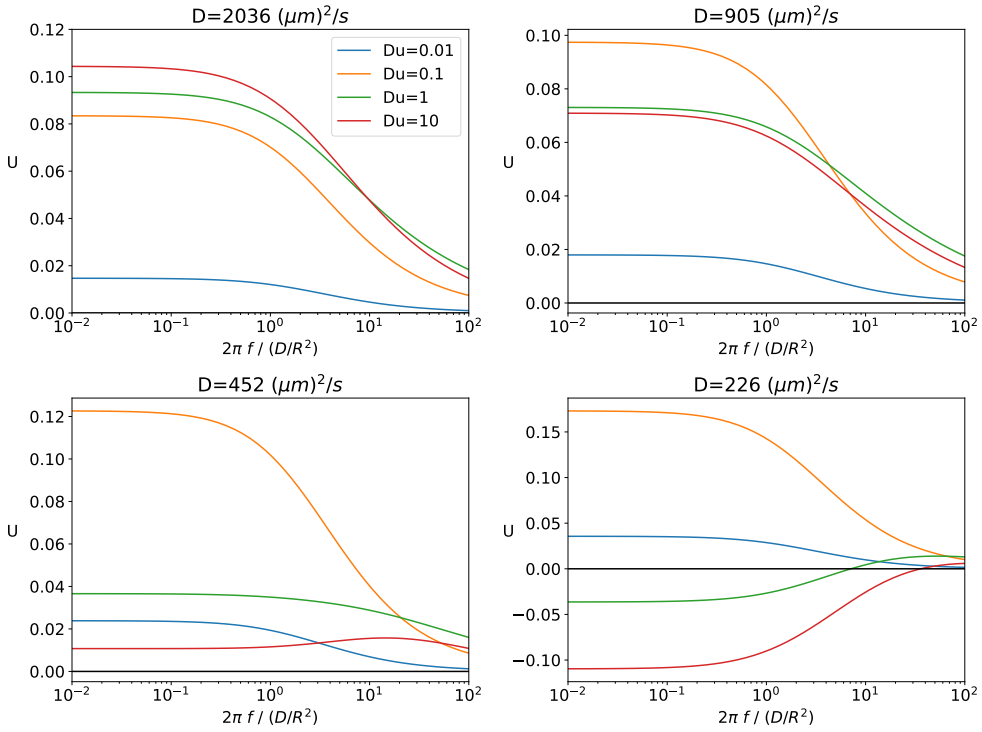

Figure 4.11. Plots of the frequency response of the dimensionless flow magnitude of CPEO flows around spheres for different diffusion constants D and Dukhin numbers Du. The dimensionless zeta potential was set to $\zeta = -4$. The upper left plot is a recreation of the plot shown in [36]

In Figure 4.12, we systematically plotted the frequency response of the flow magnitude for different values of the surface charge density σ. Within one graph, we plotted the frequency response for several values of the ion diffusion constant. Note that the zeta potential ζ is a function of the surface charge density and the Debye length λ, which is in turn a function of the salt concentration c that we set to $\lambda = 43\,\text{nm}$ and $c = 50\,\mu\text{M}$. We assume a particle radius of $R = 0.78\,\mu\text{m}$. We vary the surface charge since both the Dukhin number and the zeta potential are functions of the surface charge. For low surface charges ($\sigma = -0.0005\,\text{C/m}^2$, $\sigma = -0.0010\,\text{C/m}^2$, $\sigma = -0.0015\,\text{C/m}^2$) and low zeta potentials, we find overall increasing flow magnitudes U for increasing surface charges. However, at high surface charges ($\sigma = -0.0045\,\text{C/m}^2$, $\sigma = -0.0080\,\text{C/m}^2$,

$\sigma = -0.0160\,\mathrm{C/m^2}$), we find decreasing flow magnitudes for increasing surface charges, which decrease more strongly for lower ion diffusion constants. This leads, at a certain point, to a flow reversal at low frequencies. Interestingly, the graphs cross the zero line at higher frequencies and become positive again. Overall, we find that flow reversal can indeed occur for high surface charges and low diffusion constants. However, the required values for the surface charges/zeta potentials ($\zeta > 100\,\mathrm{mV}$) and the diffusion constants ($D \approx 500\,\mu\mathrm{m^2/s}$) are physically rather unrealistic.

4.6.4 Visualization of the Hydrodynamic Flow Field

In order to gain further insight into the reversal of migration direction, we experimentally visualized the hydrodynamic flow which propels our microswimmers (see Figure 4.2). To this end, we recorded brightfield videos at a 60x magnification, capturing a migrating microswimmer surrounded by smaller spherical particles serving as tracers. We specifically studied conditions under which the microswimmer either migrated forwards ($25\,\mu$M NaOH and $5\,\mu$M $MgCl_2$) or backwards ($50\,\mu$M NaOH and $0\,\mu$M $MgCl_2$).

As tracer particles we used unmodified silica spheres from Microparticles GmbH, with a diameter of $0.70\,\mu$m (Lot: SiO_2-COOH-F-SC143-10ml). We selected silica because of its high density, which ensures that these small particles do not quickly diffuse out of the focal plane. The size of these particles was chosen as a compromise as they need to be small enough to not disturb the flow field, yet large enough to make tracking feasible.

We applied an electric field with an amplitude of $16.75\,\mathrm{mV}/\mu$m and a frequency of $750\,$Hz. This frequency was higher than in our usual experiments as we were imaging the microswimmer and tracer particles at a higher magnification, where electrophoretic oscillations were visible at $f = 250\,$Hz. Our samples were prepared similarly to our buffer screening experiments, with the washing protocol for the tracer particles mirroring that of our DNA-modified colloids, substituting buffer with water in all washing steps.

During the recording process, we manually adjusted the microscopy stage in sync with the migrating microswimmer to maintain it within our field of view. Due to the imperfect manual position adjustment, we employed an ImageJ plugin, Template Matching and Slice Alignment [85], to obtain microscopy videos with a stationary microswimmer and moving tracer particles. The resulting videos are provided in the Supplementary Movie files 3 and 4 [92].

In Figure 4.13a and Figure 4.13b, we visualized the trajectories of tracer particles for the forward and backward migrating microswimmer, respectively. For this purpose, we selected segments of the recorded video that contained at most two tracer particles passing

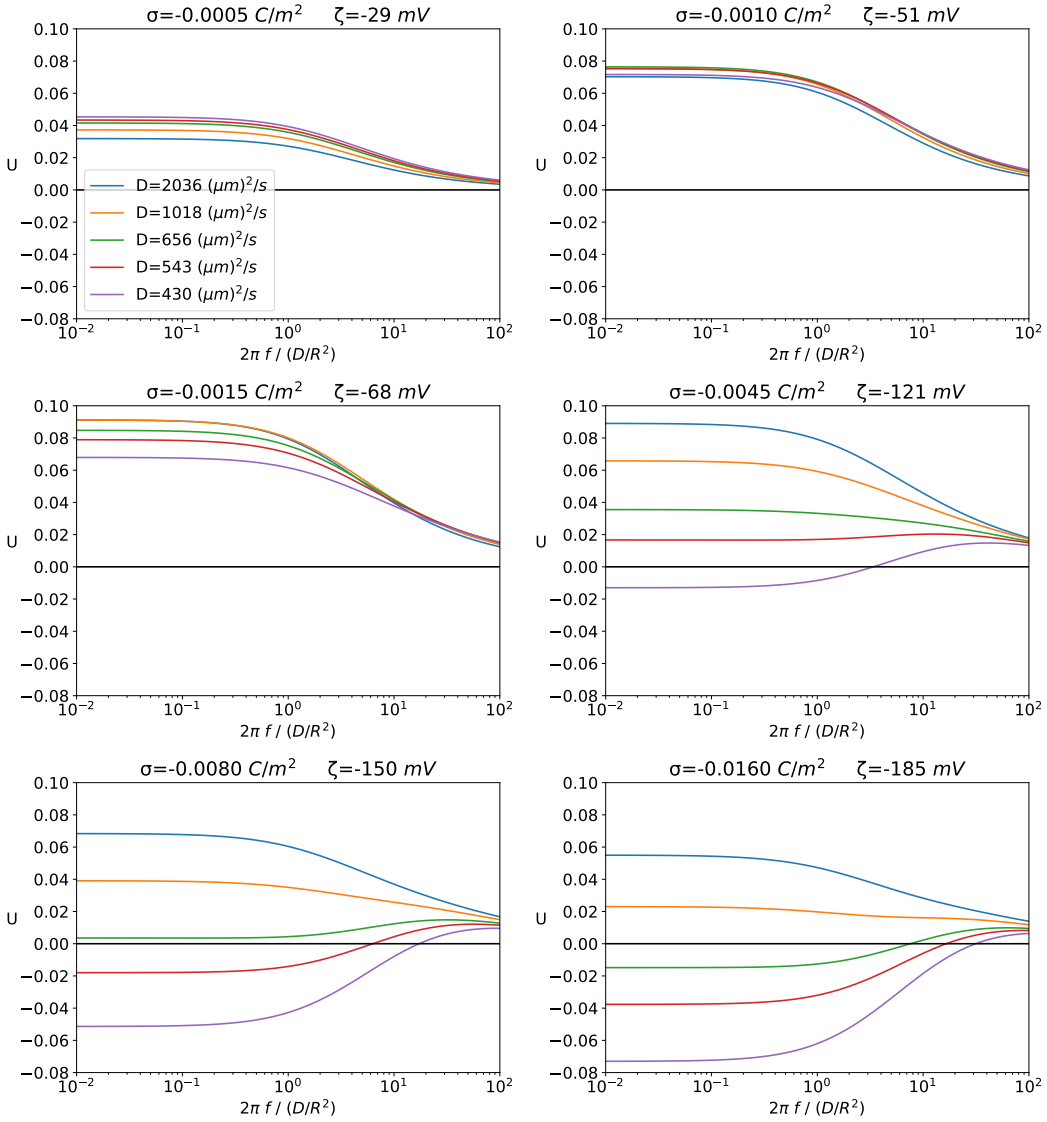

Figure 4.12. Plots of the frequency response of the dimensionless flow magnitude for CPEO flows around spheres with different surface charges σ and diffusion constants D. The Debye length is set to $\lambda = 43\,\text{nm}$ and the particle radius is $R = 0.78\,\mu\text{m}$

by the microswimmer. From the individual frames F_i of the selected video segments, we computed $G_i = \left|F_i - \overline{F}\right|$ where $\overline{F}$ is the average image of the F_i. In the images G_i, particles appear as bright spots, independent of their appearance in the images F_i where

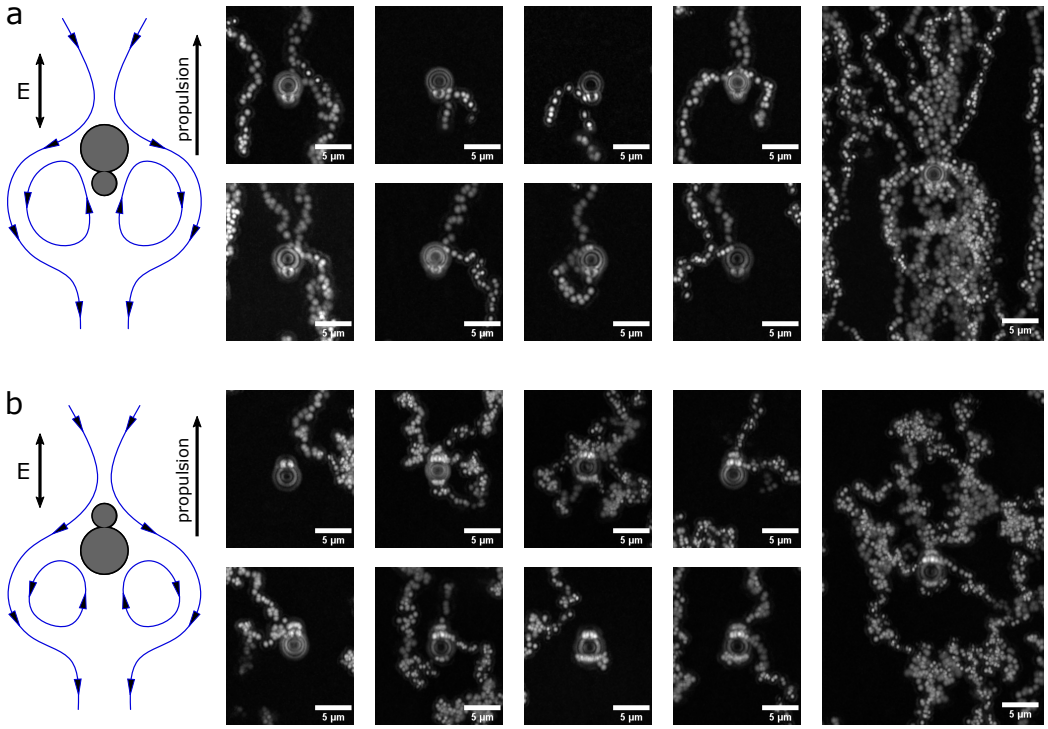

Figure 4.13. Overlay images showing particle traces of silica spheres, drifting in the flow field created by the microswimmer. Part (a) of the figure displays a forward-moving microswimmer with the larger particle located in the front, and part (b) displays a backward-moving microswimmer. The electric field oscillates in the vertical direction. The sketches on the left depict the streamlines of the deduced hydrodynamic flow, wherein the tracer particles drift. The smaller images in the center display short overlays involving one or two tracer particles, whereas the larger images on the right show an overlay from a longer video, capturing a larger number of tracer particles. The videos are provided in the Supplementary Movie files 3 and 4 [92].

they can appear either bright or dark depending on their position relative to the focal plane.

We then created an overlay image by extracting the maximum value of each pixel in the image sequence from the images G_i. The overlay images for both migration directions are shown on the right side of Figure 4.13. On the left side of Figure 4.13, we have sketched the flow field in which the tracer particles drift that can be deduced from the images. On the right, there is an overlay image of a longer video segment containing many tracer particles.

For the forward moving microswimmers in Figure 4.13a, particles approach the microswimmer from the front and move towards the center of the larger particle. They are then expelled perpendicularly to the migration direction of the microswimmer. Occasionally, a particle is trapped behind the microswimmer, where it circulates in the flow field. These trajectories are representative of the fluid flow in Figure 4.2. Importantly, it should be

noted that hydrodynamics is not the only factor influencing the movement of the tracer particles. Induced dipole-dipole forces also contribute to the interactions between the microswimmer and the tracer particles.
or the backward moving microswimmers in Figure 4.13b, the trajectories are less clear as the overall flow magnitudes are found to be lower. The trajectories appear more diffuse since the Brownian motion of the tracer particles dominates over their drift in the microswimmer's flow field. Despite this, tracer particles are observed to approach the microswimmer from the front, now represented by the smaller particle. They are attracted to the center of the smaller particle and then expelled perpendicular to the microswimmer's migration direction. Occasionally, a particle that has already passed by the microswimmer is attracted to its rear, i.e., the larger particle of the microswimmer. The tracer particle then becomes attached to the larger particle, which we attribute to induced dipole-dipole forces. We hypothesize that the induced dipole-dipole forces are stronger compared to the hydrodynamic flow in this scenario, preventing the circulation that is observed for the forward-moving microswimmer. Nonetheless, we surmise that the flow field still corresponds to the sketch on the left of Figure 4.13b.
We conclude that the flow field, is curved differently for backward-migrating microswimmers compared to forward-migrating microswimmers, and it is not simply inverted.

4.6.5 Monomer Mobility

To further investigate whether the inversion of migration direction is associated with the DNA functionalization of the colloids, we measured the mobility of the $1.0\,\mu$m-sized silica particles, both with and without DNA modification, using electrophoretic light scattering. Using a Malvern Zetasizer Nano ZS with a Dip-Cell accessory, we tested our samples in a single-use cuvette (Einmalküvetten ROTILABO® PMMA, Macro, 4 ml) from Carl Roth. We assessed the monomer mobility under buffer conditions that induced both forward and backward microswimmer migration. As we were interested specifically in the effect of small quantities of $MgCl_2$ ($5\,\mu$M), we carefully implemented several washing steps to avoid salt contamination. To this end, the unmodified $1.0\,\mu$m silica particles were diluted 1 to 5 in water resulting in concentrations comparable to those of our modified silica particles. The unmodified particles were washed following the same procedure as that used for the DNA-coated particles, but the borate buffer washing steps were omitted. For all measurements, we used the same cuvette, which was rinsed with deionized water between runs. The Dip-Cell was also rinsed between measurements. We marked one side of the cuvette to maintain the same orientation across all runs. Sample volumes of $1\,$mL were used, and colloids were diluted by a factor of 1 to 1000, i.e., we used $1\,\mu$L of our stock solution. The buffer was mixed directly in the cuvette for each measurement. We conducted four measurements, with 30 runs for each pipetted sample at a temperature of $25\,^{\circ}$C. The corresponding measurement files and raw data are provided as a Source Data

file. [92] To mitigate systematic errors, we pipetted each sample for each buffer condition three times, resulting in a total of 12 values for the monomer mobility under each buffer condition. We computed averages and standard deviations from these, which are represented in Figure 4.14 as bar graphs and error bars for the different buffer conditions used ($25\,\mu$M and $50\,\mu$M of NaOH, both with and without $5\,\mu$M of $MgCl_2$, and also $MgCl_2$ alone at $5\,\mu$M).
We did not observe any significant variation between the mobility of DNA-functionalized and unmodified colloids within the computed standard deviations, suggesting a negligible impact of the DNA modification on the electrokinetic properties of the colloids, even though the mobility of the DNA-modified colloids is lower than the mobility of the unmodified colloids across all buffer conditions. Furthermore, we found that the presence of $5\,\mu$M of $MgCl_2$ significantly reduced the mobility compared to experiments performed at the same NaOH concentrations without $MgCl_2$. We estimated the surface charge of the monomers using the measured mobility values and the buffer conditions of our experiments. This analysis was undertaken to examine whether the presence of $MgCl_2$ only modifies the double layer structure through enhanced electrostatic screening, or whether it also changes the surface charge. The zeta potential ζ can be estimated from the mobility μ using the Smoluchowski equation: $\zeta = \mu \frac{\eta}{\varepsilon_w \varepsilon_0}$ Here, η represents the viscosity of the solution, while ε_w and ε_0 denote the relative permittivity of water and the vacuum permittivity, respectively. From the zeta potential, we computed the surface charge with the help of the Poisson-Boltzmann equation, which in the presence of four ion species is given by:

$$\varepsilon_w \varepsilon_0 \frac{d^2\Phi}{dx^2} = -\left[+e \cdot c_{\mathrm{NaOH}} \cdot e^{\frac{-e\zeta}{k_B T}} - e \cdot c_{\mathrm{NaOH}} \cdot e^{\frac{e\zeta}{k_B T}} + 2e \cdot c_{\mathrm{MgCl_2}} \cdot e^{\frac{-2e\zeta}{k_B T}} - 2e \cdot c_{\mathrm{MgCl_2}} \cdot e^{\frac{e\zeta}{k_B T}}\right] \quad (4.7)$$

Here, e is the elementary charge, k_B is the Boltzmann constant, and T is the absolute temperature of the solution. c_{NaOH} and $c_{\mathrm{MgCl_2}}$ represent the concentrations of NaOH and $MgCl_2$ in the solution, respectively. Similar to the two ion species case, we can derive a relation between the surface charge σ, the charge per unit area on the surface of the monomers, and the zeta potential ζ. By multiplying the Poisson-Boltzmann equation with $\frac{d\Phi}{dx}$, integrating the result, and applying the boundary conditions $\Phi(\infty) = 0$ and $\frac{d\Phi}{dx}(\infty) = 0$ and at the surface, $\Phi(0) = \zeta$ and $\frac{d\Phi}{dx}(0) = -\frac{\sigma}{\varepsilon_w \varepsilon_0}$, we obtain the following equation for σ:

$$\begin{aligned}
\sigma &= -\sqrt{2\varepsilon_w \varepsilon_0 k_B T \cdot Q} \\
Q &= c_{\mathrm{NaOH}} \left(e^{-e\zeta/k_B T} - 1\right) \\
&\quad + c_{\mathrm{NaOH}} \left(e^{e\zeta/k_B T} - 1\right) \\
&\quad + c_{\mathrm{MgCl_2}} \left(e^{-2e\zeta/k_B T} - 1\right) \\
&\quad + 2c_{\mathrm{MgCl_2}} \left(e^{e\zeta/k_B T} - 1\right)
\end{aligned}$$

Based on this equation, we computed the surface charge from the measured mobilities for our experimental buffer conditions. We also accounted for the standard deviation of the zeta potentials, $\delta\zeta$, by using error propagation $\delta\sigma = \left|\frac{\partial\sigma}{\partial\zeta}\right| \cdot \delta\zeta$, which allowed us to determine the standard deviation of the surface charge, $\delta\sigma$.

The results are shown as a bar graph in Figure 4.15, indicating that the surface charge remains the same for identical NaOH concentrations regardless of the addition of 5 µM of $MgCl_2$. Moreover, we observed an increase in surface charge as the NaOH concentration increased. This trend is expected, as higher NaOH concentrations result in a greater degree of deprotonation of the carboxyl groups on the colloidal surface. Given the pronounced effect of even minor quantities of divalent magnesium ions on the mobility, we surmise that a detailed mathematical treatment of the dimensionless flow velocity in the context of mixed electrolytes, including divalent ions, could provide better insight into the observed reversal of migration direction.

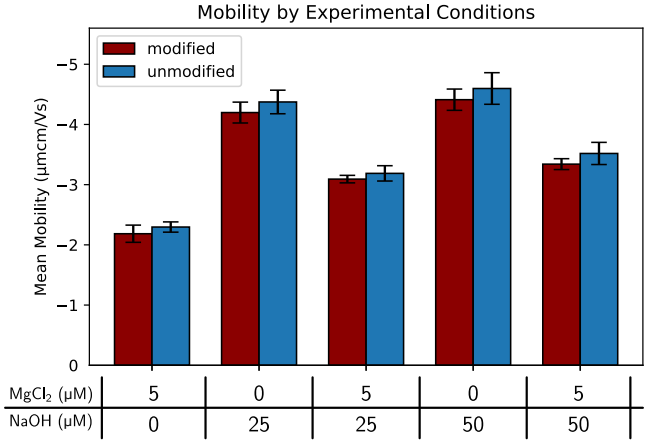

Figure 4.14. Bar graphs of the average monomer mobility from four measurements at each buffer condition. The error bars indicate the standard deviation. The buffer conditions are listed in the table below. Mobilities of DNA-modified and unmodified colloids are plotted next to each other in red and blue, respectively. No significant difference was observed between the mobility of DNA-modified and unmodified colloids across all buffer conditions. Source data are provided as a Source Data file. [92]

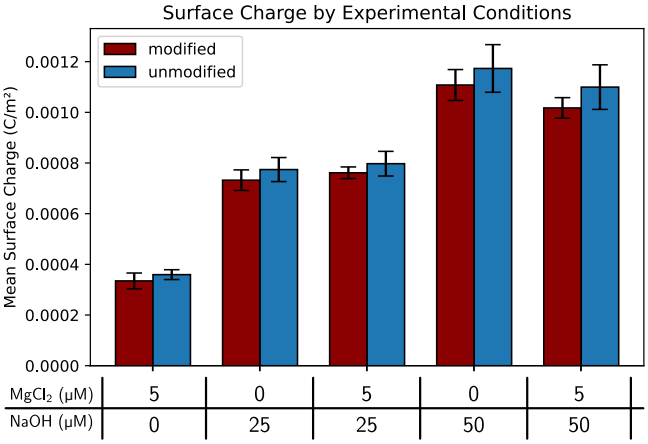

Figure 4.15. Bar graphs depicting the surface charge of monomers calculated from the average monomer mobility at each buffer conditions. The error bars are derived from the standard deviation of the mobilities via error propagation. The surface charges of DNA-modified and unmodified colloids are plotted next to each other in red and blue, respectively. The surface charge increases with higher concentrations of NaOH and is unaffected by the presence of $MgCl_2$.

5. Non-Equilibrium Assembly of Nucleic Acids in a Diffusiophoretic Trap

The text and figures in this chapter have been adapted from the publication stated below, which, at the time of writing this thesis, was under review. The videos mentioned below are presumably accessible on the publisher's webpage.

Non-Equilibrium Assembly of Nucleic Acids in a Diffusiophoretic Trap

Florian Katzmeier and Friedrich C. Simmel,
Department of Bioscience, TUM School of Natural Sciences, Technical University Munich,
D-85748 Garching, Germany

In this chapter, Friedrich C. Simmel and I conceptualized an electrically-driven upconcentration mechanism, which could occur in a natural environment, contrasting with the AC-electrically driven mechanism discussed in Chapter 3. This is particularly interesting for origin-of-life research, as it addresses the well-known concentration problem, referring to the challenge of achieving sufficiently high concentrations of reactants for reactions in primordial scenarios. [131] Specifically, I conceptualized and constructed a diffusiophoretic trap to facilitate local upconcentration and the hybridization and assembly of nucleic acids. The diffusiophoretic trap consists of a glass pipette filled with a highly concentrated electrolyte, whose components have asymmetric diffusion constants, as shown in Figure 5.1. When the electrolyte is ejected by applying pressure to the glass pipette into a low ionic strength liquid, a steep concentration gradient forms. The differential diffusion of the ions creates an electric field that can attract and concentrate nucleic acids. I characterized this mechanism by testing different pressures and consequently varying eflux rates, identifying an optimal pressure range. Further, I validated that the trap can upconcentrate silica particles as well and demonstrated that hybridization reactions on the particles' surfaces can be triggered when both DNA-modified silica particles and complementary DNA are upconcentrated. Lastly, I operated the trap with DNA nanostars, which are three-armed DNA nanostructures that can bind to each other and assemble into macroscopic gels. I observed that when the trap is active, DNA nanostars polymerize in front of the glass

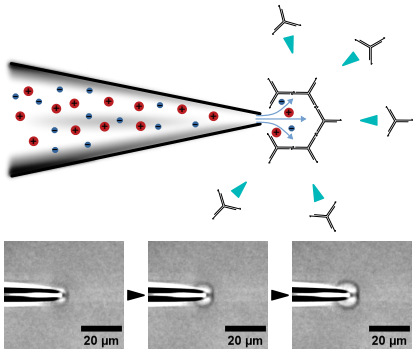

Figure 5.1. Overview Figure: Non-Equilibrium Assembly of Nucleic Acids in a Diffusiophoretic Trap. (Upper part) Sketch of the Diffusiophoretic Trap, comprising a glass pipette that ejects an electrolyte with asymmetric diffusion constants. The ejected ions generate an electric field that attracts and upconcentrates DNA nanostars, leading to their assembly into a gel. (Lower part) Microscopy images displaying the assembly of a DNA nanostar gel in front of the glass pipette.

pipette, forming a macroscopic gel, as illustrated in Figure 5.1. When the trap is deactivated, the gel disassembles. We propose that this system resembles a simple form of a biological system responding to an external stimulus.

5.1 Introduction

Living organisms operate far from equilibrium, continuously dissipating energy and exchanging matter with their surroundings to maintain their complex organization and structure. Numerous cellular processes such as microtubule and actin polymerization, RNA and protein metabo-lism, ribosome assembly, and chromosome condensation, are examples of dissipative self-assembly [132]. In these systems, local order is achieved by consuming an energy source, typically a chemical fuel, which allows organisms to exert temporal control over function. [133] Given the fundamental non-equilibrium state of biological processes, physical non-equi-librium settings such as thermal gradients [134–136], high-energy radiation [137, 138], wet-dry cycles [139–143], freeze-thaw cycles [144–146] as well as pH [147, 148] and concentration [149] gradients, have been extensively studied as plausible scenarios for promoting the emergence of life. [131] In this work, we introduce a model system for dissipative self-assembly that employs an electrolyte gradient as the energy source, complementing the chemical energy sources employed in other synthetic systems [150–158] that mimic biological systems. Specifically, we use the electrolyte gradient to achieve local up-concentration of branched DNA nanostructures [159–167], which then locally self-assemble into gels and subsequently disassemble upon the removal of the energy source.

Local up-concentration is achieved through diffusiophoresis [40], which refers to the directed migration of macromolecules or colloids in a concentration gradient. This mechanism has recently been the focus of intense research [168–178] and has been used to concentrate colloids [147,179–181] and macromolecules [182–184] in various experimental settings. In the case of electrolyte gradients, the primary driving force for diffusiophoresis is an electric field generated by the gradient itself. This electric field points along the gradient and acts on charged macromolecules like DNA through electrophoresis. Notably, the existence of such an electric field caused by an electrolyte gradient was theoretically described by Planck over a century ago. [47] Mechanistically, the electric field arises from an asymmetry in the diffusion coefficients of the ions that constitute the electrolyte. For instance, anions with higher diffusion coefficients than cations will diffuse down the concentration gradient more rapidly. Such differential diffusion results in charge separation, generating an electric field with more negative charges at the lower end of the gradient and more positive charges at the upper end. In electrochemical experiments, the potential drop associated with this electric field is referred to as the liquid junction potential. [185]

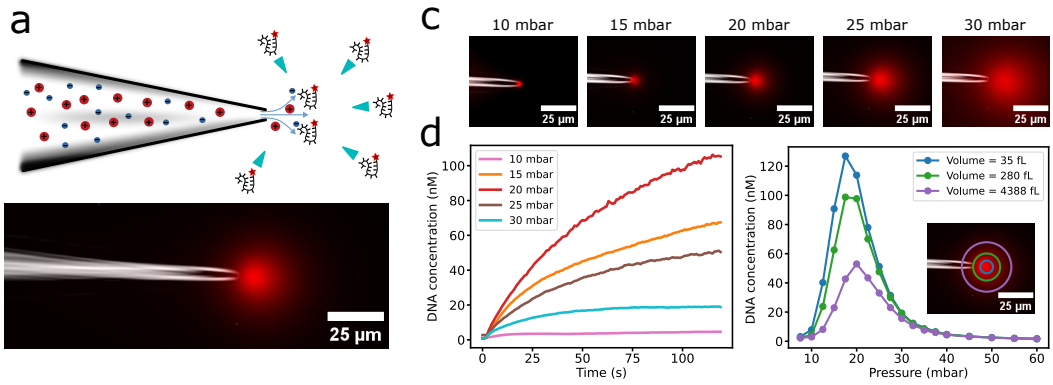

Figure 5.2. (a) Schematic representation of our experimental setup. A highly concentrated electrolyte, depicted with differently sized red and blue spheres to indicate ions with asymmetric diffusion constants, is ejected from a glass pipette to form an electrolyte gradient. Fluorescently labeled DNA strands are attracted through diffusiophoresis along the gradient towards the tip and accumulate there. The blue pointers indicate the direction of the diffusiophoretic force. (b) Overlay of an inverted brightfield image and a fluorescence image of the diffusiophoretic trap under operation. (c) Images of the diffusiophoretic trap $100\,\mathrm{s}$ after activation at different applied pressures. The brightness was individually adjusted in each image to ensure consistent visualization. (d) Left: Example time traces of the DNA concentration in a circular region of interest (ROI) around the trap, corresponding to a volume of approximately $280\,\mathrm{fL}$. Right: DNA concentrations within the trap after $100\,\mathrm{s}$ for different pipette pressures, measured in the ROIs indicated in the inset.

5.2 Results

As schematically shown in Figure 5.2a, a diffusiophoretic trap can be easily realized by filling a glass pipette with a highly concentrated electrolyte and submerging it in deionized water. The glass pipette is fixated in a commercially available pipette holder and is connected to a constant pressure supply via tubing. Upon application of a slight positive pressure on the pipette, the electrolyte flows out of the pipette tip, creating a steep electrolyte gradient near the orifice. When DNA molecules are present in the surrounding solution, they undergo directed migration towards the tip via diffusiophoresis. Close to the tip, the hydrodynamic force generated by the outflowing fluid exceeds the diffusiophoretic force, preventing DNA from entering the tip. As a result, DNA accumulates in a region in front of the tip where fluid flow and diffusiophoresis are balanced. In our experiments, we require an electric field such that negatively charged DNA migrates upwards along the electrolyte gradient toward the pipette tip. The electric field $\boldsymbol{E}$ in a two-component electrolyte gradient depends on the cation and anion diffusion coefficients D^+ and D^-, and their respective valencies z^+ and z^-: [169, 186, 187]

$$\boldsymbol{E} \propto \frac{D^+ - D^-}{|z^+|\, D^+ + |z^-|\, D^-} \frac{\boldsymbol{\nabla} c}{c} \tag{5.1}$$

Here, $\frac{\boldsymbol{\nabla} c}{c}$ represents the normalized gradient of the electrolyte concentration c. An instructive derivation of this equation, along with an evolution equation for c, is given in Section 5.5.2. Equation 5.1 guides our selection of suitable electrolytes for diffusiophoretic trapping. As the direction of the electric field is determined by the difference of the diffusion coefficients $(D^+ - D^-)$, independent of ion valency, we require $D^+ < D^-$ for DNA trapping. Additionally, low-valency ions yield stronger electric fields, as z^+ and z^- only appear in the denominator. In our experiments, we use $200\,\mathrm{mM}$ Tris, titrated with HCl to pH 7.7, which primarily contains monovalent TrisH^+ ions with $D^+ = 0.8 \times 10^{-9}\,\mathrm{m^2\,s^{-1}}$ [114] and Cl^- ions with $D^- = 2.0 \times 10^{-9}\,\mathrm{m^2\,s^{-1}}$ at $T = 298\ \mathrm{K}$. We also supplement the solution with $1\,\mathrm{mM}$ $\mathrm{MgCl_2}$ to facilitate nucleic acid hybridization. Importantly, the diffusion coefficient of Mg^{2+} is $0.7 \times 10^{-9}\,\mathrm{m^2\,s^{-1}}$ [185], which also satisfies our criterion when compared to the diffusion coefficient of Cl^-. We hypothesize that combinations of such electrolytes should also be effective.

5.2.1 Trapping Efficiency

In initial experiments, we characterized the trap with 33 nucleotide (nt) long single-stranded DNA molecules ($c = 1\,\text{nM}$) modified with a fluorescent dye. Figure 5.2b displays the trap $100\,\text{s}$ after activation, showing a diffuse cloud of fluorescent DNA in front of the pipette tip. The fluorescent cloud forms directly after activation of the trap and grows in intensity until it reaches a steady state. We observed variations in the shape and intensity of the DNA cloud depending on the applied pipette pressure, as illustrated in Figure 5.2c. Low pressures lead to a more localized DNA accumulation, while high pressures result in a larger, more diffuse cloud. These variations in the extension of the accumulation region are not unexpected: higher pressures result in higher electrolyte efflux rates, altering the shape of the concentration gradient, and DNA accumulates in a region where the diffusiophoretic force balances the fluid flow, which changes depending on both the flow magnitude and the gradient shape.

We recorded microscopy videos to quantify the formation and growth of the trapped DNA cloud at varying pipette pressures. For data analysis, we defined a circular region of interest (ROI) around the cloud and measured its average fluorescence. The ROI is identified by finding the maximum intensity among all possible circular regions of the same size within an image. We then compared the region's average fluorescence to bulk fluorescence values for the same DNA strands at different concentrations, which allowed us to estimate the local DNA concentration within the trap. Figure 5.2d (left) displays example time traces which show the change in DNA concentration within a circular ROI with a volume of $\approx 280\,\text{fL}$. We observe up to a 100-fold increase in concentration within the trap, raising the DNA concentration from its bulk value of $1\,\text{nM}$ to $100\,\text{nM}$. Further, we find that the concentration reaches a steady state after approximately $100\,\text{s}$. Notably, a pressure difference of $20\,\text{mbar}$ results in more efficient up-concentration compared to lower (e.g., $10\,\text{mbar}$, $15\,\text{mbar}$) or higher (e.g., $25\,\text{mbar}$, $30\,\text{mbar}$) pipette pressures, suggesting an optimal pressure condition.

We further quantified DNA trapping by measuring the DNA concentration within three differently sized ROIs after $100\,\text{s}$. The resulting data, showing DNA concentration as a function of pressure, are displayed in Figure 5.2d (right). For all three regions, we observe a peak trapping efficiency around $20\,\text{mbar}$. Additionally, we identify a minimum operational pressure difference of $10\,\text{mbar}$ at which the trap becomes effective. At pressures exceeding $30\,\text{mbar}$, trapping efficiency becomes comparably low. Notably, the concentration peak shifts to slightly lower pressures for smaller regions of interest, consistent with our previous observation that lower pressures result in more localized DNA clouds.

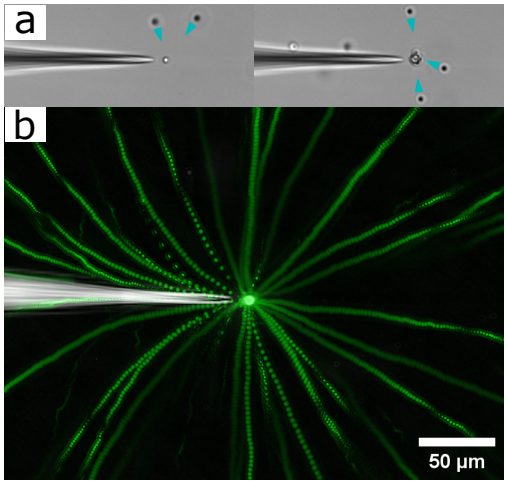

Figure 5.3. (a) Microscopy images showing the trap operating in the presence of colloidal particles ($d = 2.1\mu$m). The microparticles accumulate in front of the tip, their direction of movement is indicated with blue pointers. (b) Overlay image from a video (Supporting video 1) that captures the attraction and accumulation of the microparticles. Particle traces are represented as green lines.

5.2.2 Range of the Trap

To visualize the range of the diffusiophoretic force generated by the trap, we used carboxylated silica particles ($d = 2.1\,\mu$m), which carry a negative charge and are therefore expected to migrate in the same direction as DNA in the trapping field. Operating the trap at $25\,$mbar, we observed accumulation of colloids in a region directly in front of the trap, as shown in Figure 5.3a. We also recorded a microscopy video of the colloid trapping process (Supporting video 1), from which we generated an overlay image of the particle traces (Figure 5.3b) (details on video analysis are given in Section 5.5.5). Our observations suggest that the diffusiophoretic trapping force is long-range, extending over hundreds of micrometers. This may seem surprising, as electric forces in electrolytes typically have a range defined by the Debye length, i.e., usually on the order of nanometers. However, in non-equilibrium scenarios, such as when a current is applied or, as in our case, when a concentration gradient is present, the electric force can extend over a much longer range. It is worth noting that, according to Equation 5.1, the range of the diffusiophoretic force should in fact be similar to that of the concentration gradient.

Next, we investigated the diffusiophoretic trap's capacity to promote DNA hybridization reactions. Notably, the trap generates favorable conditions for such reactions in two respects: the trap locally enhances the DNA concentration by hundredfold, and the steep electrolyte gradient provides a high ionic strength within the trap. By contrast, in regions

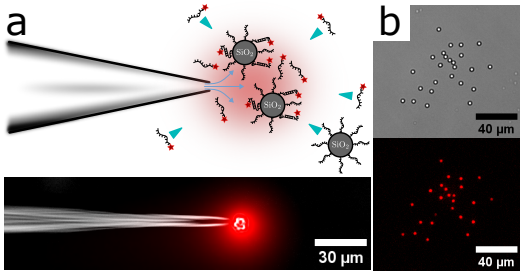

Figure 5.4. (a) DNA-modified silica particles and complementary strands are both accumulated in the diffusiophoretic trap. The locally high DNA and electrolyte concentrations promote DNA hybridization on the colloid surface. The blue pointers indicate the direction of the diffusiophoretic force. (b) Brightfield and fluorescence images of the sedimented particles after the trap was turned off (see also Supporting video 2).

remote from the trap, both DNA and electrolyte concentrations are low, preventing DNA hybridization to occur.

5.2.3 DNA Hybridization on Silica Particles

Since both carboxylated silica particles and DNA accumulate in the trap, we studied hybridization reactions on the surface of the colloids, which can be easily monitored by microscopy. We modified the microparticles by activating their carboxyl groups with 1-Ethyl-3-(3-dimethyl-aminopropyl) carbodiimide (EDC) and coupling them to 60 nt long amino-modified DNA capture strands. [124, 125] We then operated the trap at $25\,\mathrm{mbar}$ using the DNA-modified colloids and a $5\,\mathrm{nM}$ solution of fluorescently labeled 30 nt long DNA strands, which had a sequence complementary to a subsequence of the DNA on the colloids (cf. Section 5.5.8). Both colloids and free DNA accumulate in the trap, allowing the free DNA to hybridize with the DNA on the colloids (Figure 5.4a.). After $5\,\mathrm{min}$ of operation we turned off the trap and the colloids sedimented. The localization of fluorescence signal on the microparticles, which is visible in the fluorescence image of the sedimented colloids (Figure 5.4b), indicates successful DNA hybridization. We observed fluorescence on the particles for an additional $2\,\mathrm{h}$, indicating that the fluorescent DNA was indeed stably bound to the capture strands. The complete experiment is documented in Supporting video 2.

5.2.4 Formation of DNA Gels

Lastly, we studied whether the diffusiophoretic trap can promote the assembly of branched DNA junctions - also termed Y-DNA [159,160,164] or DNA nanostars [161–163,165–167]

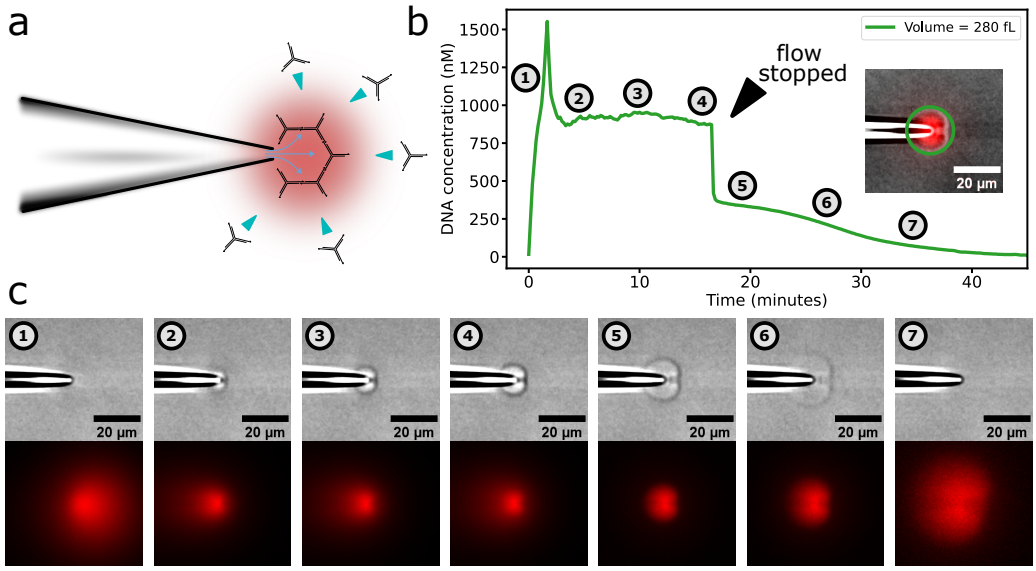

Figure 5.5. (a) Sketch illustrating how DNA nanostars are attracted and accumulate in a diffusiophoretic trap. The nanostars have self-complementary single-stranded overhangs that allow them to polymerize into a gel. (b) DNA concentration within a circular ROI close to the tip's pore during a DNA nanostar polymerization experiment. The ROI is shown in the microscopy image in the inset, numbers on the graph correspond to the images displayed in (c). (c) Brightfield and fluorescence images from selected frames of the nanostar polymerization experiment. The fluorescence intensity was individually adjusted for each frame.

- into macroscopic gels (cf. Figure 5.5a). Three-arm DNA nanostars are composed of three 42 nt long single strands that hybridize together to form a Y-shaped nanostructure with three ≈ 7 nm long arms. Each arm of a nanostar features a single-stranded sticky end with a distinct self-complementary sequence, enabling the edges of the junctions to bind to each other and polymerize into a gel. We operated the diffusiophoretic trap with $5\,$nM DNA complexes. In order to be able to monitor their assembly via fluorescence microscopy, we substituted $1\,$nM of one of their constituent strands with a 33 nt long strand carrying a Cy5-label instead of the sticky end.

In Figure 5.5c, we show selected frames extracted from a microscopy video (Supporting video 3) of the trap operating in the presence of nanostars. The video is further analyzed by plotting the fluorescence intensity within a circular region of interest as indicated in Figure 5.5b. Within roughly the first minute of operation (until time point 1), the fluorescence rapidly increases, corresponding to the formation of a diffuse DNA cloud similar as in the experiments shown in Figure 5.2. Between time points 1 and 2, the shape of the fluorescent cloud changes and its intensity drops. Simultaneously, in the brightfield image a distinct structure appears in front of the tip, which we interpret as the formation of a DNA gel. The change in shape of the fluorescent cloud is likely due to the altered hydrodynamic flow and electrolyte gradient caused by the presence of the DNA gel. The gel continues to grow in size between time points 2 and 4, while maintaining a relatively constant fluorescence level. After 17 minutes (between time points 4 and 5), we stopped the electrolyte flow, eliminating the gradient and thus terminating the trapping process. We observed a quick initial expansion in the size of the gel, accompanied by a rapid decrease in fluorescence. The gel continues to expand until it is no longer visible in either the fluorescence or brightfield channels. We repeated the DNA gel formation experiment multiple times and found similar behavior as in Figure 5.5b in each case (see Section 5.5.7).

5.3 Discussion

The observed behavior can be explained with the viscoelastic properties of DNA nanostar gels [161, 163, 164]. The rapid expansion of the gel following trap deactivation is a consequence of the elasticity of the DNA gel. During operation of the trap, the gel is compressed by the force exerted through the electric field. Upon removal of this force, the gel quickly relaxes and expands. The swift decrease in fluorescence after time point 4 can be attributed to the diffusion of unbound DNA molecules out of the trap. The later phase of the dissolution process (time points 6 and 7) is characterized by a slow

expansion of the gel and fading visibility, indicating swelling and bulk erosion. As the gel forms under a compressive force and at high DNA concentrations, it initially comprises a densely interconnected matrix. During dissolution, nanostars dissociate within the gel and either escape or bind elsewhere. This results in a reduced crosslinking density, leading to elastic relaxation and expansion of the gel matrix.

5.4 Conclusion

In conclusion, we have developed a diffusiophoretic trap capable of locally concentrating both DNA and colloids, as well as promoting hybridization between complementary DNA strands. Moreover, we investigated the reversible self-assembly of DNA nanostars into macroscopic structures. DNA nanostars assemble in the presence of an electrolyte gradient, and disassemble when this gradient is removed. An electric field generated by the gradient provides the driving force for assembly by locally up-concentrating the DNA. When the energy source is removed, the gel slowly disassembles, demonstrating that the DNA gel only exists under non-equilibrium conditions.

In addition to its fundamental scientific interest as a non-equilibrium dynamical system, the diffusiophoretic trap has potential technological applications. Our experiments demonstrate that the trap can be employed to up-concentrate charged colloids or molecules, which could be used for extracting them from diluted environmental samples, or for selecting and sorting particles based on charge. Furthermore, the local up-concentration mechanism provides a possibility to speed up concentration-dependent reactions, which might prove useful for the development of low cost DNA or RNA detection systems.

Due to its simplicity - only requiring a sufficiently steep salt gradient - our trap system is also of interest as a potential setting for prebiotic evolution, specifically relating to the well-known concentration problem. Given the dilute nature of primordial environments, prebiotic evolution faces the challenge of achieving the necessary concentration of organic molecules to undergo reactions that would lead to the formation of the first biomolecules. [131] Diffusiophoresis in salt gradients provides an additional mechanism besides other natural phenomena like thermal gradients [134–136], freeze-thaw cycles [144–146], and evaporation [139–143], which can up-concentrate (bio)molecules. Natural sources of electrolyte gradients may include porous rocks that leach salts, salt-water springs, or hydrothermal vents. According to Equation 5.1, salts suitable for the diffusiophoretic trapping of nucleic acids comprise most halogen salts of divalent or trivalent metal ions [185]. Alkaline solutions are also expected to be effective, due to the exceptionally high diffusion constant of OH^-. Notably, calcium carbonate, a commonly

occurring mineral, has previously been demonstrated to be effective in driving diffusiophoresis [169].

5.5 Materials and Methods

5.5.1 Design and Operation of the Setup

Figure 5.6 shows the setup of our diffusiophoretic trap. We constructed a custom-built mechanical micromanipulator mounted on a microscopy stage. The glass pipette holder is mounted on a lever that has an adjustable angle. We use a BNC-Type Pipette Holder (HEKA; #895229) for glass pipettes with an outer diameter of 1.5 mm. For microscopy, we employed an Olympus IX81 inverted microscope equipped with a $20\times$ objective (Olympus UPlanFL N $20 \times /0.50$). The microscope is placed on an optical table and inside a plastic housing to prevent air flow and vibrations from disturbing our experiments. Adjustable air pressure is provided to the glass pipette by an OB1 MK3 microfluidic flow controller from Elveflow.

The sample chamber is a standard 8 mm x 1 mm nitrile rubber sealing ring glued to a glass cover slide (ROTH; #CEX2.1). To fixate the sealing ring, we first dipped it into a drop of UV-curable glue (BEST KLEBSTOFFE; Uvirapid 702). Excess glue is removed by placing the sealing ring on another glass slide and picking it up again. The sealing ring is then carefully placed in the center of the glass slide. The glue is cured by shining UV light on the glass slide for 1 h. The sample chamber is rinsed with deionized water, sonicated in a 2 % Hellmanex (Hellma; #9-307-011-4-507) bath for 15 min, rinsed again with deionized water, and then sonicated again in deionized water for 15 min. The sample chamber is then carefully dried using compressed air. We store the sample chambers in an empty pipette box. We avoid storing the sample chambers in water as we found this causes the sealing ring to detach from the glass slide.

For pulling glass pipettes, we use a P-1000 pipette puller from Sutter Instruments equipped with a 2.5 mm x 2.5 mm box heating filament (Sutter Instrument, #FB255B) from Science Products GmbH. We use borosilicate glass capillaries (Sutter Instrument; #BF150-86-10) with an outer diameter of 1.5 mm and an inner diameter of 0.86 mm. The pulling settings to produce sub-micrometer pipette tip orifices are as follows: Heat $=$ 547, Pull $=$ 3, Velocity $=$ 37, Delay $=$ 1, Pressure $=$ 500. [188]

For our experiments, we use 200 mM Tris (ROTH; #4855.2) titrated with HCl (ROTH; #0281.1) to a pH of 7.7 and supplement it with 1 mM $MgCl_2$ (Merck; #63069-500ML).

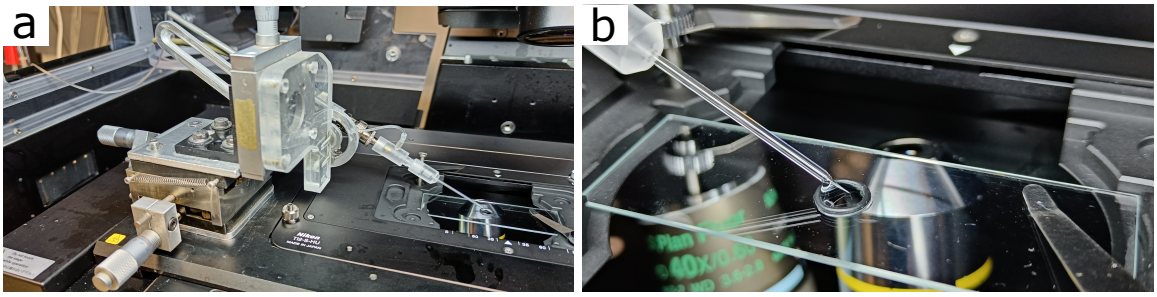

Figure 5.6. (a) Photograph of our diffusiophoretic trap setup, showing a glass pipette mounted on a mechanical micromanipulator. A pressure supply is connected via small tubing. (b) Close-up photograph of the glass pipette extending into the sample chamber, which is filled with water. The sample chamber consists of a sealing ring glued to a microscopy slide.

We prepare our samples in $1.5\,\mathrm{mL}$ tubes (Eppendorf; Safe-Lock Tubes 1.5mL). We note that all tubes contain dust particles, which are attracted to our trap and lead to inconsistent experiments. To mitigate this issue, we pre-wash the tubes with Helmanex and distilled water.

To prepare the sample chamber, we rinse it with deionized water, blow it dry, and position it on the microscopy stage. We fill a newly pulled glass pipette with buffer using specialized pipette tips (Eppendorf; Microloader) and insert the pipette into a holder on the mechanical micromanipulator. We add $30\,\mu\mathrm{L}$ of sample to the chamber, filling it gently to avoid bubble formation and to prevent dust particle contamination. We also ensure a flat water surface to prevent optical distortions. Finally, we lower the filled glass pipette into the sample chamber.

5.5.2 Theoretical Considerations

Calculation of the Electric Field

In this Section, we derive the electric field $\boldsymbol{E}$ that arises in a concentration gradient of a two-component electrolyte with ion valencies z^+ and z^- and local concentrations c^+ and c^-. When ions have dissimilar diffusion constants D^+ and D^-, one ion species diffuses more rapidly, leading to charge separation. This charge separation generates an electric field. We start by using the approach outlined by Chiang et al. [169], who derived an electric field expression for multi-component electrolytes.

The ion fluxes j^+ and j^- are governed by the Nernst-Planck equations, combined with a

convective drift term due to the fluid velocity $\boldsymbol{v}$:

$$\boldsymbol{j}^{+} = -D^{+}\boldsymbol{\nabla}c^{+} + D^{+}\left|z^{+}\right|\frac{e}{k_B T}c^{+}\boldsymbol{E} + c^{+}\boldsymbol{v} \tag{5.2}$$

$$\boldsymbol{j}^{-} = -D^{-}\boldsymbol{\nabla}c^{-} - D^{-}\left|z^{-}\right|\frac{e}{k_B T}c^{-}\boldsymbol{E} + c^{-}\boldsymbol{v} \tag{5.3}$$

Further, we must also consider the continuity equation for each ion species:

$$\frac{\partial c^{+}}{\partial t} + \nabla \cdot \boldsymbol{j}^{+} = 0 \tag{5.4}$$

$$\frac{\partial c^{-}}{\partial t} + \nabla \cdot \boldsymbol{j}^{-} = 0 \tag{5.5}$$

Additionally, we assume approximate electroneutrality in the system [189]:

$$0 = \left|z^{+}\right| c^{+} - \left|z^{-}\right| c^{-} \tag{5.6}$$

The electric current density J can be computed from the ion fluxes as $J = e\left|z^{+}\right|\boldsymbol{j}^{+} - e\left|z^{-}\right|\boldsymbol{j}^{-}$. We assume zero electric current as there are no external electrodes or other charge sources. This zero-current condition yields $\left|z^{+}\right|\boldsymbol{j}^{+} - \left|z^{-}\right|\boldsymbol{j}^{-} = 0$, which, upon using equations 5.2 and 5.3, results in

$$0 = \frac{J}{e} = -D^{+}\left|z^{+}\right|\boldsymbol{\nabla}c^{+} + D^{-}\left|z^{-}\right|\boldsymbol{\nabla}c^{-} + \left(D^{+}\left|z^{+}\right|^{2}\frac{e}{k_B T}c^{+} + D^{-}\left|z^{-}\right|^{2}\frac{e}{k_B T}c^{-}\right)\boldsymbol{E} + \left(\left|z^{+}\right|c^{+} - \left|z^{-}\right|c^{-}\right)\boldsymbol{v} \tag{5.7}$$

The convection term now includes the right side of equation 5.6 as a factor and thus vanishes. We then define $n = \left|z^{+}\right| c^{+} = \left|z^{-}\right| c^{-}$ in line with equation 5.6:

$$0 = \frac{J}{e} = -\left(D^{+} + D^{-}\right)\boldsymbol{\nabla}n + \frac{e}{k_B T}\left(D^{+}\left|z^{+}\right| + D^{-}\left|z^{-}\right|\right)n\boldsymbol{E} \tag{5.8}$$

Here, n represents the equivalent number of monovalent ions bearing the same charge as the multivalent ions. Solving for $\boldsymbol{E}$ gives the desired expression for the electric field:

$$\boldsymbol{E} = \frac{k_B T}{e}\frac{D^{+} - D^{-}}{\left|z^{+}\right| D^{+} + \left|z^{-}\right| D^{-}}\frac{\boldsymbol{\nabla}n}{n} \tag{5.9}$$

The gradient term is invariant under scaling, implying that $\frac{\boldsymbol{\nabla}n}{n} = \frac{\alpha\boldsymbol{\nabla}n}{\alpha n} = \frac{\boldsymbol{\nabla}c}{c}$. The scaling factor α can be chosen such that c corresponds to any definition of the local electrolyte concentration. For instance, setting $\alpha = \frac{1}{\left|z^{+}\right|}$ yields $c = \frac{1}{\left|z^{+}\right|}n = c^{+}$.

Equation for the Electrolyte Concentration

For completeness, we also derive the evolution equation for the electrolyte concentration c. To do this, we eliminate the electric field in equation 5.2 using equation 5.9. We employ the appropriate electrolyte concentration definition for the gradient term, which is $\frac{\boldsymbol{\nabla} c^+}{c^+}$:

$$\boldsymbol{j}^+ = -D^+ \boldsymbol{\nabla} c^+ + D^+ \left|z^+\right| c^+ \frac{D^+ - D^-}{\left|z^+\right| D^+ + \left|z^-\right| D^-} \frac{\boldsymbol{\nabla} c^+}{c^+} + c^+ \boldsymbol{v} \tag{5.10}$$

The equation can be further simplified and rearranged as:

$$\boldsymbol{j}^+ = -D^+ D^- \frac{\left|z^+\right| + \left|z^-\right|}{\left|z^+\right| D^+ + \left|z^-\right| D^-} \boldsymbol{\nabla} c^+ + c^+ \boldsymbol{v} \tag{5.11}$$

We define an effective diffusion constant $D^* = D^+ D^- \frac{\left|z^+\right| + \left|z^-\right|}{\left|z^+\right| D^+ + \left|z^-\right| D^-}$ and apply the continuity equation 5.4:

$$\frac{\partial c^+}{\partial t} = D^* \Delta c^+ - \nabla \left(c^+ \boldsymbol{v}\right) \tag{5.12}$$

Note that the procedure would yield the same result if initiated with equation 5.3, but with c^- appearing in the equation instead of c^+. Also, drift-diffusion equations are generally invariant under scaling, as the concentration term appears in every summand. We can thus replace c^+ with any ion concentration definition. For instance, we can use $n = c^+ \left|z^+\right|$ again.

5.5.3 Programming and Video Editing

For video and image analysis we used ImageJ [190]. The final video editing was done using the open-source software Shotcut [128]. The programming was assisted by ChatGPT [191] based on the large language model GPT-4 [192]. We use NUPACK for the design of DNA sequences [126].

5.5.4 Measurement of the Trapping Efficiency (Section 5.2.1)

Experimental Section

We prepare a $1\,\mathrm{mL}$ solution containing $1\,\mathrm{nM}$ of fluorescently labeled DNA in deionized water. Using this solution, we operate the diffusiophoretic trap and record microscopy videos to capture the formation of the fluorescent diffuse cloud at varying applied pressures. Between each run, we carefully replace the sample in the chamber. Each recorded video lasts $120\,\mathrm{s}$, with an image captured every $1\,\mathrm{s}$. To generate a calibration curve for data

analysis, we also image DNA solutions at concentrations of 0 nM, 1 nM, 5 nM, 25 nM, 50 nM, and 100 nM.
We record additional videos of the trapping process that include a brightfield channel at selected pressure values: 10 mbar, 15 mbar, 20 mbar, 25 mbar, and 30 mbar. These dual-channel videos enable us to visualize the shape of the fluorescent diffuse cloud in relation to the pipette.

Calibration and Image Correction

We aim to establish a calibration procedure to translate fluorescence values from microscopy images into DNA concentrations. To achieve this, we compute a translation factor and perform a flat-field correction to account for uneven illumination. For the flat-field correction, we need to generate a correction image.

A microscopy image with pixel intensity values $I(x, y)$ at pixel coordinates x and y under uneven illumination can be modeled as

$$I(x, y) = S(x, y) \cdot F(x, y) + B. \tag{5.13}$$

Here, B represents the background signal predominantly arising from the camera's internal noise, $F(x, y)$ denotes the uneven illumination pattern with a spatial average $\langle F(x, y)\rangle = 1$, and $S(x, y)$ is the signal representing image features. Rearranging equation (5.13), we obtain

$$S(x, y) = \frac{I(x, y) - B}{F(x, y)}. \tag{5.14}$$

We use an image with 0 nM DNA concentration, containing only deionized water, as our background image B. To compute the correction image $F(x, y)$, we consider images $I_c(x, y)$ of bulk DNA at concentrations c. Using equation (5.13), we have

$$I_c(x, y) = g(c) \cdot F(x, y) + B. \tag{5.15}$$

$g(c)$ is constant for a given image and depends on the DNA concentration. Solving for $F(x, y)$ yields

$$F(x, y) = \frac{I_c(x, y) - B}{g(c)}. \tag{5.16}$$

We can find an expression for $g(c)$ by averaging equation (5.16) and using $\langle F(x, y)\rangle = 1$:

$$g(c) = \langle I_c(x, y) - B\rangle \tag{5.17}$$

We can thus calculate the correction image as

$$F(x,y) = \frac{I_c(x,y) - B}{\langle I_c(x,y) - B \rangle}. \tag{5.18}$$

We averaged the correction images obtained for all DNA concentrations c to enhance accuracy. This averaged correction image is then applied using equation (5.14).

To translate fluorescence values into concentrations, we assume a linear relationship between concentration c and $g(c)$:

$$\langle I_c(x,y) - B \rangle = g(c) = k \cdot c \tag{5.19}$$

We fit $\langle I_c(x,y) - B \rangle$ to obtain k, as shown in Figure 5.7. We find $k = 90.1\,\mathrm{a\,u}\,/\mathrm{nM}$.

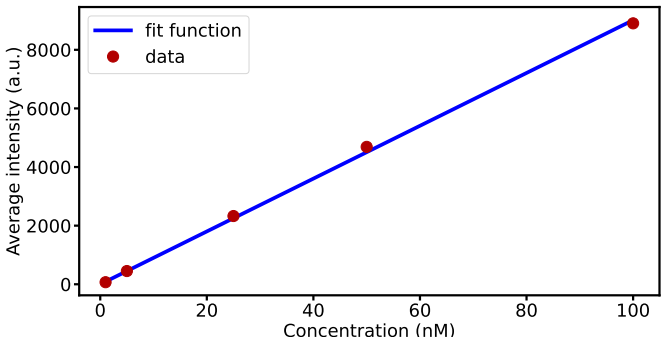

Figure 5.7. Plot of the average intensity of the bulk fluorescent values at different concentrations of fluorescent DNA. Data are fitted with a linear function.

Using this value, we can estimate local DNA concentrations $c(x,y)$ in the corrected images $S(x,y)$ as $c(x,y) = S(x,y)/k$.

Concentrations in the Trap

To assess the efficiency of the diffusiophoretic trap under various applied pressures, we aim to measure the DNA concentration in the trap. First, we apply the correction to the videos using equation (5.14). We define a circular region of interest around the diffusiophoretic trap where we aim to estimate the DNA concentration. We identify this region by locating the maximum intensity among all possible circular regions of the same size within an image. First, we create an image that contains the average values of the circular region around a specific pixel as the pixel value. Computationally, we achieve this

by defining a normalized circular filter $C(x, y)$. This filter depicts a bright circle on a black background, with the sum of all its pixel values equal to 1. We convolve each frame of our microscopy videos with this circular filter, as expressed by $S(x, y) * C(x, y)$. From the resulting image, we extract the maximum pixel value, denoted as $\max(S(x, y) * C(x, y))$. According to our definition, this maximum value represents the average fluorescence value inside the trap. Note that this procedure is effective only when a single bright spot is present in an image. We apply this procedure to every frame of all microscopy videos for three differently sized circular regions. This yields fluorescence-over-time data for each recorded video at a given pressure. By applying the conversion factor k, we translate fluorescence values into concentrations and generate the plots depicted in Figure 5.2

Image Editing

From the dual-channel videos that include both brightfield and fluorescence channels, we selected one frame from each channel 100 s after initiating each experiment. We then generated overlay images by combining the inverted brightfield frame with the corresponding fluorescence frame. To maintain uniformity, we adjusted the contrast in both the brightfield and fluorescence frames to get similar brightness levels for all images.

5.5.5 Operation of the Trap with Silica Spheres (Section 5.2.2)

Experimental Section

We purchased carboxylated silica spheres with a diameter of 2.12 µm (Lot: SiO2-COOH-AR1060-5ml) from microParticles GmbH. Before use, we washed the colloids in deionized water. To do this, we diluted the colloidal stock solution 1:10 in 1000 µL of deionized water. We then centrifuged the solution at 1000 rcf for 2 min and removed the supernatant. Next, we added 1000 µL of deionized water and sonicated the colloidal solution for 1 min using an ultrasound generator (Bandelin: SONOPLUS UW mini20) at maximum power. We repeated the procedure three times. For our experiments, we used a total dilution of 1:200,000 with respect to the initial stock concentration. Note that this value requires adjustment through trial and error, as the number of colloids lost during the washing procedure and the initial stock concentration may vary.
We operated our diffusiophoretic trap at 25 mBar and recorded a 3 min long brightfield video of colloids being attracted and accumulated in the trap.

Data Analysis and Video Editing

From the recorded video, we created the image shown in Figure 5.3, which displays the trajectories of the colloids as green lines. To generate this image, we first computed $G_i = |I_i - I|$ from the individual frames I_i, where I is the average image of these frames. In the computed images G_i, particles appear as bright spots. This is independent of their appearance in the original frames F_i, where they could appear either bright or dark depending on their position relative to the focal plane. Finally, we created an overlay image by taking the maximum value of each pixel across the image sequence from the images G_i. We then overlaid the resulting image with the inverted average image I such that the pipette is visible in the image.

5.5.6 DNA Hybridization on Silica Particles (Section 5.2.3)

Functionalization of Silica Particles

We modified the surface of our silica spheres by activating the carboxyl groups using 1-Ethyl-3-(3-dimethyl-aminopropyl) carbodiimide (EDC) and coupling them to amino-modified DNA [124, 125]. The protocol follows a methodology we previously developed [92]. The colloids reacted in $200\,\mu$L of $100\,$mM MES buffer (pH 4.8, adjusted with HCl and NaOH), containing $250\,\mu$M amino-modified DNA and $250\,$mM EDC (Merck: Art. No. E6383-1G), on a rotator at room temperature for $3\,$h. We used a colloid concentration of $11.35 \times 10^9\,\mathrm{mL}^{-1}$ for the reaction. Subsequently, the colloids were washed and incubated extensively in borate buffer (boric acid adjusted to pH 8.2 with NaOH) and deionized water to remove residual reaction components and hydrolyze unreacted activated carboxyl groups. We avoided buffers containing amino groups during washing to preserve the negative surface charge of the colloids. Finally, the colloids were diluted 1 to 5 to a concentration of $2.27 \times 10^9\,\mathrm{mL}^{-1}$ in deionized water, shock-frozen in liquid nitrogen, and stored at $-80\,^\circ$C. An extended protocol detailing the washing procedure is available in Section A.1.

Experimental Section

We conducted our trapping experiments using a 1:200000 dilution of the DNA-functionalized colloids relative to their initial stock concentration. We use $5\,$nM of complementary DNA and a $30\,\mu$L sample volume. We operated the trap for $5\,$min and recorded a video in both the brightfield and fluorescence channels. We then recorded another video in the brightfield channel, during which we turned off the trap to observe colloid sedimentation. We

resumed imaging the sedimented colloids in the brightfield and fluorescence channels for $2\,\mathrm{h}$. We terminated the experiment upon observing that the liquid in the sample chamber had evaporated.

Data Analysis and Video Editing

From the recorded videos, we generated Supplementary Movie 2. We adjusted the brightness levels throughout the first part of the video to ensure the visibility of the trapped DNA. We also created an overlay image, displayed in Figure 5.4, by combining an inverted brightfield image of the trapped colloids with a fluorescence image of the diffuse cloud of attracted DNA.

5.5.7 Formation of DNA Gels from DNA Nanostars (Section 5.2.4)

Experimental Section

For our experiments, we prepared a $1\,\mathrm{mL}$ solution of DNA nanostars in deionized water. The solution contains $5\,\mathrm{nM}$ of each of the three DNA strands that compose the Y-shaped nanostars, yielding an overall nanostar concentration of $5\,\mathrm{nM}$. We substituted $1\,\mathrm{nM}$ of one strand with a Cy5-labeled strand to produce fluorescent nanostars. We heated the sample on a heat block set to $90\,^{\circ}\mathrm{C}$ for $2\,\mathrm{min}$ and allowed it to cool to room temperature over $10\,\mathrm{min}$. We operated the diffusiophoretic trap using $30\,\mu\mathrm{L}$ of this fluorescent DNA solution. We recorded a microscopy video, capturing both the brightfield and fluorescence channels every $10\,\mathrm{s}$ to observe the polymerizing DNA nanostars. After approximately $17\,\mathrm{min}$, we turned off the trap but continued imaging. We repeated the experiment 6 times.

Data Analysis and Video Editing

To estimate the concentration of DNA nanostars in the diffusiophoretic trap, we apply the image correction method outlined in Section 5.5.4, using equation 5.5.4. We then follow the procedure detailed in Section 5.5.4 to measure the DNA concentration in a designated region of interest in front of the trap. The concentration versus time graphs for all replicates are displayed in Figure 5.8. A representative graph is shown in Figure 5.5. For visualization, we select fluorescence and brightfield frames from the recorded video at specific time points to document the evolving DNA gel structure. We adjust the brightness and contrast of these frames to maintain visibility across different fluorescence intensities.

These processed images appear in Figure 5.5. The full video, with brightness adjusted for all frames and channels, is accessible in Supplementary Movie 3.

Replicates

In Figure 5.8, we display the concentration versus time graphs for replicates of the DNA nanostar polymerization experiments, originally presented in Figure 5.5. The graphs generally show the same qualitative time-dependent trends with an initial rapid increase in DNA concentration in the trap and a subsequent decline during the onset of gel polymerization. During gel polymerization, the fluorescence level remains more or less constant, albeit with some variations and noise. We assume that these variations stem from variations in the shape of the flow fields and concentration gradients due to slight differences in the position and shape of the gel. When the trap is deactivated at around 17 minutes, the DNA concentration experiences an initial sharp decline, followed by a gradual decrease to 0 nM as the DNA gel dissociates. The graph labeled 'run 1' appears in Figure 5.5. In 'run 3', an unusual drop in DNA concentration occurs during the dissociation phase because the gel detached from the glass pipette and drifted away. In 'run 6', we inadvertently deactivated the trap one minute later than in the other runs.

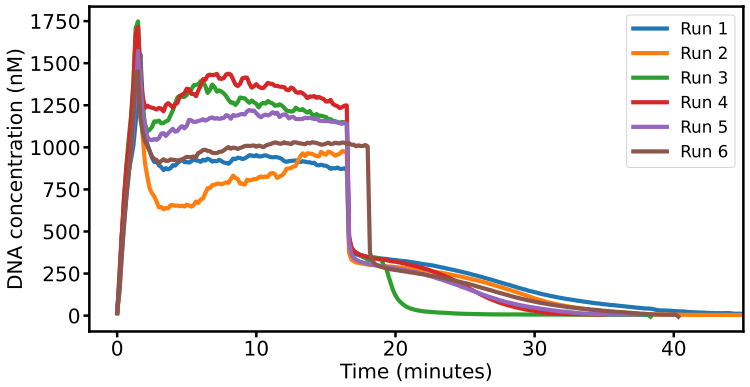

Figure 5.8. Replicates of the DNA nanostar polymerization experiment shown in Figure 5.5. The plots represent the average intensity in a region of interest corresponding to a sample volume of $280\,\mathrm{fL}$.

5.5.8 DNA Sequences

We order DNA from IDT in dry form and adopted the sequences from a previous study [193]. The sequences composing the DNA nanostars are listed in the table below, in 5' to 3' notation. Y2_CY5 is a modified version of the strand Y2, having a fluorescent dye instead

of a single-stranded overhang. /5Cy5/ is the notation of the fluorophore modification from the DNA supplier.

Label	Sequence	Length (nt)
Y1	GCTCGAGCCAGTGAGGACGGAAGTTTGTCGTAGCATCGCACC	42
Y2	GCTCGAGCCAACCACGCCTGTCCATTACTTCCGTCCTCACTG	42
Y3	GCTCGAGCGGTGCGATGCTACGACTTTGGACAGGCGTGGTTG	42
Y2_CY5	/5Cy5/AACCACGCCTGTCCATTACTTCCGTCCTCACTG	33

The sequence used to modify the colloids is listed in the table below and labeled as C2μ. C2μ* is designed to be complementary to the latter part of C2μ and features a fluorophore modification. Both sequences are designed to lack secondary structure, optimizing binding, as confirmed by NUPACK analysis. The prefix /5AmMC6/ denotes an amino modification, while /5Cy55/ denotes a fluorophore modification.

Label	Sequence	Length (nt)
C2μ	/5AmMC6/GTCTTTTATGCTGCTTATTCGTGTATATCCTGACCTAACTGAACTACCGCGCTAAAACTG	60
C2μ*	/5Cy55/CAGTTTTAGCGCGGTAGTTCAGTTAGGTCA	30

6. Summary and Outlook

In summary, my co-authors and I have provided a comprehensive explanation for a previously poorly understood colloidal patterning phenomenon in AC electric fields. Specifically, we discovered that hydrodynamic quadrupole flow, caused by Concentration Polarization Electroosmosis (CPEO) emerging around the colloids, is responsible for the patterning. Interestingly, it was recently found that similar patterns can also be created by AC magnetic fields acting on magnetic particles [194].

The existence of CPEO flows around spherical particles in AC electric fields led us to conclude that CPEO can be used to propel asymmetric particles. This understanding allowed us to complete the picture of AC electrophoresis (ACEP), which, as we found, can be achieved through Induced Charge Electrophoresis (ICEP) for metal particles, and through the mechanism we introduced, Concentration Polarization Electrophoresis (CPEP). I believe that a comprehensive understanding of AC electroosmosis, including CPEO and ICEO, may prove useful in creating novel microfluidic devices. ICEO is already extensively used in microfluidic devices [70–75]. Furthermore, I propose that the generic occurrence of CPEP, as demonstrated by us, might be useful for sorting particles based on their shape and composition. Finally, I envision sophisticated microrobotics applications going beyond the demonstrated action of simple silica dimers. One can construct microrobots out of more intriguing materials, such as living organisms or biocompatible materials, which would allow the addition of genetic circuits, biological or chemical sensors to the microrobots.

Concerning the diffusiophoretic trap we implemented, I believe similar traps could be utilized in low-cost sensing applications to extract nucleic acids from low-concentration environmental samples. Furthermore, the trap could be used to concentrate and assemble structures beyond DNA nanostars, such as DNA origamis and colloids, into macroscopic structures. Additionally, the trap could be used to separate particles and molecules based on their charge, as the direction of the focusing electric field depends on the employed electrolyte gradient. Importantly, our trap system, which utilizes simple diffusiophoresis in salt gradients, offers a promising platform for prebiotic evolution by concentrating organic molecules. Such a process is important in dilute primordial environments to promote interactions and the assembly of simple biomolecules into more complex structures [131].

A. Appendix

A.1 Functionalization of the Colloids

A.1.1 DNA sequences

The sequences of the oligonucleotides used for modification and cross-linking of the microparticles (in 5' to 3' direction) are listed below:

- `/5AmMC6/TTCGTTTTAGTCCCATTTGTTCAGTTTTTTCAGTTTTAGCGCGGTAGTTCAGTTAGGTCA`
- `/5AmMC6/GTCTTTTATGCTGCTTATTCGTGTATATCCTGACCTAACTGAACTACCGCGCTAAAACTG`

Here '/5AmMC6/' denotes the amino modification at the 5' end of the sequences by the oligo synthesis company (IDT).

A.1.2 Buffer and reagent stocks

The following buffers and reagents can be prepared in advance.

- 1 M MES buffer (Carl Roth: Art. No 4256.2) titrated to pH 4.8 with HCl and NaOH
- 0.1 M MES buffer diluted from the stock above
- 50 mM Borate buffer at pH 8.2 prepared by titrating boric acid (Carl Roth: Art. N0 6943.2) with HCl and NaOH
- 5'-amino-modified DNA diluted in deionized water to a concentration of 1 mM

Ethyl-3-(3-dimethyl-aminopropyl) carbodiimide (EDC) (Merck: Art. No. E6383-1G) is stored in dry form in small aliquots of approximately 20 mg at $-20\,^{\circ}$C and is later diluted in deionized water just before starting the bioconjugation reaction.

A.1.3 Colloid Concentrations

Carboxylated silica spheres with diameters $1.01\,\mu m$ (Lot: SiO_2-COOH-AR756-5ml) and $2.12\,\mu m$ (Lot: SiO_2-COOH-AR1060-5ml) were purchased from the microParticles GmbH. The colloids come at a weight per volume concentration of $c_W = 0.05\,g/mL$. This can be translated into a number density c via

$$c = \frac{c_W}{\rho \frac{4}{3}\pi \left(\frac{d}{2}\right)^3}$$

were $\rho = 1.85\,g/cm^3$ is the density of the colloids and d is their diameter. The number density of the colloids is thus given by

$$c_{1.01} = \frac{50 \cdot 10^9}{mL}$$
$$c_{2.12} = \frac{5.42 \cdot 10^9}{mL}.$$

The following relation between the colloid concentrations c^s in the reaction has to be fulfilled in order to have approximately the same number of reaction sites in a sample:

$$c^s_{2.12} = \left(\frac{1.01}{2.12}\right)^2 c^s_{1.01}, \tag{A.1}$$

which relates the number densities via the surface area of the colloids. We choose

$$c^s_{1.01} = 10 \cdot 10^9 \frac{1}{mL}$$
$$c^s_{2.12} = 2.27 \cdot 10^9 \frac{1}{mL}.$$

as the starting point for our protocol.

A.1.4 Protocol

0. Colloid Start Concentration

- vortex colloid stock solutions
- $2.12\,\mu m$ colloids: Pipet $419\,\mu L$ of colloids and $581\,\mu L$ of deionized water into a $1.5\,mL$ tube (dilution $1/2.386$)
- $1.01\,\mu m$ colloids: Pipet $200\,\mu L$ of colloids and $800\,\mu L$ of deionized water into a $1.5\,mL$ tube (dilution $1/5$)

1. Transfer Colloids into MES Buffer

- centrifuge the colloids at 250 rcf for 30 s and remove the supernatant (the Colloids should be sedimented)
- add 1 mL of 0.1 M MES buffer
- vortex briefly
- centrifuge the colloids at 250 rcf for 30 s (Colloids should be sedimented)
- add $100\,\mu$L of 0.1 M MES buffer at pH 4.8
- sonicate the colloids with a ultrasound generator at maximum power settings (20 W) for 1 min

The sonication with the ultrasound generator (Bandelin: SONOPLUS UW mini20) breaks up potentially aggregated colloids.

2. Modification Reaction

- create 1.25 M EDC stock solution: Disolve 12 mg of EDC in 50 µL deionized water
- add 50 µL of 1 mM amino-modified DNA and 10 µL of 1 M MES-buffer and 40 µL of 1.25 M EDC to a 0.5 mL tube
- vortex briefly
- add the 100 µL of the prepared colloids solution to the sample.
- vortex briefly
- incubate for 3 h on a rotator

3. Washing Procedure

The colloids are first washed with borate buffer to neutralize the acidic MES buffer and to hydrolize unreacted activated carboxyl groups. The colloids are then washed with deionized water to remove the borate buffer and any reactants that are unspecifically adsorbed to the colloids.

- transfer the sample to a 1.5 mL tube
- add 800 µL of 50 mM borate buffer to the sample.

- repeat the following steps for 5 times
  - centrifuge at 250 rcf for 30 s (the colloids should be sedimented) and remove the supernatant
  - add 1 mL of 50 mM borate buffer to the sample
  - vortex briefly; In round 4: sonicate at max settings for 1 min and incubate for 1.5 h on a rotator
- repeat the following steps for 5 times
  - Centrifuge at 1000 rcf for 30 s (Colloids should be sedimented) and remove the supernatant
  - add 1 mL of deionized water to the sample
  - vortex briefly; in round 4: sonicate at max setting for 1 min and incubate for 1.5 h on a rotator
- sonicate the colloids with a ultrasound generator at max settings for 1 min
- create aliquots, shock freeze in liquid nitrogen and store at $-80\,^{\circ}\mathrm{C}$

A.2 Raw Data (Microrobots Powered by Concentration Polarization Electrophoresis (CPEP)

A.2.1 Buffer Characterization

Tables A.1, A.3, A.5 and A.7 list all velocity measurements for all buffer conditions. Column 1 and 2 list the concentrations of the buffer ingredients. Column 3 (video no.) enumerates the videos recorded with the same buffer condition. Column 4 (dimer $(\mu\mathrm{m/s})$) reports the measured velocities of all dimers in a video as an ordered list. Column 5 (orientation) lists the orientations of the dimers from Column 4 encoded as 1 ('up') and -1 ('down'). Up corresponds to the case where the smaller particle of a dimer appears below the larger particle on the computer screen. Column 6 (reference $(\mu\mathrm{m/s})$) contains the measured velocities of all reference particles as an ordered list. Column 7 (average reference $(\mu\mathrm{m/s})$) lists the average velocity of the reference particles from Column 6 of one video. Column 8 (dimer corrected $(\mu\mathrm{m/s})$) lists the dimer velocities from Column 4 corrected by the average velocity of the reference particles from Column 7.

Tables A.2, A.4, A.6 and A.8 list the corrected velocity measurements, and the corresponding average and standard deviation for the given buffer compositions. Column 1 and 2 list the concentrations of the buffer ingredients. Column 3 (dimer corrected (µm/s)) list all corrected dimer velocities of a given buffer composition. Column 4 (average (µm/s)) reports the average of the corrected dimer velocities. Column 5 (standard deviation (µm/s)) lists the standard deviation of the corrected dimer velocities.

Table A.1. NaOH raw data

NaOH (µM)	$MgCl_2$ (µM)	video no.	dimer (µm/s)	orientation	reference (µm/s)	average reference (µm/s)	dimer corrected (µm/s)
10	5.2	1	-2.1584; 2.0315; 1.7996	1; -1; -1	-0.11963	-0.11963	2.0388; 2.1512; 1.9192
10	5.2	2	-2.11; 1.8049	1; -1	0.09221	0.09221	2.2022; 1.7127
10	5.2	3	1.7057; 1.6759	-1; -1	-0.22243; -0.26056; -0.17912	-0.2207	1.9264; 1.8966
25	0.2	1	-0.62871; -0.66528	-1; -1	-0.16556; -0.23086; -0.21944	-0.20529	-0.42343; -0.45999
25	0.2	2	-0.22598	1	-0.33294; -0.11588	-0.22441	0.0015664
25	0.2	3	-0.32598	-1	-0.1046	-0.1046	-0.22138
25	5.2	1	3.081; 2.9794	-1; -1	0.016034; 0.10796; 0.10584	0.076612	3.0044; 2.9028
25	5.2	2	-3.098; 3.1878	1; -1	-0.033192	-0.033192	3.0648; 3.221
25	5.2	3	-3.8004; 3.4204	1; -1	-0.24992; -0.36162; -0.092779; 0.1997	-0.12616	3.6742; 3.5466
50	0.2	1	-0.69124; 1.0838; 0.81608	-1; 1; 1	0.15563	0.15563	-0.84687; -0.92813; -0.66045
50	0.2	2	-1.0354; -1.1525	-1; -1	0.065881	0.065881	-1.1013; -1.2184
50	0.2	3	-0.69959; -0.90219; -0.88047	-1; -1; -1	-0.12209	-0.12209	-0.57749; -0.78009; -0.75838
50	5.2	1	0.36514; -0.75861	-1; 1	-0.011512	-0.011512	0.37665; 0.7471
50	5.2	2	0.49612; -0.9068	-1; 1	-0.12991; 0.10312; 0.039071	0.0040941	0.49203; 0.9109
50	5.2	3	-0.71939; -0.87973	1; 1	-0.09121	-0.09121	0.62818; 0.78852
100	5.2	1	-0.31532; -0.17464	1; -1	0.049767	0.049767	0.36509; -0.22441
100	5.2	2	0.05744; -0.03439	1; 1	-0.16706; 0.050236; -0.1582	-0.091673	-0.14911; -0.057283
100	5.2	3	-0.044189; 0.29934	1; 1	0.01613; -0.020345; -0.1041	-0.036106	0.0080835; -0.33544

Table A.2. NaOH corrected velocities

NaOH (µM)	$MgCl_2$ (µM)	dimer corrected (µm/s)	average (µm/s)	standard deviation (µm/s)
10	5.2	2.0388; 2.1512; 1.9192; 2.2022; 1.7127; 1.9264; 1.8966	1.9782	0.16687
25	0.2	-0.42343; -0.45999; 0.0015664; -0.22138	-0.27581	0.21261
25	5.2	3.0044; 2.9028; 3.0648; 3.221; 3.6742; 3.5466	3.2356	0.31069
50	0.2	-0.84687; -0.92813; -0.66045; -1.1013; -1.2184; -0.57749; -0.78009; -0.75838	-0.85889	0.2164
50	5.2	0.37665; 0.7471; 0.49203; 0.9109; 0.62818; 0.78852	0.65723	0.19825
100	5.2	0.36509; -0.22441; -0.14911; -0.057283; 0.0080835; -0.33544	-0.065514	0.24331

Table A.3. Tris raw data

Tris (µM)	$MgCl_2$ (µM)	video no.	dimer (µm/s)	orientation	reference (µm/s)	average reference (µm/s)	dimer corrected (µm/s)
10	5.2	1	2.1867; 2.112	-1; -1	-0.011658	-0.011658	2.1983; 2.1237
10	5.2	2	2.3178	-1	-0.28296; -0.093157	-0.18806	2.5058
10	5.2	3	2.0876; -2.5115	-1; 1	-0.01149	-0.01149	2.099; 2.5
10	5.2	4	2.384; -2.5342	-1; 1	-0.31553; 0.031664	-0.14193	2.526; 2.3922
25	5.2	1	2.7714; -1.5856	-1; 1	0.035405	0.035405	2.736; 1.621
25	5.2	2	-2.8863; 2.7368	1; -1	0.0074493	0.0074493	2.8938; 2.7293
25	5.2	3	-2.1166; -2.9565; 2.956	1; 1; -1	-0.0031657	-0.0031657	2.1135; 2.9533; 2.9592
50	0.2	1	0.24035; -0.29358; -0.29227	-1; 1; 1	-0.07472	-0.07472	0.31507; 0.21886; 0.21755
50	0.2	2	-0.18728; 0.3081; 0.067422	1; -1; -1	-0.10733; 0.014156	-0.046585	0.1407; 0.35468; 0.11401
50	0.2	3	-0.41175; -0.35746	1; 1	0.081775	0.081775	0.49352; 0.43924
50	5.2	1	2.2018; -2.4064	-1; 1	-0.082894	-0.082894	2.2847; 2.3235
50	5.2	2	2.2391; -2.415	-1; 1	0.042677; -0.078361	-0.017842	2.257; 2.3971
50	5.2	3	2.4588; -2.2549	-1; 1	-0.04447	-0.04447	2.5033; 2.2105
100	5.2	1	1.1616; -1.736; -1.8208	-1; 1; 1	-0.22214; -0.30256	-0.26235	1.424; 1.4736; 1.5584
100	5.2	2	1.7564; -1.4701	-1; 1	0.083002; 0.033984	0.058493	1.6979; 1.5286
100	5.2	3	-1.2916; 1.5386; -1.7132	1; -1; 1	-0.071143; 0.016444	-0.027349	1.2642; 1.566; 1.6859
250	5.2	1	0.82139; -0.63782	-1; 1	-0.016064	-0.016064	0.83745; 0.62176
250	5.2	2	-0.87382; -0.94419	1; 1	-0.03497	-0.03497	0.83885; 0.90922
250	5.2	3	-0.95719; -0.82211; 0.80946	1; 1; -1	-0.13714; 0.20802	0.035439	0.99263; 0.85755; 0.77402
500	5.2	1	-0.55723; 0.51097; -0.45549	1; -1; 1	-0.065543	-0.065543	0.49169; 0.57651; 0.38994
500	5.2	3	-0.54143; 0.78223	1; -1	-0.2473	-0.2473	0.29413; 1.0295

A.2.2 Electric Field Strength and Frequency Characterization

Table A.9, A.10 and A.11 each contain data obtained from measurements made on one individual dimer and a reference particle. Column 1 and 2 list the applied electric field amplitude and frequency. Column 3 lists the measured velocity of the dimer. Column 4

Table A.4. Tris corrected velocities

Tris (μM)	$MgCl_2$ (μM)	dimer corrected (μm/s)	average (μm/s)	standard deviation (μm/s)
10	5.2	2.1983; 2.1237; 2.5058; 2.099; 2.5; 2.526; 2.3922	2.335	0.18938
25	5.2	2.736; 1.621; 2.8938; 2.7293; 2.1135; 2.9533; 2.9592	2.5723	0.51075
50	0.2	0.31507; 0.21886; 0.21755; 0.1407; 0.35468; 0.11401; 0.49352; 0.43924	0.2867	0.13732
50	5.2	2.2847; 2.3235; 2.257; 2.3971; 2.5033; 2.2105	2.3293	0.10607
100	5.2	1.424; 1.4736; 1.5584; 1.6979; 1.5286; 1.2642; 1.566; 1.6859	1.5248	0.14114
250	5.2	0.83745; 0.62176; 0.83885; 0.90922; 0.99263; 0.85755; 0.77402	0.83307	0.11551
500	5.2	0.49169; 0.57651; 0.38994; 0.29413; 1.0295	0.55636	0.28501

Table A.5. NaCl raw data

NaCl (μM)	$MgCl_2$ (μM)	video no.	dimer (μm/s)	orientation	reference (μm/s)	average reference (μm/s)	dimer corrected (μm/s)
25	5.2	1	0.2565; -0.090399	-1; -1	-0.047559; -0.10738	-0.077468	0.33397; -0.01293
25	5.2	2	-0.0010654; -0.072518	1; -1	-0.083108	-0.083108	-0.082042; 0.01059
25	5.2	3	-0.058622; 0.077811; 0.20893	1; -1; -1	-0.0033616	-0.0033616	0.055261; 0.081173; 0.21229
50	0.2	1	-0.07064	-1	-0.10322	-0.10322	0.032583
50	0.2	2	-0.30739; 0.14427	-1; 1	-0.20242	-0.20242	-0.10497; -0.34669
50	0.2	3	0.23731; -0.0034925	1; 1	0.022871; 0.14171	0.08229	-0.15502; 0.085783
50	5.2	1	0.18548; -0.60578	-1; 1	0.10408; -0.16269; -0.13499	-0.064532	0.25002; 0.54125
50	5.2	2	0.35203; -0.4395	-1; 1	0.013808; 0.12143	0.067621	0.28441; 0.50712
50	5.2	3	-0.36842; 0.49881	1; -1	0.041369; -0.13753	-0.048079	0.32034; 0.54689
50	5.2	4	-0.62647; 0.5147; -0.6237	1; -1; 1	-0.011805; 0.0073405	-0.0022323	0.62424; 0.51693; 0.62146
100	0.2	1	-0.3359; -0.070846; -0.32053	1; 1; 1	-0.39082; -0.018323	-0.20457	0.13133; -0.13372; 0.11596
100	0.2	2	-0.050905	-1	-0.15048; -0.098426; -0.10022; 0.21803; -0.13712	-0.053645	0.0027406
100	0.2	3	0.041658; 0.27696; 0.091807	-1; -1; -1	0.035803; 0.092218	0.06401	-0.022352; 0.21295; 0.027797
100	0.2	4	-0.19775	1	-0.035193; 0.050215; -0.069265	-0.018081	0.17967
100	5.2	1	0.54022; -0.76891	-1; 1	-0.064309	-0.064309	0.60453; 0.7046
100	5.2	2	-0.9319; -0.94887	1; 1	-0.061837; 0.0075117; -0.099579	-0.051301	0.88059; 0.89757
100	5.2	3	0.51296; 0.58286	-1; -1	0.1632	0.1632	0.34976; 0.41966
100	5.2	4	0.59116; 0.54284	-1; -1	-0.0032619	-0.0032619	0.59442; 0.5461
250	5.2	1	0.35226; -0.81461	-1; 1	0.10234	0.10234	0.24992; 0.91694
250	5.2	2	0.57366; 0.52717; -0.74718	-1; -1; 1	-0.012219	-0.012219	0.58588; 0.53939; 0.73496
250	5.2	3	-0.43561; 0.52548	1; -1	-0.007625	-0.007625	0.42798; 0.53311
500	5.2	1	-0.23991; 0.53692; -0.27462	1; -1; 1	0.118; -0.19101	-0.036507	0.20341; 0.57343; 0.23812
500	5.2	2	0.69386; -0.13413	-1; 1	-0.16074	-0.16074	0.8546; -0.026605
500	5.2	3	0.36688; 0.44444	-1; -1	-0.10812	-0.10812	0.475; 0.55257

Table A.6. NaCl corrected velocities

NaCl (μM)	$MgCl_2$ (μM)	dimer corrected (μm/s)	average (μm/s)	standard deviation (μm/s)
25	5.2	0.33397; -0.01293; -0.082042; 0.01059; 0.055261; 0.081173; 0.21229	0.085472	0.14266
50	0.2	0.032583; -0.10497; -0.34669; -0.15502; 0.085783	-0.097663	0.17027
50	5.2	0.25002; 0.54125; 0.28441; 0.50712; 0.32034; 0.54689; 0.62424; 0.51693; 0.62146	0.46807	0.14427
100	0.2	0.13133; -0.13372; 0.11596; 0.0027406; -0.022352; 0.21295; 0.027797; 0.17967	0.064296	0.11614
100	5.2	0.60453; 0.7046; 0.88059; 0.89757; 0.34976; 0.41966; 0.59442; 0.5461	0.62465	0.19693
250	5.2	0.24992; 0.91694; 0.58588; 0.53939; 0.73496; 0.42798; 0.53311	0.56974	0.21321
500	5.2	0.20341; 0.57343; 0.23812; 0.8546; -0.026605; 0.475; 0.55257	0.41007	0.29205

Table A.7. $MgCl_2$ raw data

$MgCl_2$ (μM)	video no.	dimer (μm/s)	orientation	reference (μm/s)	average reference (μm/s)	dimer corrected (μm/s)
5	4	-0.1007	1	0.12329; 0.078374; 0.08571	0.095791	0.19649
5	1	0.89903; -0.73302	1; -1	0.033914	0.033914	-0.86511; -0.76694
5	2	0.50023; -0.76023	1; -1	0.040048	0.040048	-0.46019; -0.80028
5	3	0.61077; 0.64962	1; 1	-0.071589	-0.071589	-0.68236; -0.72121
10	1	-0.77615	-1	-0.11222	-0.11222	-0.66393
10	2	0.81232	1	-0.049807; 0.027225; -0.089389; 0.061394	-0.012644	-0.82496
10	3	-0.67114; -0.61298	-1; -1	0.16781; 0.0054852; -0.045543; 0.050324	0.04452	-0.71566; -0.6575
10	4	0.94059	1	-0.1349	-0.1349	-1.0755
10	5	-0.44429	-1	-0.061833; 0.035126; 0.065325	0.012873	-0.45717
25	1	-0.2533; 0.49167	1; 1	-0.20812	-0.20812	0.045177; -0.69979
25	2	-0.68736; -0.14944	-1; -1	-0.041324; -0.064957; -0.036963	-0.047748	-0.63961; -0.10169
25	3	-0.40842	-1	-0.099255	-0.099255	-0.30917
25	4	-0.31028; 0.63511	-1; 1	-0.021058	-0.021058	-0.28922; -0.65617
50	1	-0.043009	-1	0.0075411	0.0075411	-0.05055
50	2	-0.1422; -0.13616	-1; 1	0.0054712	0.0054712	-0.14768; 0.14163
50	3	-0.079519; 0.080918	-1; 1	-0.045867	-0.045867	-0.033653; -0.12679
100	1	0.11921	-1	0.0010629	0.0010629	0.11815
100	2	0.18407	-1	0.074598; 0.051411	0.063005	0.12106
100	3	0.31911; 0.23815	-1; -1	-0.0078792; -0.064006	-0.035943	0.35505; 0.27409
100	4	-0.46523	1	0.066031; 0.24479	0.15541	0.62064
100	5	0.29586; -0.21409	-1; 1	-0.060438	-0.060438	0.35629; 0.15366
250	1	-0.2334	1	-0.062887	-0.062887	0.17051
250	2	0.24637	-1	0.0055673; -0.030459; -0.0033249	-0.0094054	0.25577
250	3	0.33192; -0.28766	-1; 1	0.061578	0.061578	0.27034; 0.34924

Table A.8. $MgCl_2$ corrected velocities

$MgCl_2$ (μM)	dimer corrected (μm/s)	average (μm/s)	standard deviation (μm/s)
5	-0.86511; -0.76694; -0.46019; -0.80028; -0.68236; -0.72121	-0.71601	0.14038
10	-0.66393; -0.82496; -0.71566; -0.6575; -1.0755; -0.45717	-0.73245	0.20621
25	0.045177; -0.69979; -0.63961; -0.10169; -0.30917; -0.28922; -0.65617	-0.37864	0.29366
50	-0.05055; -0.14768; 0.14163; -0.033653; -0.12679; 0.19649	-0.0034233	0.14154
100	0.11815; 0.12106; 0.35505; 0.27409; 0.62064; 0.35629; 0.15366	0.28556	0.18015
250	0.17051; 0.25577; 0.27034; 0.34924	0.26147	0.073229

lists the velocity of the reference particle. Column 5 lists the corrected velocity of the dimer.

Table A.9. Swimmer 1

electric field (mV/μm)	frequency (Hz)	dimer (μm/s)	reference (μm/s)	dimer corrected (μm/s)
3.05	250	-0.04425	-0.05515	0.01089
4.57	250	0.18415	-0.07716	0.26130
6.09	250	-0.36709	-0.05731	0.30978
7.61	250	-0.58703	-0.06520	0.52183
9.14	250	0.73478	-0.10905	0.84382
10.66	250	-1.01412	-0.04195	0.97218
12.18	250	1.08429	-0.07286	1.15715
13.71	250	-1.58886	-0.00330	1.58556
15.23	250	1.90124	0.06676	1.83448
16.75	250	-2.27900	0.02538	2.30438
16.75	500	-1.90459	0.10462	2.00922
16.75	750	1.27442	0.04976	1.22466
16.75	1000	0.84186	-0.06135	0.90321
16.75	1500	-0.14115	0.23458	0.37573
16.75	2000	0.00711	0.11272	0.10561

Table A.10. Swimmer 2

electric field (mV/μm)	frequency (Hz)	dimer (μm/s)	reference (μm/s)	dimer corrected (μm/s)
3.05	250	-0.07672	-0.03346	0.04326
4.57	250	-0.23488	-0.05509	0.17980
6.09	250	0.29167	-0.13350	0.42517
7.61	250	0.50567	-0.10702	0.61269
9.14	250	-0.96007	-0.15874	0.80133
10.66	250	0.91369	-0.09650	1.01020
12.18	250	1.37226	-0.08227	1.45453
13.71	250	-1.85958	-0.19601	1.66357
15.23	250	2.01217	-0.13712	2.14930
16.75	250	-2.41953	0.00508	2.42461
16.75	500	1.90613	-0.27114	2.17727
16.75	750	-1.64252	-0.34347	1.29905
16.75	1000	-1.02669	-0.22037	0.80632
16.75	1500	-0.51470	-0.02538	0.48932
16.75	2000	-0.40936	-0.36060	0.04876

Table A.11. Swimmer 3

electric field (mV/μm)	frequency (Hz)	dimer (μm/s)	reference (μm/s)	dimer corrected (μm/s)
3.05	250	-0.05914	0.00575	0.06489
4.57	250	0.13688	-0.03549	0.17237
6.09	250	0.16393	-0.06861	0.23254
7.61	250	0.37440	-0.14963	0.52403
9.14	250	0.53618	-0.12732	0.66351
10.66	250	-1.00302	-0.16564	0.83737
12.18	250	-1.13091	0.05384	1.18474
13.71	250	1.15126	-0.26317	1.41444
15.23	250	1.65991	-0.01931	1.67923
16.75	250	-1.95483	-0.12504	1.82979
16.75	500	-1.72144	-0.12492	1.59652
16.75	750	-1.33342	-0.13304	1.20038
16.75	1000	0.71604	-0.08498	0.80102
16.75	1500	-0.41806	-0.11272	0.30534
16.75	2000	0.17822	0.09728	0.08093

Bibliography

[1] H. Helmholtz, "Studien über electrische grenzschichten," *Ann. Phys.*, vol. 243, pp. 337–382, Jan. 1879.

[2] G. Quincke, "Ueber die fortführung materieller theilchen durch strömende elektricität," *Ann. Phys.*, vol. 189, pp. 513–598, Jan. 1861.

[3] M. von Smoluchowski, "Contribution à la théorie de l'endosmose électrique et de quelques phénomènes corrélatifs," *Bulletin de l'Académie des sciences de Cracovie*, p. 184, 1903.

[4] M. Gouy, "Sur la constitution de la charge électrique à la surface d'un électrolyte," *Journal de Physique Théorique et Appliquée*, vol. 9, no. 1, pp. 457–468, 1910.

[5] D. L. Chapman, "Li. a contribution to the theory of electrocapillarity," *Lond. Edinb. Dublin Philos. Mag. J. Sci.*, vol. 25, pp. 475–481, Apr. 1913.

[6] P. Debye and E. Hückel, "Zur theorie der elektrolyte. i. gefrierpunktserniedrigung und verwandte erscheinungen," *Phys. Z.*, vol. 24, pp. 185–206, 1923.

[7] D. Henry, "The cataphoresis of suspended particles. part i.—the equation of cataphoresis," *Proc. R. Soc. London A.*, vol. 133, pp. 106–129, Sept. 1931.

[8] F. Morrison, "Electrophoresis of a particle of arbitrary shape," *J. Colloid Interf. Sci.*, vol. 34, no. 2, pp. 210–214, 1970.

[9] J. J. Bikerman, "Zur theorie der kataphorese und elektrosmose," *Z Phys Chem (N F)*, vol. 171A, pp. 209–220, Nov. 1934.

[10] J. J. Bikerman, "Electrokinetic equations and surface conductance. a survey of the diffuse double layer theory of colloidal solutions," *Trans. Faraday Soc.*, vol. 35, p. 154, 1940.

[11] S. S. Dukhin and V. N. Shilov, "Theory of static polarization of diffuse part of thin electric double layer of spherical particles," *Colloid Journal of the USSR*, vol. 31, p. 564, 1969.

[12] R. W. O'Brien and L. R. White, "Electrophoretic mobility of a spherical colloidal particle," *J. Chem. Soc., Faraday trans. II*, vol. 74, p. 1607, 1978.

[13] R. W. O'Brien and R. J. Hunter, "The electrophoretic mobility of large colloidal particles," *Can. J. Chemistry*, vol. 59, no. 13, pp. 1878–1887, 1981.

[14] R. O'Brien, "The solution of the electrokinetic equations for colloidal particles with thin double layers," *J. Colloid Interf. Sci.*, vol. 92, no. 1, pp. 204–216, 1983.

[15] J. T. G. Overbeek, "Theorie der electrophorese – het relaxatie-effect," 2019.

[16] P. Wiersema, A. Loeb, and J. Overbeek, "Calculation of the electrophoretic mobility of a spherical colloid particle," *J. Colloid Interf. Sci.*, vol. 22, no. 1, pp. 78–99, 1966.

[17] B. V. Derjaguin, G. P. Sidorenko, E. A. Zubashchenko, and A. A. Korotkova, "Kinetic phenomena in the boundary layers of liquids," *Colloid Journal of the USSR*, vol. 9, pp. 335–347, 1947.

[18] D. C. Prieve, J. L. Anderson, J. P. Ebel, and M. E. Lowell, "Motion of a particle generated by chemical gradients. part 2. electrolytes," *J. Fluid Mech.*, vol. 148, pp. 247–269, 1984.

[19] D. C. Prieve and R. Roman, "Diffusiophoresis of a rigid sphere through a viscous electrolyte solution," *J. Chem. Soc., Faraday trans. II*, vol. 83, no. 8, p. 1287, 1987.

[20] S. S. Dukhin, "Boundary layer near the surface of a solid body and low-frequency dielectric dispersion," *Spec. Discuss. Faraday Soc.*, vol. 1, p. 158, 1970.

[21] S. S. Dukhin, V. N. Shilov, and J. J. Bikerman, "Dielectric phenomena and double layer in disperse systems and polyelectrolytes," *J. Electrochem. Soc.*, vol. 121, no. 4, p. 154C, 1974.

[22] G. Schwarz, "A theory of the low-frequency dielectric dispersion of colloidal particles in electrolyte solution1,2," *J. Phys. Chem-us.*, vol. 66, pp. 2636–2642, Dec. 1962.

[23] H. P. Schwan, *Electrical Properties of Tissue and Cell Suspensions*, pp. 147–209. Elsevier, 1957.

[24] J. Lyklema, S. S. Dukhin, and V. N. Shilov, "The relaxation of the double layer around colloidal particles and the low-frequency dielectric dispersion," *J. Electroanal. Chem. Interfacial Electrochem.*, vol. 143, no. 1-2, pp. 1–21, 1983.

[25] N. I. Gamayunov, V. A. Murtsovkin, and A. S. Dukhin, "Pair interaction of particles in electric field. 1. features of hydrodynamic interaction of polarized particles," *Colloid Journal of the USSR (English Translation)*, vol. 48, no. 2, pp. 233–239, 1986.

[26] A. S. Dukhin and V. A. Murtsovkin, "Pair interaction of particles in electric field. 2. influence of polarization of double layer of dielectric particles on their hydrodynamic interaction in a stationary electric field," *Colloid Journal of the USSR (English Translation)*, vol. 48, no. 2, pp. 240–247, 1986.

[27] A. S. Dukhin, "Pair interaction of disperse particles in electric field. 3. hydrodynamic interaction of ideally polarizable metal particles and dead biological cells," *Colloid Journal of the USSR (English Translation)*, vol. 48, no. 3, pp. 439–445, 1986.

[28] A. Ramos, H. Morgan, N. G. Green, and A. Castellanos, "Ac electrokinetics: a review of forces in microelectrode structures," *J. Phys. D: Appl. Phys.*, vol. 31, pp. 2338–2353, Sept. 1998.

[29] A. Ramos, H. Morgan, N. G. Green, and A. Castellanos, "Ac electric-field-induced fluid flow in microelectrodes," *J. Colloid Interf. Sci.*, vol. 217, pp. 420–422, Sept. 1999.

[30] T. M. Squires and M. Z. Bazant, "Induced-charge electro-osmosis," *J. Fluid Mech.*, vol. 509, pp. 217–252, 2004.

[31] T. M. Squires and M. Z. Bazant, "Breaking symmetries in induced-charge electro-osmosis and electrophoresis," *J. Fluid Mech.*, vol. 560, p. 65, 2006.

[32] O. Schnitzer and E. Yariv, "Macroscale description of electrokinetic flows at large zeta potentials: nonlinear surface conduction," *Phys. Rev. E*, vol. 86, no. 2, p. 021503, 2012.

[33] O. Schnitzer, R. Zeyde, I. Yavneh, and E. Yariv, "Weakly nonlinear electrophoresis of a highly charged colloidal particle," *Phys. Fluids*, vol. 25, no. 5, p. 052004, 2013.

[34] V. Calero, R. Fernández-Mateo, H. Morgan, P. García-Sánchez, and A. Ramos, "Stationary electro-osmotic flow driven by ac fields around insulators," *Phys. Rev. Applied*, vol. 15, p. 014047, Jan. 2021.

[35] F. Katzmeier, B. Altaner, J. List, U. Gerland, and F. C. Simmel, "Emergence of colloidal patterns in ac electric fields," *Phys. Rev. Lett.*, vol. 128, p. 058002, Feb. 2022.

[36] R. Fernández-Mateo, P. García-Sánchez, V. Calero, H. Morgan, and A. Ramos, "Stationary electro-osmotic flow driven by AC fields around charged dielectric spheres," *J. Fluid Mech.*, vol. 924, p. R2, 2021.

[37] C. Grosse, "Generalization of a classic thin double layer polarization theory of colloidal suspensions to electrolyte solutions with different ion valences," *J. Phys. Chem. B*, vol. 113, no. 26, pp. 8911–8924, 2009.

[38] C. Grosse, "Generalization of a classic theory of the low frequency dielectric dispersion of colloidal suspensions to electrolyte solutions with different ion valences," *J. Phys. Chem. B*, vol. 113, no. 32, pp. 11201–11215, 2009.

[39] S. Dukhin, "Non-equilibrium electric surface phenomena," *Adv. Colloid Interfac.*, vol. 44, pp. 1–134, 1993.

[40] J. L. Anderson and D. C. Prieve, "Diffusiophoresis: Migration of colloidal particles in gradients of solute concentration," *Separ. Purif. Method.*, vol. 13, no. 1, pp. 67–103, 1984.

[41] P. Hiemenz, *Principles of Colloid and Surface Chemistry, Revised and Expanded, 3rd Edition*. Erscheinungsort nicht ermittelbar and Boston, MA: CRC Press and Safari, 3rd edition ed., 2016.

[42] H. Ohshima, *Theory of colloid and interfacial electric phenomena*, vol. 12 of *Interface science and technology*. Amsterdam: Elsevier/Academic Press, 2006.

[43] J. L. Anderson, "Colloid transport by interfacial forces," *Annu. Rev. Fluid Mech.*, vol. 21, no. 1, pp. 61–99, 1989.

[44] A. S. Jayaraman, E. Klaseboer, and D. Y. Chan, "The unusual fluid dynamics of particle electrophoresis," *J. Colloid Interf. Sci.*, vol. 553, pp. 845–863, Oct. 2019.

[45] G. K. Batchelor, *An Introduction to fluid dynamics*. Cambridge mathematical library, Cambridge: Cambridge Univ. Press, 1. cambridge mathematical ed., 14. print ed., 2010.

[46] S. Marbach, H. Yoshida, and L. Bocquet, "Local and global force balance for diffusiophoretic transport," *J. Fluid Mech.*, vol. 892, 2020.

[47] M. Planck, "Ueber die potentialdifferenz zwischen zwei verdünnten lösungen binärer electrolyte," *Ann. Phys.*, vol. 276, no. 8, pp. 561–576, 1890.

[48] H. Isambert, A. Ajdari, J.-L. Viovy, and J. Prost, "Electrohydrodynamic patterns in macroion dispersions under a strong electric field," *Phys. Rev. E*, vol. 56, no. 5, pp. 5688–5704, 1997.

[49] Y. Hu, J. L. Glass, A. E. Griffith, and S. Fraden, "Observation and simulation of electrohydrodynamic instabilities in aqueous colloidal suspensions," *J. Chem. Phys.*, vol. 100, no. 6, pp. 4674–4682, 1994.

[50] B. R. Jennings, M. Stankiewicz, "Electro-optic observations of electrodynamic band formation in colloidal suspensions," *Proc. Math. Phys. Eng. Sci.*, vol. 427, no. 1873, pp. 321–330, 1990.

[51] Geoffrey Ingram Taylor, "Studies in electrohydrodynamics. i. the circulation produced in a drop by an electric field," *Proc. Math. Phys. Eng. Sci.*, vol. 291, no. 1425, pp. 159–166, 1966.

[52] I. Prigogine and G. Nicolis, "On symmetry–breaking instabilities in dissipative systems," *J. Chem. Phys.*, vol. 46, no. 9, pp. 3542–3550, 1967.

[53] I. Prigogine and R. Lefever, "Symmetry breaking instabilities in dissipative systems. ii," *J. Chem. Phys.*, vol. 48, no. 4, pp. 1695–1700, 1968.

[54] P. P. Lele, M. Mittal, and E. M. Furst, "Anomalous particle rotation and resulting microstructure of colloids in ac electric fields," *Langmuir*, vol. 24, no. 22, pp. 12842–12848, 2008.

[55] M. Mittal, P. P. Lele, E. W. Kaler, and E. M. Furst, "Polarization and interactions of colloidal particles in ac electric fields," *J. Chem. Phys.*, vol. 129, no. 6, p. 064513, 2008.

[56] J. H. Masliyah and S. Bhattacharjee, *Electrokinetic and colloid transport phenomena*. Hoboken, N.J: Wiley-Interscience, 2006.

[57] S. S. Dukhin, *Twentieth Intl Cong. on Pure and Applied Chemistry*. 1965.

[58] H. Ohshima, T. W. Healy, and L. R. White, "Approximate analytic expressions for the electrophoretic mobility of spherical colloidal particles and the conductivity of their dilute suspensions," *J. Chem. Soc., Faraday trans. II*, vol. 79, no. 11, p. 1613, 1983.

[59] H. Ohshima, "Electrophoresis of soft particles," *Adv. Colloid Interfac.*, vol. 62, no. 2-3, pp. 189–235, 1995.

[60] C. Grosse, "Extension of a classic low frequency dielectric dispersion theory of colloidal suspensions to include different counterion and co-ion valences, a broad frequency range, and the stagnant layer conductivity," *J. Phys. Chem. B*, vol. 116, no. 45, pp. 13538–13553, 2012.

[61] S. S. Dukhin, "Electrokinetic phenomena of the second kind and their applications," *Adv. Colloid Interfac.*, vol. 35, pp. 173–196, 1991.

[62] A. V. Delgado, F. González-Caballero, R. Hunter, L. K. Koopal, and J. Lyklema, "Measurement and interpretation of electrokinetic phenomena (iupac technical report)," *Pure Appl. Chem.*, vol. 77, no. 10, pp. 1753–1805, 2005.

[63] Y.-R. Shi, M.-P. Ye, L.-C. Du, and Y.-X. Weng, "Experimental determination of particle size-dependent surface charge density for silica nanospheres," *J. Phys. Chem. C*, vol. 122, no. 41, pp. 23764–23771, 2018.

[64] V. Shilov, A. Delgado, F. Gonzalez-Caballero, and C. Grosse, "Thin double layer theory of the wide-frequency range dielectric dispersion of suspensions of non-conducting spherical particles including surface conductivity of the stagnant layer," *Colloids Surf., A*, vol. 192, no. 1-3, pp. 253–265, 2001.

[65] J. Lyklema, M. M. Springer, V. N. Shilov, and S. S. Dukhin, "The relaxation of the double layer around colloidal particles and the low-frequency dielectric dispersion," *J. Electroanal. Chem. Interfacial Electrochem.*, vol. 198, no. 1, pp. 19–26, 1986.

[66] C. Grosse and V. N. Shilov, "Theory of the low-frequency electrorotation of polystyrene particles in electrolyte solution," *J. Phys. Chem. A*, vol. 100, no. 5, pp. 1771–1778, 1996.

[67] M. J. Lighthill, "On the squirming motion of nearly spherical deformable bodies through liquids at very small reynolds numbers," *Comm. Pure Appl. Math.*, vol. 5, no. 2, pp. 109–118, 1952.

[68] J. R. Blake, "A spherical envelope approach to ciliary propulsion," *J. Fluid Mech.*, vol. 46, no. 1, pp. 199–208, 1971.

[69] B. Derjaguin and L. Landau, "Theory of the stability of strongly charged lyophobic sols and of the adhesion of strongly charged particles in solutions of electrolytes," *Prog. Surf. Sci.*, vol. 43, no. 1, pp. 30–59, 1993.

[70] M. Z. Bazant and Y. Ben, "Theoretical prediction of fast 3d ac electro-osmotic pumps," *Lab Chip*, vol. 6, no. 11, pp. 1455–1461, 2006.

[71] F. J. Hong, J. Cao, and P. Cheng, "A parametric study of ac electrothermal flow in microchannels with asymmetrical interdigitated electrodes," *Int. Commun. Heat Mass Transfer*, vol. 38, no. 3, pp. 275–279, 2011.

[72] W. Y. Ng, S. Goh, Y. C. Lam, C. Yang, and I. Rodríguez, "Dc-biased ac-electroosmotic and ac-electrothermal flow mixing in microchannels," *Lab Chip*, vol. 9, no. 6, pp. 802–809, 2009.

[73] C.-C. Huang, M. Z. Bazant, and T. Thorsen, "Ultrafast high-pressure ac electro-osmotic pumps for portable biomedical microfluidics," *Lab Chip*, vol. 10, no. 1, pp. 80–85, 2010.

[74] J. P. Urbanski, T. Thorsen, J. A. Levitan, and M. Z. Bazant, "Fast ac electro-osmotic micropumps with nonplanar electrodes," *Appl. Phys. Lett.*, vol. 89, no. 14, p. 143508, 2006.

[75] J. Wu, "ac electro-osmotic micropump by asymmetric electrode polarization," *J. Appl. Phys.*, vol. 103, no. 2, p. 024907, 2008.

[76] S. Gangwal, O. J. Cayre, M. Z. Bazant, and O. D. Velev, "Induced-charge electrophoresis of metallodielectric particles," *Phys. Rev. Lett.*, vol. 100, no. 5, p. 058302, 2008.

[77] C. Peng, I. Lazo, S. V. Shiyanovskii, and O. D. Lavrentovich, "Induced-charge electro-osmosis around metal and janus spheres in water: Patterns of flow and breaking symmetries," *Phys. Rev. E*, vol. 90, no. 5-1, p. 051002, 2014.

[78] T. Mano, J.-B. Delfau, J. Iwasawa, and M. Sano, "Optimal run-and-tumble-based transportation of a janus particle with active steering," *Proc. Natl. Acad. Sci. U.S.A.*, vol. 114, no. 13, pp. E2580–E2589, 2017.

[79] D. Nishiguchi and M. Sano, "Mesoscopic turbulence and local order in janus particles self-propelling under an ac electric field," *Phys. Rev. E*, vol. 92, no. 5, p. 052309, 2015.

[80] D. Nishiguchi, J. Iwasawa, H.-R. Jiang, and M. Sano, "Flagellar dynamics of chains of active janus particles fueled by an ac electric field," *New J. Phys.*, vol. 20, no. 1, p. 015002, 2018.

[81] A. Boymelgreen and G. Yossifon, "Observing electrokinetic janus particle-channel wall interaction using microparticle image velocimetry," *Langmuir*, vol. 31, no. 30, pp. 8243–8250, 2015.

[82] "Properties — microparticles gmbh." `https://microparticles.de/en/properties.html`, 23.07.2020.

[83] E. A. Frankel, P. C. Bevilacqua, and C. D. Keating, "Polyamine/nucleotide coacervates provide strong compartmentalization of mg^{2+}, nucleotides, and rna," *Langmuir*, vol. 32, no. 8, pp. 2041–2049, 2016.

[84] E. Kopperger, J. List, S. Madhira, F. Rothfischer, D. C. Lamb, and F. C. Simmel, "A self-assembled nanoscale robotic arm controlled by electric fields," *Science*, vol. 359, no. 6373, pp. 296–301, 2018.

[85] Q. Tseng, I. Wang, E. Duchemin-Pelletier, A. Azioune, N. Carpi, J. Gao, O. Filhol, M. Piel, M. Théry, and M. Balland, "A new micropatterning method of soft substrates reveals that different tumorigenic signals can promote or reduce cell contraction levels," *Lab Chip*, vol. 11, no. 13, pp. 2231–2240, 2011.

[86] T. Lindeberg, "Scale-space theory: a basic tool for analyzing structures at different scales," *J. Appl. Stat.*, vol. 21, no. 1-2, pp. 225–270, 1994.

[87] F. Katzmeier, "Interacting brownian particle simulation." `https://github.com/Katzi93/Interacting_Brownian_Particle_Simulation`, 2021.

[88] C. H. Li and C. K. Lee, "Minimum cross entropy thresholding," *Pattern Recogn.*, vol. 26, no. 4, pp. 617–625, 1993.

[89] "Calculate density and viscosity of glycerol/water mixtures." `http://www.met.reading.ac.uk/~sws04cdw/viscosity_calc.html`, 07.10.2021.

[90] A. Volk and C. J. Kähler, "Density model for aqueous glycerol solutions," *Exp. Fluids*, vol. 59, no. 5, pp. 1–4, 2018.

[91] N.-S. Cheng, "Formula for the viscosity of a glycerol−water mixture," *Ind. Eng. Chem. Res.*, vol. 47, no. 9, pp. 3285–3288, 2008.

[92] F. Katzmeier and F. C. Simmel, "Microrobots powered by concentration polarization electrophoresis (cpep)," *Nat. Commun.*, vol. 14, Oct. 2023.

[93] R. Fernández-Mateo, V. Calero, H. Morgan, P. García-Sánchez, and A. Ramos, "Wall repulsion of charged colloidal particles during electrophoresis in microfluidic channels," *Phys. Rev. Lett.*, vol. 128, no. 7, p. 074501, 2022.

[94] R. Fernández-Mateo, H. Morgan, A. Ramos, and P. García-Sánchez, "Wall repulsion during electrophoresis: Testing the theory of concentration-polarization electro-osmosis," *Phys. Fluids*, vol. 35, no. 1, p. 012019, 2023.

[95] F. Ma, X. Yang, H. Zhao, and N. Wu, "Inducing propulsion of colloidal dimers by breaking the symmetry in electrohydrodynamic flow," *Phys. Rev. Lett.*, vol. 115, no. 20, p. 208302, 2015.

[96] A. Boymelgreen, G. Yossifon, and T. Miloh, "Propulsion of active colloids by self-induced field gradients," *Langmuir*, vol. 32, no. 37, pp. 9540–9547, 2016.

[97] A. F. Demirörs, M. T. Akan, E. Poloni, and A. R. Studart, "Active cargo transport with janus colloidal shuttles using electric and magnetic fields," *Soft Matter*, vol. 14, no. 23, pp. 4741–4749, 2018.

[98] X. Zhu, Y. Gao, R. Mhana, T. Yang, B. L. Hanson, X. Yang, J. Gong, and N. Wu, "Synthesis and propulsion of magnetic dimers under orthogonally applied electric and magnetic fields," *Langmuir*, vol. 37, no. 30, pp. 9151–9161, 2021.

[99] A. M. Boymelgreen, T. Balli, T. Miloh, and G. Yossifon, "Active colloids as mobile microelectrodes for unified label-free selective cargo transport," *Nat. Commun.*, vol. 9, no. 1, p. 760, 2018.

[100] X. Huo, Y. Wu, A. Boymelgreen, and G. Yossifon, "Analysis of cargo loading modes and capacity of an electrically-powered active carrier," *Langmuir*, vol. 36, no. 25, 2019.

[101] D. C. Prieve, P. J. Sides, and C. L. Wirth, "2-d assembly of colloidal particles on a planar electrode," *Curr. Opin. Colloid In.*, vol. 15, no. 3, pp. 160–174, 2010.

[102] W. D. Ristenpart, I. A. Aksay, and D. A. Saville, "Electrohydrodynamic flow around a colloidal particle near an electrode with an oscillating potential," *J. Fluid Mech.*, vol. 575, pp. 83–109, 2007.

[103] J. J. Arcenegui, P. García-Sánchez, H. Morgan, and A. Ramos, "Electro-orientation and electrorotation of metal nanowires," *Phys. Rev. E*, vol. 88, no. 6, p. 063018, 2013.

[104] B. Edwards and N. Engheta, "Electric tweezers: negative dielectrophoretic multiple particle positioning," *New J. Phys.*, vol. 14, no. 6, p. 063012, 2012.

[105] B. Edwards, N. Engheta, and S. Evoy, "Electric tweezers: Experimental study of positive dielectrophoresis-based positioning and orientation of a nanorod," *J. Appl. Phys.*, vol. 102, no. 2, p. 024913, 2007.

[106] D. L. Fan, R. C. Cammarata, and C. L. Chien, "Precision transport and assembling of nanowires in suspension by electric fields," *Appl. Phys. Lett.*, vol. 92, no. 9, p. 093115, 2008.

[107] R. Pethig, "Review article-dielectrophoresis: status of the theory, technology, and applications," *Biomicrofluidics*, vol. 4, no. 2, 2010.

[108] P. P. Mathai, P. T. Carmichael, B. A. Shapiro, and J. A. Liddle, "Simultaneous positioning and orientation of single nano-wires using flow control," *RSC Adv.*, vol. 3, no. 8, p. 2677, 2013.

[109] V. T. Milam, A. L. Hiddessen, J. C. Crocker, D. J. Graves, and D. A. Hammer, "Dna-driven assembly of bidisperse, micron-sized colloids," *Langmuir*, vol. 19, no. 24, pp. 10317–10323, 2003.

[110] Z. Zeravcic, V. N. Manoharan, and M. P. Brenner, "Colloquium : Toward living matter with colloidal particles," *Rev. Mod. Phys.*, vol. 89, no. 3, 2017.

[111] Y. Wang, Y. Wang, D. R. Breed, V. N. Manoharan, L. Feng, A. D. Hollingsworth, M. Weck, and D. J. Pine, "Colloids with valence and specific directional bonding," *Nature*, vol. 491, no. 7422, pp. 51–55, 2012.

[112] R. Dreyfus, M. E. Leunissen, R. Sha, A. V. Tkachenko, N. C. Seeman, D. J. Pine, and P. M. Chaikin, "Simple quantitative model for the reversible association of dna coated colloids," *Phys. Rev. Lett.*, vol. 102, no. 4, p. 048301, 2009.

[113] T. B. Jones, *Electromechanics of Particles*. Cambridge University Press, 2009.

[114] B. Ng and P. H. Barry, "The measurement of ionic conductivities and mobilities of certain less common organic ions needed for junction potential corrections in electrophysiology," *J. Neurosci. Meth.*, vol. 56, no. 1, pp. 37–41, 1995.

[115] A. S. Khair and B. Balu, "Breaking electrolyte symmetry in induced-charge electro-osmosis," *J. Fluid Mech.*, vol. 905, 2020.

[116] O. Schnitzer and E. Yariv, "Strong electro-osmotic flows about dielectric surfaces of zero surface charge," *Phys. Rev. E*, vol. 89, no. 4, p. 043005, 2014.

[117] E. Rowatt and R. J. Williams, "The binding of polyamines and magnesium to dna," *J. Inorg. Biochem.*, vol. 46, no. 2, pp. 87–97, 1992.

[118] A. M Boymelgreen, G. Kunti, P. Garcia-Sanchez, A. Ramos, G. Yossifon, and T. Miloh, "The role of particle-electrode wall interactions in mobility of active janus particles driven by electric fields," *J. Colloid Interf. Sci.*, vol. 616, pp. 465–475, 2022.

[119] Y. Wu, A. Fu, and G. Yossifon, "Active particles as mobile microelectrodes for selective bacteria electroporation and transport," *Sci. Adv.*, vol. 6, no. 5, p. eaay4412, 2020.

[120] S. Park and G. Yossifon, "Micromotor-based biosensing using directed transport of functionalized beads," *ACS Sens.*, vol. 5, no. 4, pp. 936–942, 2020.

[121] L. Zhang, Z. Xiao, X. Chen, J. Chen, and W. Wang, "Confined 1d propulsion of metallodielectric janus micromotors on microelectrodes under alternating current electric fields," *ACS Nano*, vol. 13, no. 8, pp. 8842–8853, 2019.

[122] Z. Wang, Z. Wang, J. Li, S. T. H. Cheung, C. Tian, S.-H. Kim, G.-R. Yi, E. Ducrot, and Y. Wang, "Active patchy colloids with shape-tunable dynamics," *J. Am. Chem. Soc.*, vol. 141, no. 37, pp. 14853–14863, 2019.

[123] J. G. Lee, A. Al Harraq, K. J. M. Bishop, and B. Bharti, "Fabrication and electric field-driven active propulsion of patchy microellipsoids," *The journal of physical chemistry. B*, vol. 125, no. 16, pp. 4232–4240, 2021.

[124] D. Sehgal and I. K. Vijay, "A method for the high efficiency of water-soluble carbodiimide-mediated amidation," *Anal. Biochem.*, vol. 218, no. 1, pp. 87–91, 1994.

[125] N. Nakajima and Y. Ikada, "Mechanism of amide formation by carbodiimide for bioconjugation in aqueous media," *Bioconjug. Chem.*, vol. 6, no. 1, pp. 123–130, 1995.

[126] J. N. Zadeh, C. D. Steenberg, J. S. Bois, B. R. Wolfe, M. B. Pierce, A. R. Khan, R. M. Dirks, and N. A. Pierce, "Nupack: Analysis and design of nucleic acid systems," *J. Comput. Phys.*, vol. 32, no. 1, pp. 170–173, 2011.

[127] J.-Y. Tinevez, N. Perry, J. Schindelin, G. M. Hoopes, G. D. Reynolds, E. Laplantine, S. Y. Bednarek, S. L. Shorte, and K. W. Eliceiri, "Trackmate: An open and extensible platform for single-particle tracking," *Methods*, vol. 115, pp. 80–90, 2017.

[128] "https://shotcut.org/."

[129] OpenAI, "Chatgpt: Optimizing language models for dialogue," *OpenAI*, 30.11.2022.

[130] T. B. Brown, B. Mann, N. Ryder, M. Subbiah, J. Kaplan, P. Dhariwal, A. Neelakantan, P. Shyam, G. Sastry, A. Askell, S. Agarwal, A. Herbert-Voss, G. Krueger, T. Henighan, R. Child, A. Ramesh, D. M. Ziegler, J. Wu, C. Winter, C. Hesse, M. Chen, E. Sigler, M. Litwin, S. Gray, B. Chess, J. Clark, C. Berner, S. McCandlish, A. Radford, I. Sutskever, and D. Amodei, "Language models are few-shot learners," May 2020.

[131] A. Ianeselli, A. Salditt, C. Mast, B. Ercolano, C. L. Kufner, B. Scheu, and D. Braun, "Physical non-equilibria for prebiotic nucleic acid chemistry," *Nat. Rev. Phys.*, vol. 5, no. 3, pp. 185–195, 2023.

[132] J. L. England, "Dissipative adaptation in driven self-assembly," *Nat. Nanotechnol.*, vol. 10, no. 11, pp. 919–923, 2015.

[133] A. Arango-Restrepo, D. Barragán, and J. M. Rubi, "Self-assembling outside equilibrium: emergence of structures mediated by dissipation," *Phys. Chem. Chem. Phys.*, vol. 21, no. 32, pp. 17475–17493, 2019.

[134] C. B. Mast and D. Braun, "Thermal trap for dna replication," *Phys. Rev. Lett.*, vol. 104, no. 18, p. 188102, 2010.

[135] M. Kreysing, L. Keil, S. Lanzmich, and D. Braun, "Heat flux across an open pore enables the continuous replication and selection of oligonucleotides towards increasing length," *Nat. Chem.*, vol. 7, no. 3, pp. 203–208, 2015.

[136] A. Salditt, L. M. R. Keil, D. P. Horning, C. B. Mast, G. F. Joyce, and D. Braun, "Thermal habitat for rna amplification and accumulation," *Phys. Rev. Lett.*, vol. 125, no. 4, p. 048104, 2020.

[137] M. W. Powner, B. Gerland, and J. D. Sutherland, "Synthesis of activated pyrimidine ribonucleotides in prebiotically plausible conditions," *Nature*, vol. 459, no. 7244, pp. 239–242, 2009.

[138] P. B. Rimmer, J. Xu, S. J. Thompson, E. Gillen, J. D. Sutherland, and D. Queloz, "The origin of rna precursors on exoplanets," *Sci. Adv.*, vol. 4, no. 8, p. eaar3302, 2018.

[139] S. Rajamani, A. Vlassov, S. Benner, A. Coombs, F. Olasagasti, and D. Deamer, "Lipid-assisted synthesis of rna-like polymers from mononucleotides," *Origins Life Evol. B.*, vol. 38, no. 1, pp. 57–74, 2008.

[140] S. Becker, C. Schneider, H. Okamura, A. Crisp, T. Amatov, M. Dejmek, and T. Carell, "Wet-dry cycles enable the parallel origin of canonical and non-canonical nucleosides by continuous synthesis," *Nat. Commun.*, vol. 9, p. 163, 12 2018.

[141] L. Da Silva, M.-C. Maurel, and D. Deamer, "Salt-promoted synthesis of rna-like molecules in simulated hydrothermal conditions," *J. Mol. Evol.*, vol. 80, no. 2, pp. 86–97, 2015.

[142] A. V. Dass, S. Wunnava, J. Langlais, B. von der Esch, M. Krusche, L. Ufer, N. Chrisam, R. C. A. Dubini, F. Gartner, S. Angerpointner, C. F. Dirscherl, P. Rovó, C. B. Mast, J. E. Šponer, C. Ochsenfeld, E. Frey, and D. Braun, "Rna oligomerisation without added catalyst from 2′,3′–cyclic nucleotides by drying at air–water interfaces**," *ChemSystemsChem*, vol. 5, no. 1, 2023.

[143] S. Dagar, S. Sarkar, and S. Rajamani, "Nonenzymatic template-directed primer extension using 2'-3' cyclic nucleotides under wet-dry cycles," *Origins Life Evol. B.*, vol. 53, no. 1-2, pp. 43–60, 2023.

[144] J. Attwater, A. Wochner, V. B. Pinheiro, A. Coulson, and P. Holliger, "Ice as a protocellular medium for rna replication," *Nat. Commun.*, vol. 1, no. 1, p. 76, 2010.

[145] H. Mutschler, A. Wochner, and P. Holliger, "Freeze-thaw cycles as drivers of complex ribozyme assembly," *Nat. Chem.*, vol. 7, no. 6, pp. 502–508, 2015.

[146] S. J. Zhang, D. Duzdevich, D. Ding, and J. W. Szostak, "Freeze-thaw cycles enable a prebiotically plausible and continuous pathway from nucleotide activation to nonenzymatic rna copying," *Proc. Natl. Acad. Sci. U.S.A.*, vol. 119, no. 17, p. e2116429119, 2022.

[147] F. M. Möller, F. Kriegel, M. Kieß, V. Sojo, and D. Braun, "Steep pH gradients and directed colloid transport in a microfluidic alkaline hydrothermal pore," *Angew. Chem., Int. Ed.*, vol. 56, pp. 2340–2344, Jan. 2017.

[148] V. Helmbrecht, M. Weingart, F. Klein, D. Braun, and W. D. Orsi, "White and green rust chimneys accumulate rna in a ferruginous chemical garden," *Geobiology*, vol. 21, no. 6, pp. 758–769, 2023.

[149] T. Matreux, K. Le Vay, A. Schmid, P. Aikkila, L. Belohlavek, A. Z. Çalışkanoğlu, E. Salibi, A. Kühnlein, C. Springsklee, B. Scheu, D. B. Dingwell, D. Braun, H. Mutschler, and C. B. Mast, "Heat flows in rock cracks naturally optimize salt compositions for ribozymes," *Nat. Chem.*, vol. 13, no. 11, pp. 1038–1045, 2021.

[150] S. De and R. Klajn, "Dissipative self-assembly driven by the consumption of chemical fuels," *Adv. Mater.*, vol. 30, no. 41, p. e1706750, 2018.

[151] K. Das, L. Gabrielli, and L. J. Prins, "Chemically fueled self-assembly in biology and chemistry," *Angew. Chem., Int. Ed.*, vol. 60, no. 37, pp. 20120–20143, 2021.

[152] L. Heinen and A. Walther, "Programmable dynamic steady states in atp-driven nonequilibrium dna systems," *Sci. Adv.*, vol. 5, no. 7, p. eaaw0590, 2019.

[153] L. N. Green, H. K. K. Subramanian, V. Mardanlou, J. Kim, R. F. Hariadi, and E. Franco, "Autonomous dynamic control of dna nanostructure self-assembly," *Nat. Chem.*, vol. 11, no. 6, pp. 510–520, 2019.

[154] S. Gentile, E. Del Grosso, P. E. Pungchai, E. Franco, L. J. Prins, and F. Ricci, "Spontaneous reorganization of dna-based polymers in higher ordered structures fueled by rna," *J. Am. Chem. Soc.*, vol. 143, no. 48, pp. 20296–20301, 2021.

[155] J. Deng and A. Walther, "Programmable and chemically fueled dna coacervates by transient liquid-liquid phase separation," *Chem*, vol. 6, no. 12, pp. 3329–3343, 2020.

[156] E. Del Grosso, L. J. Prins, and F. Ricci, "Transient dna-based nanostructures controlled by redox inputs," *Angew. Chem., Int. Ed.*, vol. 59, no. 32, pp. 13238–13245, 2020.

[157] E. Del Grosso, E. Franco, L. J. Prins, and F. Ricci, "Dissipative dna nanotechnology," *Nat. Chem.*, vol. 14, no. 6, pp. 600–613, 2022.

[158] S. Agarwal and E. Franco, "Enzyme-driven assembly and disassembly of hybrid dna-rna nanotubes," *J. Am. Chem. Soc.*, vol. 141, no. 19, pp. 7831–7841, 2019.

[159] Y. Li, Y. D. Tseng, S. Y. Kwon, L. d'Espaux, J. S. Bunch, P. L. McEuen, and D. Luo, "Controlled assembly of dendrimer-like DNA," *Nat. Mater.*, vol. 3, pp. 38–42, 01 2004.

[160] S. H. Um, J. B. Lee, N. Park, S. Y. Kwon, C. C. Umbach, and D. Luo, "Enzyme-catalysed assembly of DNA hydrogel," *Nat. Mater.*, vol. 5, pp. 797 – 801, 10 2006.

[161] S. Biffi, R. Cerbino, F. Bomboi, E. M. Paraboschi, R. Asselta, F. Sciortino, and T. Bellini, "Phase behavior and critical activated dynamics of limited-valence dna nanostars," *Proc. Natl. Acad. Sci. U.S.A.*, vol. 110, no. 39, pp. 15633–15637, 2013.

[162] L. Rovigatti, F. Smallenburg, F. Romano, and F. Sciortino, "Gels of DNA Nanostars Never Crystallize," *ACS Nano*, vol. 8, no. 4, pp. 3567–3574, 2014.

[163] G. Nava, M. Rossi, S. Biffi, F. Sciortino, and T. Bellini, "Fluctuating elasticity mode in transient molecular networks," *Phys. Rev. Lett.*, vol. 119, no. 7, p. 078002, 2017.

[164] Z. Xing, A. Caciagli, T. Cao, I. Stoev, M. Zupkauskas, T. O'Neill, T. Wenzel, R. Lamboll, D. Liu, and E. Eiser, "Microrheology of dna hydrogels," *Proc. Natl. Acad. Sci. U.S.A.*, vol. 115, no. 32, pp. 8137–8142, 2018.

[165] R. A. Brady, W. T. Kaufhold, N. J. Brooks, V. Foderà, and L. D. Michele, "Flexibility defines structure in crystals of amphiphilic DNA nanostars," *J. Phys. Condens. Matter*, vol. 31, no. 7, p. 074003, 2019.

[166] Y. Sato, T. Sakamoto, and M. Takinoue, "Sequence-based engineering of dynamic functions of micrometer-sized DNA droplets," *Sci. Adv.*, vol. 6, no. 23, p. eaba3471, 2020.

[167] S. Agarwal, D. Osmanovic, M. A. Klocke, and E. Franco, "The Growth Rate of DNA Condensate Droplets Increases with the Size of Participating Subunits," *ACS Nano*, vol. 16, no. 8, pp. 11842–11851, 2022.

[168] J. J. McDermott, A. Kar, M. Daher, S. Klara, G. Wang, A. Sen, and D. Velegol, "Self-generated diffusioosmotic flows from calcium carbonate micropumps," *Langmuir*, vol. 28, no. 44, pp. 15491–15497, 2012.

[169] T.-Y. Chiang and D. Velegol, "Multi-ion diffusiophoresis," *J. Colloid Interf. Sci.*, vol. 424, pp. 120–123, 2014.

[170] J. S. Paustian, C. D. Angulo, R. Nery-Azevedo, N. Shi, A. I. Abdel-Fattah, and T. M. Squires, "Direct measurements of colloidal solvophoresis under imposed solvent and solute gradients," *Langmuir*, vol. 31, no. 15, pp. 4402–4410, 2015.

[171] A. Kar, T.-Y. Chiang, I. Ortiz Rivera, A. Sen, and D. Velegol, "Enhanced transport into and out of dead-end pores," *ACS nano*, vol. 9, no. 1, pp. 746–753, 2015.

[172] A. Banerjee, I. Williams, R. N. Azevedo, M. E. Helgeson, and T. M. Squires, "Soluto-inertial phenomena: Designing long-range, long-lasting, surface-specific interactions in suspensions," *Proc. Natl. Acad. Sci. U.S.A.*, vol. 113, no. 31, pp. 8612–8617, 2016.

[173] S. Shin, E. Um, B. Sabass, J. T. Ault, M. Rahimi, P. B. Warren, and H. A. Stone, "Size-dependent control of colloid transport via solute gradients in dead-end channels," *Proc. Natl. Acad. Sci. U.S.A.*, vol. 113, no. 2, pp. 257–261, 2016.

[174] D. Velegol, A. Garg, R. Guha, A. Kar, and M. Kumar, "Origins of concentration gradients for diffusiophoresis," *Soft Matter*, vol. 12, no. 21, pp. 4686–4703, 2016.

[175] A. Gupta, S. Shim, and H. A. Stone, "Diffusiophoresis: from dilute to concentrated electrolytes," *Soft Matter*, vol. 16, no. 30, pp. 6975–6984, 2020.

[176] B. Ramm, A. Goychuk, A. Khmelinskaia, P. Blumhardt, H. Eto, K. A. Ganzinger, E. Frey, and P. Schwille, "A diffusiophoretic mechanism for atp-driven transport without motor proteins," *Nat. Phys.*, vol. 17, no. 7, pp. 850–858, 2021.

[177] S. Shim, "Diffusiophoresis, diffusioosmosis, and microfluidics: Surface-flow-driven phenomena in the presence of flow," *Chem. Rev.*, vol. 122, no. 7, pp. 6986–7009, 2022.

[178] Q. A. E. Peter, R. P. B. Jacquat, T. W. Herling, P. K. Challa, T. Kartanas, and T. P. J. Knowles, "Microscale diffusiophoresis of proteins," *J. Phys. Chem. B*, vol. 126, no. 44, pp. 8913–8920, 2022.

[179] B. Abécassis, C. Cottin-Bizonne, C. Ybert, A. Ajdari, and L. Bocquet, "Boosting migration of large particles by solute contrasts," *Nat. Mater.*, vol. 7, no. 10, pp. 785–789, 2008.

[180] J. Palacci, B. Abécassis, C. Cottin-Bizonne, C. Ybert, and L. Bocquet, "Colloidal motility and pattern formation under rectified diffusiophoresis," *Phys. Rev. Lett.*, vol. 104, no. 13, p. 138302, 2010.

[181] N. Shi, R. Nery-Azevedo, A. I. Abdel-Fattah, and T. M. Squires, "Diffusiophoretic focusing of suspended colloids," *Phys. Rev. Lett.*, vol. 117, no. 25, p. 258001, 2016.

[182] S. M. Friedrich, J. M. Burke, K. J. Liu, C. F. Ivory, and T.-H. Wang, "Molecular rheotaxis directs dna migration and concentration against a pressure-driven flow," *Nat. Commun.*, vol. 8, no. 1, p. 1213, 2017.

[183] S. Li, A. Li, K. Hsieh, S. M. Friedrich, and T.-H. Wang, "Electrode-free concentration and recovery of dna at physiologically relevant ionic concentrations," *Anal. Chem.*, vol. 92, no. 8, pp. 6150–6157, 2020.

[184] M. K. Rasmussen, J. N. Pedersen, and R. Marie, "Size and surface charge characterization of nanoparticles with a salt gradient," *Nat. Commun.*, vol. 11, no. 1, p. 2337, 2020.

[185] P. H. Barry and J. W. Lynch, "Liquid junction potentials and small cell effects in patch-clamp analysis," *J. Membrane Biol.*, vol. 121, no. 2, pp. 101–117, 1991.

[186] A. Gupta, B. Rallabandi, and H. A. Stone, "Diffusiophoretic and diffusioosmotic velocities for mixtures of valence-asymmetric electrolytes," *Phys. Rev. Fluids*, vol. 4, no. 4, p. 043702, 2019.

[187] J. L. Wilson, S. Shim, Y. E. Yu, A. Gupta, and H. A. Stone, "Diffusiophoresis in multivalent electrolytes," *Langmuir*, vol. 36, no. 25, pp. 7014–7020, 2020.

[188] A. Oesterle, "Pipette cookbook 2015: P-97 & p-1000 micropipette pullers," *Sutter Instrument, California*, 2015.

[189] E. J. F. Dickinson, J. G. Limon-Petersen, and R. G. Compton, "The electroneutrality approximation in electrochemistry," *J. Solid State Electr.*, vol. 15, no. 7-8, pp. 1335–1345, 2011.

[190] C. A. Schneider, W. S. Rasband, and K. W. Eliceiri, "Nih image to imagej: 25 years of image analysis," *Nat. Methods*, vol. 9, no. 7, pp. 671–675, 2012.

[191] OpenAI, "Chatgpt-4 (Mar 14 version)," 2023. Large language model.

[192] OpenAI, "Gpt-4 technical report," 2023.

[193] Y. Sato and M. Takinoue, "Capsule-like dna hydrogels with patterns formed by lateral phase separation of dna nanostructures," *J. Am. Chem. Soc.*, vol. 2, no. 1, pp. 159–168, 2022.

[194] G. Junot, M. De Corato, and P. Tierno, "Large scale zigzag pattern emerging from circulating active shakers," *Phys. Rev. Lett.*, vol. 131, p. 068301, Aug. 2023.